Title
The Role of Dipolarizing Flux Bundles in Magnetotail Dynamics

Author
Liu, Jiang

Publication Date
2013

Peer reviewed|Thesis/dissertation

University of California
Los Angeles

The Role of Dipolarizing Flux Bundles in Magnetotail Dynamics

A dissertation submitted in partial satisfaction
of the requirements for the degree
Doctor of Philosophy in Geophysics and Space Physics

by

Jiang Liu

2013

Abstract of the Dissertation

The Role of Dipolarizing Flux Bundles in Magnetotail Dynamics

by

Jiang Liu

Doctor of Philosophy in Geophysics and Space Physics

University of California, Los Angeles, 2013

Professor Vassilis Angelopoulos, Chair

Transient ($\sim$ 40s time scale) flux tubes carrying strong northward magnetic field and earthward flow are frequently observed in the magnetotail. Here I use the term "dipolarizing flux bundles" (DFBs) to describe these flux tubes. Thought to be generated by tail reconnection at $X_{\mathrm{GSM}} =\sim -20$ $\mathrm{R_E}$, DFBs travel earthward towards the inner edge of the plasma sheet, bringing significant changes to the near-earth magnetotail. After twenty years of extensive study on DFBs, numerous questions regarding their role in magnetotail dynamics remain. The THEMIS mission, which enables multi-point observations at different tail locations, provides the opportunity to answer many of these questions. With a statistical study based on THEMIS data, I explore the dipolarizing flux bundle's role in several aspects of magnetotail dynamics—its importance in magnetotail flux transport, the mechanisms controlling its motion, the modifications its motion makes to the ambient plasma, its current system, and the modifications it makes to the global magnetotail current system.

First, I establish that DFBs are the major, high-efficiency magnetic flux carriers in near-earth magnetotail convection. Therefore, the DFB flux transport properties I found (e.g., DFBs transport more magnetic flux during substorm time) may shape all near-earth magnetotail convection. Then I investigate how a DFB's earthward motion modifies the plasma inside it as well as the ambient plasma. Dipolarizing flux bundle motion results in a total pressure buildup inside the $\sim$ 1000km-thin DF layer; the buildup exerts a tailward force from

there to retard DFB motion. This motion also builds up thermal pressure, the distribution of which requires the existence of field-aligned currents (FACs) near the DFB. To confirm the existence of these FACs, I infer the DFB-associated current system from magnetic field variations. The magnetic field variations are consistent with region-2-sense (towards/away from earth to the DFB's dusk/dawn side) FACs immediately earthward of the DFB and region-1-sense (opposite to region-2-sense) FACs inside the DF layer. Such a FAC configuration is similar to that of a substorm current wedge (SCW). In addition, the amount of current carried by several DFBs is sufficient to form a typical $\sim$ 1 MA SCW. Therefore, I suggest that dipolarizing flux bundles are "wedgelets"—building blocks of a substorm current wedge.

The dissertation of Jiang Liu is approved.

Lawrence R. Lyons

Robert L. McPherron

Christopher T. Russell

Vassilis Angelopoulos, Committee Chair

University of California, Los Angeles

2013

This thesis is dedicated to my late grandmother Xue Huifang.

Table of Contents

1 Introduction **1**

1.1 Dipolarizing Flux Bundles 1

1.2 Flux transport of DFBs 6

1.3 Causes and results of DFB motion 7

1.4 The DFB-associated current system 9

1.5 Outline of study 11

2 Dataset and methodology **13**

2.1 THEMIS data 13

2.2 Event selection 14

2.2.1 Selection of dipolarizing flux bundles 15

2.2.2 Selection of bursty bulk flows 20

2.3 The topology of dipolarizing flux bundles 21

2.3.1 Background 21

2.3.2 Results 25

2.3.3 Summary and discussion 34

3 Magnetic flux transport by dipolarizing flux bundles **35**

3.1 Introduction 35

3.2 Dataset 38

3.3 Results 39

3.3.1 The importance of dipolarizing flux bundles for flux transport 39

3.3.2 Spatial distribution of DFBs and their transport 43

3.4 Summary and discussion 62

3.4.1 The importance of DFBs in magnetotail convection 64
3.4.2 A picture of the DFB life as a flux transporter 66
3.4.3 The relationship between DFBs and other tail transients 67

4 The controlling factor and the results of the dipolarizing flux bundles' motion 69

4.1 Introduction 69
4.1.1 The mechanism controlling DFB motion 70
4.1.2 Dipolarizing flux bundle-associated FACs 71
4.2 Results 73
4.2.1 Total pressure distribution 73
4.2.2 Thermal pressure distribution 77
4.2.3 Plasma flow distribution 81
4.3 Summary and Discussion 84
4.3.1 The nature of pressure and flow distributions 85
4.3.2 The factors controlling DFB motion 86
4.3.3 The relationship between thermal pressure buildup and FACs 87

5 The current system of the dipolarizing flux bundle 91

5.1 Introduction 92
5.2 Results and Interpretations 94
5.2.1 Region-2 and -1-sense field-aligned currents 94
5.2.2 The DFCS current direction 97
5.2.3 DFCS Thickness, Density, and Total Strength 106
5.2.4 Cross-tail Current Sheet Modification by Dipolarizing Flux Bundles . 110
5.3 Summary and Additional Discussion 115

6 Conclusions **119**

Appendix A Correcting THEMIS EFI measurements **122**

A.1 The correction method 122

A.2 Considering quiet-time convection 123

Appendix B Determining the Dipolarization Front's Normal Direction . . **126**

Appendix C Reconstruction of quantity distributions around the DFB . . **130**

Appendix D Clarifying the inference of the direction of dipolarization front current **134**

D.1 The angle between **L** and Z 134

D.2 The dipolarization front current direction relative to the dipolarization front average magnetic field direction 136

Bibliography **142**

List of Figures

1.1 Illustration of plasma bubbles 2

1.2 Properties of BBFs 5

1.3 A self-closing DFB current system 10

2.1 Locations of DFBs 17

2.2 Superposed quantities of DFBs 19

2.3 Properties of BBFs 22

2.4 XY view of a plasma bubble 23

2.5 Shape of a DFB 24

2.6 n_z dependence on distance from the neutral sheet 27

2.7 V_y dependence on relative location to the DFB 28

2.8 DFB radius estimation 30

2.9 How to calculate DFB radius 33

3.1 A BBF example 41

3.2 Determining DFB duration 42

3.3 The importance of DFB flux transport 45

3.4 X dependence of DFB flux transport 47

3.5 More X dependence of DFB flux transport 51

3.6 Y dependence of DFB flux transport 54

3.7 The dependence of DFB flux transport on distance from the neutral sheet . . 56

3.8 An illustration of the DFB flux tube 57

3.9 AE dependence of DFB flux transport 58

3.10 AE dependence of DFB occurrence rate 61

4.1 Total pressure distribution near DFBs 74
4.2 Superposed quantities of DFBs 76
4.3 Thermal pressure distribution 79
4.4 Equatorial thermal pressure distribution 80
4.5 Flow distribution 82
4.6 Illustration of pressure-related FACs 89

5.1 B_y variations of a DFB 96
5.2 Angle between $\mathbf{B}_{\text{in}}$ and $\mathbf{L}$ 100
5.3 Angle between $\mathbf{B}_{\text{in}}$ and $\mathbf{L}$ (illustrated) 102
5.4 Illustration of DFCS current system 104
5.5 Thickness and strength of the DFCS 107
5.6 DFB field lines 112
5.7 Reconstruction of DFB field lines 114

A.1 Results from alternative EFI offset removal 125

B.1 Dipolarization front normal directions 129

C.1 Satellite paths relative to the DFB 131

D.1 Angle between $\mathbf{L}$ and Z 135
D.2 Angle between $\langle\mathbf{B}\rangle$ and $\mathbf{L}$ 138
D.3 Angle between $\langle\mathbf{B}\rangle$ and $\mathbf{L}$ (illustrated) 139
D.4 Angle between $\langle\mathbf{b}\rangle$ and $\mathbf{L}$ 141
D.5 Angle between $\langle\mathbf{b}\rangle$ and $\mathbf{L}$ (illustrated) 141

Acknowledgments

The work in this thesis would not have been possible without the time and effort of many people. I am sincerely thankful for all the help and support that I received from my advisor, professors, and researchers at UCLA; fellow graduate students at UCLA; and collaborators from other institutes. I am grateful to my parents, Liu Jianke and Zhang Baoyun, and my wife, Wang Yue, for their love and support. I am also thankful to my grandfather, Liu Shengjia, for leading me to the world of science.

Many people contributed significantly to this thesis. I am extremely thankful for the mentorship of my advisor, Vassilis Angelopoulos. I was fortunate to be one of his first graduate students. His impressive breadth of knowledge in space plasma physics has encouraged me to enjoy sailing through plasma physics books and journal papers. His heavily-packed daily schedule taught me the importance of working hard to succeed. Vassilis encouraged me to work on several research projects before settling on dipolarizing flux bundles, providing extremely helpful advices which made each project fruitful. His helpful advice on the dipolarizing flux bundle project made this thesis possible. I am looking forward to continuing working with Vassilis.

I am also grateful for the time, effort, and advice from my first advisor in space physics, Professor Zuyin Pu. Without my experiences working with him at Peking University for my undergraduate dissertation, I would not currently be studying magnetospheric physics. I hope to continue collaborating with him throughout my career.

I have benefited from the teaching of several professors at UCLA. I was lucky enough to take the last advanced space plasma physics class by Margaret Kivelson and the last substorm class by Bob McPherron. I also learned from Ray Walker in class, and I greatly appreciate his help in preparing for my field exam. The classes I took with Larry Lyons, Richard Thorne, Chris Russell, George Morales, and Arlene Russell were extremely beneficial for expanding my knowledge and skills in magnetohydrodynamics, inner magnetosphere, kinetic theories, and scientific writing. Support from Maha Ashour-Abdalla for attending the international space physics simulation workshop helped me to learn various simulation techniques.

The knowledge and expertise of colleagues and collaborators at UCLA and other institutes have benefited my this thesis greatly. Andrei Runov and Xuzhi Zhou, as experts in dipolarizing flux bundles, taught me many physics and data analysis methods that were helpful. They contributed substantially to Chapters 2 through 5 of this thesis. I learned from Zhonghua Yao much about dipolarizing flux bundles and substorms, especially the relationship between thermal pressure and field-aligned currents; Chapter 4 contains his contribution. Christine Gabrielse helped me writing Chapter 1. Michael Hartinger provided me the template for this thesis.

This thesis has been crucially improved by the suggestions and comments of my thesis committee members, Larry Lyons, Chris Russell, and Bob McPherron. It has also been greatly improved through the discussions with Bob Strangeway, Song Yan, Weijie Sun, Huishan Fu, Tung-Shin Hsu, Xiangning Chu, Tai Phan, Micheal Shay, and Gerhard Haerendel. During Monday group meetings, the suggestions from other group members, Stefan Kiehas, Drew Turner, Ferdinand Plaschke, Michael Hartinger, Christine Gabrielse, ShanShan Li, Xiaojia Zhang, Justin Lee, and Jing Li, have also helped improved my work. During other occasions, I received great help and beneficial suggestions from Hui Zhang, Quanqi Shi, Yasong Ge, Magret Kivelson, Meng Zhou, Shiyong Huang, Song Fu, Qiugang Zong, Suiyan Fu, Zuyin Pu, Forrest Mozer, Wenlong Liu, Xianguo Zhang, Shin Ohtani, and Victor Sergeev. I am also thankful to Lauri Holbrook, Emmanuel Masonsong, Rick Fort, Jim Nakatsuka, and the ESS and IGPP staff for their help with administrative affairs that enabled me to finish my thesis research.

I thank many scientists for providing the tools and data used in my study. I acknowledge NASA contract NAS5-02099 for financial support during my thesis. I am grateful to John W. Bonnell and Forrest S. Mozer for use of the THEMIS EFI data. I thank Davin Larson and Robert P. Lin for use of THEMIS SST and Charles W. Carlson and James P. McFadden for use of ESA data. I am grateful to Karl-Heinz Glassmeier, Uli Auster, and Wolfgang Baumjohann for the use of FGM data provided under the lead of the Technical University of Braunschweig and for financial support through the German Ministry for Economy and Technology and the German Center for Aviation and Space (DLR) under contract 50 OC

0302. I thank Stephen Mende and Christopher T. Russell for use of the THEMIS ground magnetometer data. I thank Ian R. Mann, D.K. Milling, and the remainder of the CARISMA team for use of GMAG data (CARISMA is operated by the University of Alberta, funded by the Canadian Space Agency). I am grateful to Patrick Cruce, Cindy Russell, Brian Kerr, Aaron Flores, and the rest of the THEMIS programmer team for helps in using these data.

At last, I am very grateful to Judy Hohl, who taught me how to write. Her patient advices on all aspects of writing an article, including but not limited to a scientific paper, has entirely changed my incorrect writing habits. Without her help, this thesis would have remained in my mind.

Chapter 2 combines a part of *Liu et al.* (2013a) and a part of *Liu et al.* (2013b).

Chapter 3 is a version of *Liu et al.* (2013c).

Chapter 4 is a version of *Liu et al.* (2013b).

Chapter 5 is a part of *Liu et al.* (2013a).

Vita

2005	Canon Scholarship School of Earth and Space Sciences, Peking University.
2006	Jun-Tseng Scholarship Peking University.
2007	B.A. Space Physics School of Earth and Space Sciences, Peking University.
2007-2013	Graduate Student Researcher Earth and Space Sciences Department, UCLA.
2010	M.S. Geophysics and Space Physics UCLA.
2012	Harold and Mayla Sullwold Scholarship Earth and Space Sciences Department, UCLA.

Publications

Shang, W.-S., Z.-H. Yao, Q.-Q. Shi, W.-J. Sun, S.-Y. Fu, **J. Liu**, A.-M. Tian, Q.-G. Zong, Z. Y. Pu, and T. Xiao (2013), Braking of high speed flows in the magnetotail: Themis joint observations, *Chin. Sci. Bull.*, in press.

Sun, W. J., S. Y. Fu, G. K. Parks, **J. Liu**, Z. H. Yao, Q. Q. Shi, Q.-G. Zong, S. Y. Huang, Z. Y. Pu, and T. Xiao (2013), Field-aligned currents associated with dipolarization fronts, *Geophys. Res. Lett.*, doi:10.1002/grl.50902.

Yao, Z. H., V. Angelopoulos, Z. Y. Pu, S. Y. Fu, M. Kubyshkina, **J. Liu**, X. N. Chu,

T. Nishimura, X. Cao, A. M. Du, C. Yue, Q. Q. Shi, and Y. Wei (2013), Conjugate observations of flow diversion in the magnetotail and auroral arc extension in the ionosphere, *J. Geophys. Res.*, doi:10.1002/jgra.50419.

Liu, J., V. Angelopoulos, A. Runov, and X.-Z. Zhou (2013a), On the current sheets surrounding dipolarizing flux bundles in the magnetotail: The case for wedgelets, *J. Geophys. Res.*, *118*, 2000–2020, doi:10.1002/jgra.50092.

Zhou, X.-Z., V. Angelopoulos, A. Runov, **J. Liu**, and Y. S. Ge (2012), Emergence of the active magnetotail plasma sheet boundary from transient, localized ion acceleration, *J. Geophys. Res.*, *117*, A10216, doi:10.1029/2012JA018171.

Yao, Z. H., Z. Y. Pu, S. Y. Fu, V. Angelopoulos, M. Kubyshkina, X. Xing, L. Lyons, Y. Nishimura, L. Xie, X. G. Wang, C. J. Xiao, X. Cao, **J. Liu**, H. Zhang, M. Nowada, Q. G. Zong, R. L. Guo, J. Zhong, and J. X. Li (2012), Mechanism of substorm current wedge formation: THEMIS observations, *Geophys. Res. Lett.*, *39*, L13102, doi:10.1029/2012GL052055.

Liu, J., C. Gabrielse, V. Angelopoulos, N. A. Frissell, L. R. Lyons, J. P. McFadden, J. Bonnell, and K. H. Glassmeier (2011b), Superposed epoch analysis of magnetotail flux transport during substorms observed by THEMIS, *J. Geophys. Res.*, *116*, A00I29, doi:10.1029/2010JA015886.

Liu, J., V. Angelopoulos, M. Kubyshkina, J. McFadden, K.-H. Glassmeier, and C. T. Russell (2011a), Revised timing and onset location of two isolated substorms observed by Time History of Events and Macroscale Interactions During Substorms (THEMIS), *J. Geophys. Res.*, *116*, A00I17, doi:10.1029/2010JA015877.

Chu, X.-N., Z.-Y. Pu, X. Cao, J. Wang, V. Mishin, V. Angelopoulos, **J. Liu**, Y. Wei, K.-H.

Glassmeier, J. Mcfadden, D. Larson, S. Mende, H. Frey, C. Russell, I. Mann, D. Sibeck, Q.-G. Zong, S.-Y. Fu, L. Xie, T. I. Saifudinova, M. V. Tolochko, L. A. Sapronova, H. Reme, and E. Lucek (2010), Themis observations of two substorms on february 26, 2008, *Science China Technological Sciences*, *53*(5), 1328–1337.

Pu, Z. Y., X. N. Chu, X. Cao, V. Mishin, V. Angelopoulos, J. Wang, Y. Wei, Q. G. Zong, S. Y. Fu, L. Xie, K. Glassmeier, H. Frey, C. T. Russell, **J. Liu**, J. McFadden, D. Larson, S. Mende, I. Mann, D. Sibeck, L. A. Sapronova, M. V. Tolochko, T. I. Saifudinova, Z. H. Yao, X. G. Wang, C. J. Xiao, X. Z. Zhou, H. Reme, and E. Lucek (2010), THEMIS observations of substorms on 26 February 2008 initiated by magnetotail reconnection, *J. Geophys. Res.*, *115*, 2212, doi:10.1029/2009JA014217.

Ivanova, V., **J. Liu**, S. Kiehas, V. Semenov, and H. Biernat (2009), Inverse reconstruction technique based on time-dependent Petschek-type reconnection model: first application to THEMIS magnetotail observations, *Ann. Geophys.*, *27*, 4369–4377, doi:10.5194/angeo-27-4369-2009.

Liu, J., V. Angelopoulos, H. Frey, J. McFadden, D. Larson, K. Glassmeier, S. Mende, C. T. Russell, I. J. Rae, K. R. Murphy, and S. Apatenkov (2009), THEMIS observation of a substorm event on 04:35, 22 February 2008, *Ann. Geophys.*, *27*, 1831–1841, doi:10.5194/angeo-27-1831-2009.

Liu, J., V. Angelopoulos, D. Sibeck, T. Phan, Z. Y. Pu, J. McFadden, K. H. Glassmeier, and H. U. Auster (2008), THEMIS observations of the dayside traveling compression region and flows surrounding flux transfer events, *Geophys. Res. Lett.*, *35*, L17S07, doi:10.1029/2008GL033673.

Angelopoulos, V., D. Sibeck, C. W. Carlson, J. P. McFadden, D. Larson, R. P. Lin, J. W. Bonnell, F. S. Mozer, R. Ergun, C. Cully, K. H. Glassmeier, U. Auster, A. Roux, O. Lecontel,

S. Frey, T. Phan, S. Mende, H. Frey, E. Donovan, C. T. Russell, R. Strangeway, **J. Liu**, I. Mann, J. Rae, J. Raeder, X. Li, W. Liu, H. J. Singer, V. A. Sergeev, S. Apatenkov, G. Parks, M. Fillingim, and J. Sigwarth (2008), First Results from the THEMIS Mission, *Space Sci. Rev.*, *141*, 453–476, doi:10.1007/s11214-008-9378-4.

Zhang, H., K. K. Khurana, M. G. Kivelson, V. Angelopoulos, Z. Y. Pu, Q.-G. Zong, **J. Liu**, and X.-Z. Zhou (2008), Modeling a force-free flux transfer event probed by multiple Time History of Events and Macroscale Interactions during Substorms (THEMIS) spacecraft, *J. Geophys. Res.*, *113*, A00C05, doi:10.1029/2008JA013451.

CHAPTER 1

Introduction

1.1 Dipolarizing Flux Bundles

Russell and McPherron (1973) first reported observations of spatially and temporally localized enhancements of the near-Earth ($X > -30$ R_E) magnetotail's northward magnetic field component, B_z. (X and B_z are in GSM coordinates, which are used in this thesis unless otherwise specified.) As high B_z is characteristic of Earth's dipole field, these enhancements have been called transient "dipolarizations". Each transient dipolarization is led by a sharp increase in B_z, referred to as a "dipolarization front"; B_z remains high for several tens of seconds. These high-B_z structures were later found to be high-B_z flux tubes that travel earthward from their source in the magnetotail (most likely generated by near-earth tail reconnection, usually tailward of $X = -20$ R_E) (e.g., *Runov et al.*, 2009). Although such a flux tube is greatly deformed from extremely stretched to highly dipolar (see Figure 1.1a) as it travels, the magnetic flux it contains should be carried and transported coherently like a bundle. To emphasize this property, I refer to these magnetotail high-B_z flux tubes as "dipolarizing flux bundles" (DFBs).

Since their discovery by *Russell and McPherron* (1973), DFBs have been the focus of intense research, especially after the "plasma bubble" model (Figure 1.1) showed their importance in magnetotail dynamics.

The plasma bubble model is a theoretical description of a DFB. The concept of plasma bubbles was first proposed by *Pontius and Wolf* (1990) (hereafter referred to as PW90) to solve the so-called "pressure crisis" (*Erickson and Wolf*, 1980). The pressure crisis arises from the assumption of steady convection in the magnetotail and conservation of entropy

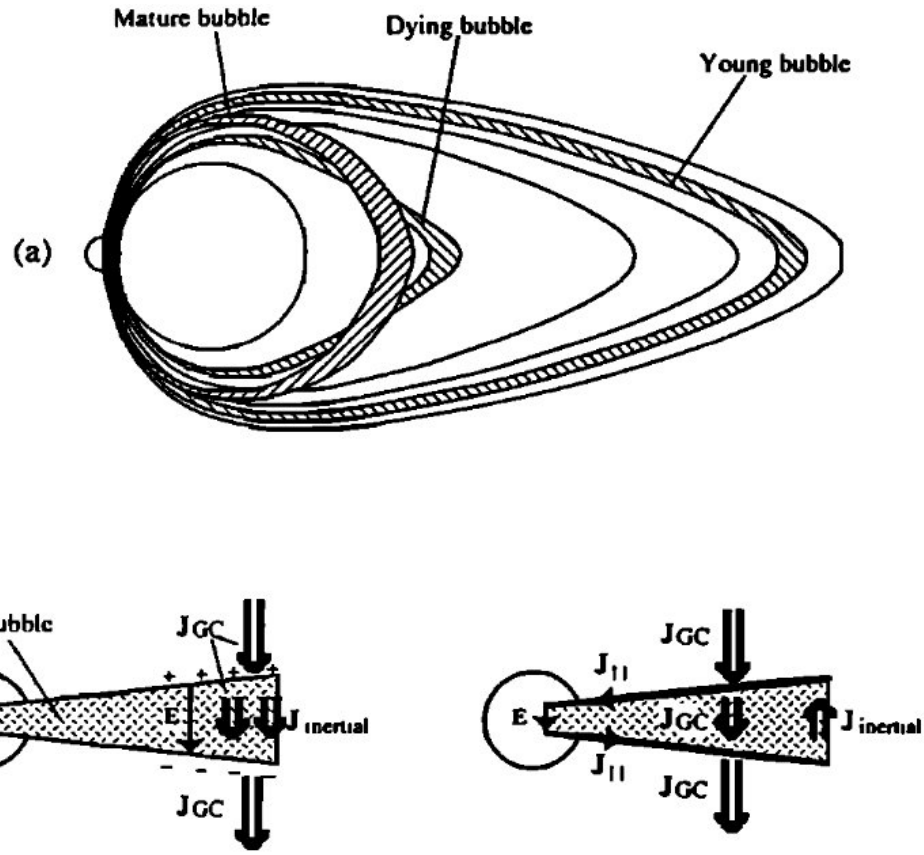

Figure 1.1: (After *Chen and Wolf* (1993)) Cartoons illustrating some stages in the evolution of a bubble (DFB). (a) the noon-midnight meridian plane; in this view the decelerating bubble and mature bubble would look very similar, and only the mature bubble is shown. (b) and (c) "Overhead views", the view of an observer located high above the north pole. Dawnside is toward the top, duskside toward the bottom. The variables $\mathbf{J}_{GC}$, $\mathbf{J}_{in}$, and $\mathbf{J}_{\parallel}$ represent gradient/curvature drift, inertial currents, and Birkeland currents. Figure 1.1b shows a young bubble; Figure 1.1c shows a decelerating bubble. The overhead view of a mature bubble would be the same as that for the decelerating bubble, but in the mature bubble, inertial current would be negligible. In all cases the Sun is to the left.

within a flux tube, requiring the parameter $pV^{5/3}$ (where p is the plasma pressure and V is the volume of the flux tube) to be constant along the flux-tube streamlines. Observations show that the measured lobe pressure falls much more slowly with distance than the modeled pressure within a flux tube that convects earthward slowly, conserving $pV^{5/3}$.

To address this problem, PW90 proposed the existence of density-depleted flux tubes—plasma bubbles—that have much lower $pV^{5/3}$ than their surrounding flux tubes in the magnetotail. A plasma bubble, or a DFB, therefore has lower plasma pressure than the plasma that surrounds it, requiring a larger magnetic field strength inside it than outside it to maintain quasi-pressure balance. As these bubbles convect earthward at a much higher speed than the surrounding flux tubes, they make a non-negligible contribution to the net rate of plasma transport. *Pontius and Wolf* (1990) followed by *Chen and Wolf* (1993) suggests that magnetotail convection is completed by plasma bubbles impulsively rather than steadily which invalidates the pressure crisis.

The ideas of PW90 were confirmed and extended by the discovery of high-speed flows and especially bursty-bulk flows (BBFs) in the central plasma sheet (*Baumjohann et al.*, 1990; *Angelopoulos et al.*, 1992, (hereafter referred to as A92)). Bursty bulk flows are defined in A92 as high-speed flows (faster than 400 km/s) that organize themselves in 10-min time scale flow enhancements. Each individual flow peak is defined as a flow burst. *Angelopoulos et al.* (1992) surveyed two years of AMPTE/IRM data collected when the satellite was located at the inner central plasma sheet, where the magnetic field Z component and flow velocity are negligible most of the time, and studied statistically the observed earthward BBFs in this database. Figure 1.2 shows the results of the superposed epoch analysis applied to the components of the magnetic field, the ion velocity, density and temperature, and the sum of the ion and magnetic field pressure (which is very close to the total pressure). As seen in Figures 1.2a and 1.2b, the peak in B_z appears at the same time as the flow peak. This statistically significant, positive enhancement of B_z suggests a close relationship between BBFs and dipolarizing flux bundles—BBFs are the flow signature of DFBs. Ninety percent of the BBFs, and by inference DFBs, were captured during geomagnetically active conditions (AE$>$ 100nT). Figure 1.2b shows that BBFs are strongly earthward, with vanishing

average V_y and V_z. The velocity of these BBFs suggests that DFBs mainly travel earthward, consistent with PW90's plasma bubble model. One deviation of the statistical result from the PW90 picture emerges in Figure 1.2d; namely, density depletion is not statistically present inside the bubbles when the data are organized by their flow peaks. Nevertheless, early case studies (*Sergeev et al.*, 1996) and more recent statistical studies organized by the DFB onsets (e.g., *Ohtani et al.*, 2004; *Runov et al.*, 2011) confirmed the density and plasma pressure depletions brought about by plasma bubbles (DFBs).

Using results from PW90, A92, and other publications, *Chen and Wolf* (1993) (hereafter referred to as CW93) suggested a basic picture of plasma bubble (DFB) evolution (Figure 1.1). After its generation at $X = -20$ to -30 R_E by near-earth tail reconnection (e.g., *Sitnov et al.*, 2009), the bubble moves earthward with the reconnection outflow. Because the duskward gradient/curvature currents are weaker inside the bubble than outside, the bubble will charge up positively on the dawnside and negatively on the duskside (Figure 1.1b), providing a stronger dawn-dusk electric field than in the background. The equatorial part of the bubble will be accelerated earthward by $\mathbf{j} \times \mathbf{B}$ force, where $\mathbf{j}$ is a duskward current across the bubble. As the bubble approaches Earth, its $pV^{5/3}$ value will eventually approach those of its equatorial neighbors, because $pV^{5/3}$ of the surrounding plasma sheet decreases earthward and because of particles gradient/curvature drift into the bubble, increasing the bubble's $pV^{5/3}$. The earthward acceleration will eventually reverse (Figure 1.1c). After the bubble's earthward equatorial motion has declined sufficiently, it becomes a "mature bubble" (Figure 1.1a). Its shape is rounder than its neighbors and its ionospheric footprint is poleward of the footprints of its equatorial neighbors. After equatorial motion has slowed, the field line's equatorward ionospheric motion will eventually catch up. In the final stage of the bubble's life ("dying bubble" in the Figure 1.1a), it has rebounded a little and become indistinguishable from its neighbors in the plasma sheet. In reality, however, a DFB (plasma bubble) may overshoot and rebound multiple times before it reaches its final equilibrium location (e.g., *Chen and Wolf*, 1999; *Panov et al.*, 2010). In addition, at a DFB's dying stage it does not simply blend with the ambient field, but permanently enhances the magnetic field near geosynchronous orbit. This enhancement is called a flux pileup (e.g., *Zhang et al.*, 2007).

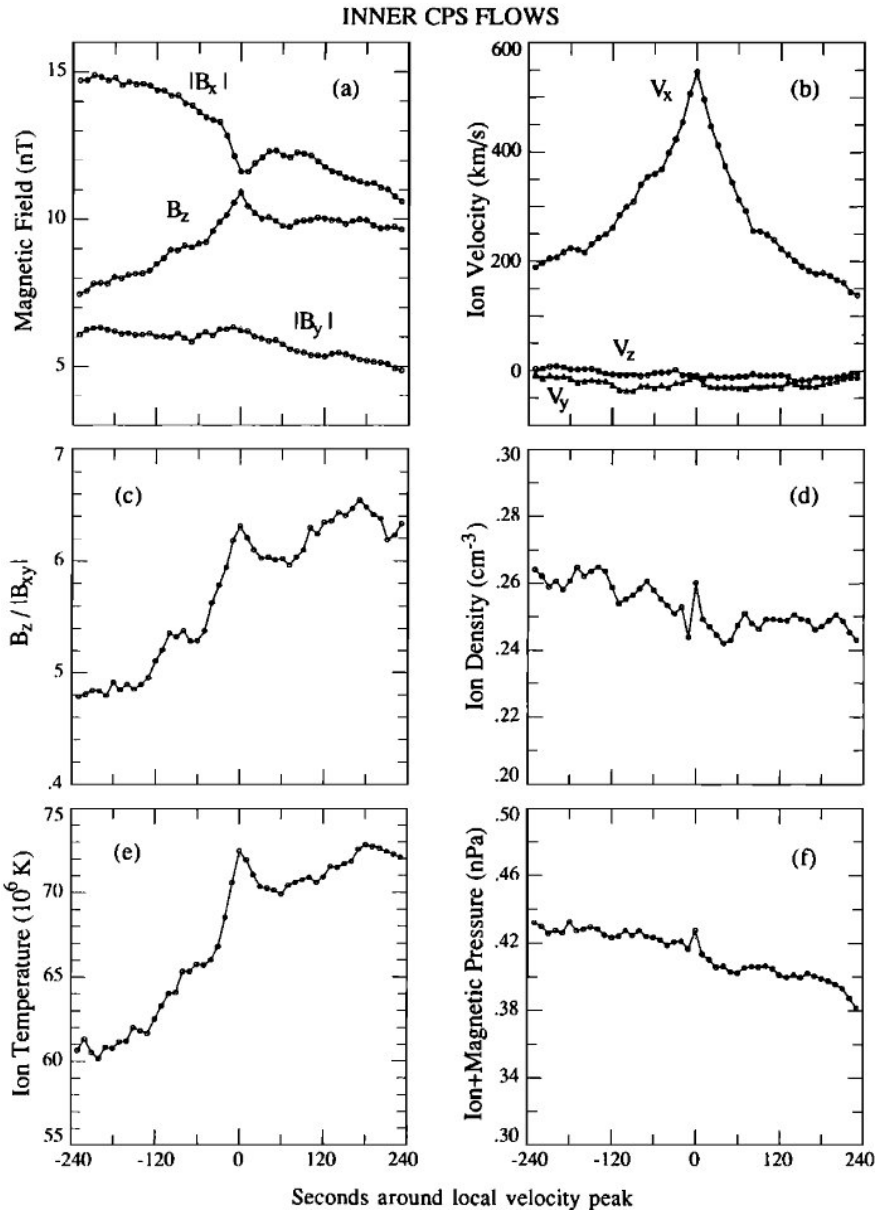

Figure 1.2: (After *Angelopoulos et al.* (1992)) Results of superposed epoch analysis applied to plasma and magnetic field data around inner central plasma sheet local velocity peaks above 400 km/s in the 1985-1986 AMPTE/IRM data base. The plasma and magnetic field data were time centered around each velocity peak ($t = 0$) and averaged over the database from -4 to $+4$ min. Shown are the resulting traces at 10-s resolution.

Nevertheless, the picture of CW93 can well represent the general life history of DFBs as a voyage from the near-earth reconnection site to geosynchronous orbit.

During their voyage towards Earth, DFBs produce many effects that are significant to magnetotail dynamics. For example, earthward DFB motion leads to particle acceleration (e.g., *Zhou et al.*, 2010; *Fu et al.*, 2011, 2013), so DFBs are a source of energetic particle injections into the inner magnetosphere (e.g., *Moore et al.*, 1981; *Gabrielse et al.*, 2012; *Runov et al.*, 2013). The DFB's role in magnetotail goes much beyond solving the pressure crisis. It is especially important during active times, e.g., during substorms and steady magnetospheric convection, when DFBs are more often observed. Understanding DFB properties will greatly improve our knowledge of magnetotail dynamics, especially during active times.

In this thesis I deal with three unresolved topics related to DFB properties. First, I establish the importance of magnetic flux transport by DFBs to magnetotail convection. Second, I study the mechanisms controlling DFB motion and the effects of that motion. Last, I investigate the current system surrounding the DFB. In the following, I introduce the importance of and some background about each topic. I also include more specific information about each topic in the introduction section of the chapter devoted to that topic.

1.2 Flux transport of DFBs

As DFBs have strong magnetic field and travel fast, they are expected to transport much of the magnetic flux in the near-earth magnetotail ($X > -30$ R_E). Therefore, they may play an important role in magnetotail convection. When DFBs are generated by near-earth tail reconnection, the magnetic flux in the lobe is transferred to DFBs, which in turn are transported to the inner magnetosphere. Since the likelihood of reconnection is related to the amount of flux in the lobe, DFBs act to reduce the likelihood of reconnection by transporting the lobe flux away. Understanding the importance and properties of DFB flux transport will greatly enhance our understanding of near-earth tail reconnection and convection.

Chen and Wolf (1993) roughly estimated the DFB flux transport by calculating the ratio of cross-tail potential contributed by plasma bubbles (DFBs) to the total cross-tail potential (which is also the percentage of magnetic flux transport DFBs account for) and found that their models result in a ratio up to 80%. Because CW93 set in the calculation a mechanism that bubbles exchange particles with their surroundings, which makes them dissolve, the flux transport ratio of DFBs decreases monotonically towards the inner edge of the plasma sheet. Nevertheless, the CW93 result suggests the importance of DFB flux transport from the theoretical perspective.

On the observational side, *Angelopoulos et al.* (1994) estimated the flux transport of bursty bulk flows that are closely related to DFBs. *Angelopoulos et al.* (1994) found that although BBFs last at most 10-15% of the time when the satellites were in the central plasma sheet, they are responsible for at least 30% of the total measured earthward transport and 60-100% of the transport closer to apogee ($\sim$ 20 R_E) and at midnight, i.e., in the regions of maximum BBF occurrence rate. Therefore, BBFs are a major and high-efficiency flux transporter in the tail.

Theoretical work and observations of BBFs have indicated the importance of DFBs in magnetotail flux transport. Bursty bulk flows are not DFBs, however; they also include flows outside the dipolarized magnetic field regions. An observational investigation of the flux transport properties of DFBs themselves is not yet available.

1.3 Causes and results of DFB motion

Dipolarizing flux bundles are most likely generated by tail reconnection (e.g., *Runov et al.*, 2009; *Angelopoulos et al.*, 2013). After being ejected earthward, they join the dipole field near the inner edge of the plasma sheet. Although earthward motion of DFBs has been observed for over 40 years (*Russell et al.*, 1971), a consensus has not been reached about the mechanisms that control this motion. Only by knowing these mechanisms can one understand the evolution of DFBs and their effects on magnetotail configuration. For example, the origin of the often-observed tailward DFB-related flows earthward of 20 R_E downtail is still not clear:

they could be related to flow vortices (*Fairfield et al.*, 1998), overshooting during braking (*Chen and Wolf*, 1999), or DFB-related velocity shear (e.g., *Sergeev et al.*, 1996). These different scenarios can only be distinguished from one another if the mechanisms responsible for DFB motion are understood.

A simple picture of DFB motion has been developed in the context of the interchange instability (*Chen and Wolf*, 1999). However, after applying the classic analytic criterion of interchange instability to observations, *Lee et al.* (2012) found that near-tail configuration before and during a DFB is statistically stable against the interchange mode. This suggests that the interchange instability resulting from an incoming DFB (e.g., the first in a series) is unlikely to trigger the generation of new, substorm-associated, DFBs (most DFBs are associated with substorms). Recently, *Wolf et al.* (2012) modified the theory of interchange mode-induced motion of DFBs. In their ideal MHD simulation, a stable system is disturbed slightly by the introduction of a bubble which then executes a decaying oscillation called an "interchange oscillation". The oscillation is in good agreement with the observations of braking and rebounding of tail flow bursts (*Panov et al.*, 2010).

Acceleration and deceleration of DFBs are controlled by the plasma pressure gradient force and the $\mathbf{j} \times \mathbf{B}$ force. In the MHD approximation the $\mathbf{j} \times \mathbf{B}$ force expresses itself as magnetic curvature force and magnetic pressure gradient force. The magnetic pressure is often considered together with the plasma pressure. In the *Chen and Wolf* (1999) picture, the magnetic curvature force accelerates the "filament" (transient flux tube) in the early stages but the effect of the curvature force reverses when the filament reaches the flow-braking region. Using THEMIS multi-point observations, *Li et al.* (2011) showed that the magnetic curvature force can still accelerate the DFB at 9 R_E downtail. However, this is opposite to the general trend of DFB motion, namely a deceleration after generation (e.g., *Shiokawa et al.*, 1997). More studies are needed to resolve the factors that control DFB motion.

Dipolarizing flux bundle motion brings pressure and flow perturbations to the ambient plasma. Simulations predict that the pressure perturbation builds up most strongly at the DFB's meridian of symmetry (e.g., *Yang et al.*, 2011). The flow perturbation is two vortices

on each to the dawn and dusk sides of the DFB (e.g., *Birn et al.*, 2004a; *Keiling et al.*, 2009). It has been suggested that these pressure and flow perturbations lead to generation of field-aligned currents (e.g., *Xing et al.*, 2011; *Birn et al.*, 1999), which form part of the DFB's current system.

1.4 The DFB-associated current system

The sharp jump in B_z at the leading edge of the DFB, the dipolarization front (DF), indicates that a strong, duskward, vertical current sheet flows along the DF. This duskward current must close elsewhere, so a DFB is associated with a system of currents. As the DFBs are one of the most important observables during substorms (e.g., *Angelopoulos et al.*, 2008a), their current system should be closely related to the substorm current wedge (SCW) (*McPherron et al.*, 1973), the major modification a substorm makes to the tail current system. Therefore, knowledge of the DFB current system will greatly improve our understanding of the substorm process.

Previous works have suggested that a SCW is generated as DFBs are decelerated in the flow-braking region near geosynchronous orbit. Flow braking creates inertial current (*Shiokawa et al.*, 1997), shear current (the shear of the flow generates a current due to the vorticity) (e.g., *Birn et al.*, 1999), or pressure-gradient driven currents (e.g., *Xing et al.*, 2011). These currents close through the ionosphere along field lines to form a wedge-like loop.

Alternatively, the SCW may be explained as redistribution of the current that has been carried by the DFB once it reaches the inner magnetosphere. To produce the $\sim$ 20 nT jump in B_z at the arrival of the $\sim$ 1000-km thick dipolarization front, the vertical current sheet at the DF must have a current density of $\sim$ 30 nA/m^2. Considering that $\sim$ 30 nA/m^2 is a large value compared to the current density in the horizontal cross-tail current sheet (2-6 nA/m^2), the DFB-associated current system significantly modifies both the local and global current systems. It is therefore important to understand how DFB currents close. *Nakamura et al.* (2001) discussed the redirection of the cross-tail current sheet (along the magnetic field

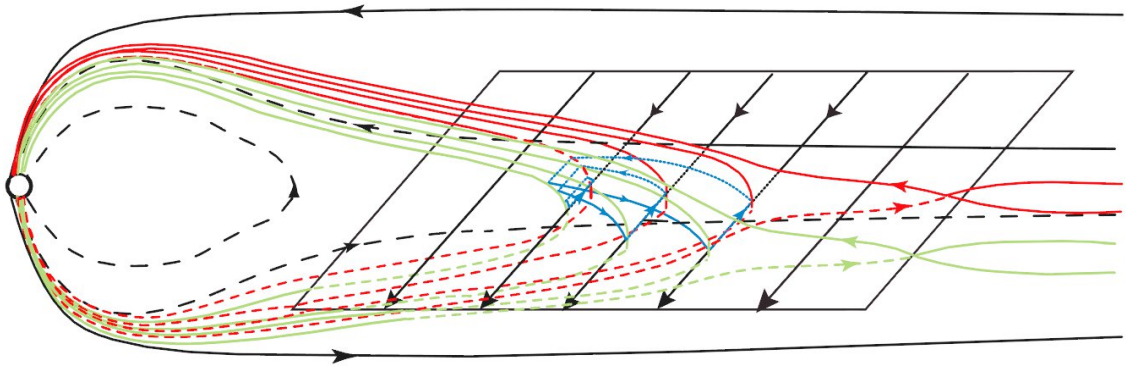

Figure 1.3: (After *Zhang et al.* (2011)) Cross-tail current diversion at the meridian of the DFB. With the arrival of the DFB, originally stretched tail-like field lines become more dipolarized (red at the DFB's dawnside and green at its duskside). Outside the meridian of the DFB, the field lines remain stretched (black field lines), and the current sheet retains its horizontal structure (black lines along neutral sheet). Redistribution of the horizontal cross-tail current at the sector of the DFB occurs in the radial direction (earthward/tailward) via cross-field currents (blue lines) and feeding the intense duskward current of the dipolarization front (blue azimuthal lines).

lines) into the ionosphere at the dawnside and out of the ionosphere at the duskside in the context of the PW90 and CW93 scenario (Figure 1.1). Such a combination of field-aligned currents (FACs) is called "region-1 sense" (the opposite direction is region-2 sense). In the recent study by *Zhang et al.* (2011), however, a significant reduction in the tail lobe flux was observed after the DFB passed, indicating a reduction in the cross-tail current in the rear side of the DFB. In addition, the magnetic topology at the dawn and dusk edges of the DFB (strong B_z inside and low B_z outside) necessitates cross-field currents in the earthward and tailward directions, respectively. The entire DFB current loop is illustrated in Figure 1.3. In this picture, the currents related to DFBs can close within the DFBs themselves without going to the ionosphere. Later, when the DFB approaches Earth it encounters the strong magnetic field of the near-Earth region, at which point there is no necessity for the duskward vertical current sheet at the dipolarization front (the enhanced magnetic field inside the DFB has merged with the Earth's strong dipole field). The earthward/tailward current densities at the sides of the flow burst must therefore close into the ionosphere with field-aligned currents along the dawn and dusk edges of the DFB, and this new loop is the SCW.

The *Zhang et al.* (2011) picture of the DFB current loop was introduced theoretically

by *Birn et al.* (2004a). In their 3-D MHD simulation, dawnward currents on the inner edge of the DFB and increased duskward currents on the outer edge are reproduced. These currents form extended layers in X and close around the DFB through northward and southward currents. *Birn et al.* (2004a) also reproduced the field-aligned currents suggested by CW93 and *Nakamura et al.* (2001) in the final stage of the DFB. In the *Birn et al.* (2004a) study these currents are discussed in terms of pressure gradient-driven currents arising from reconfiguration of the inner magnetosphere after flow arrival. However, it is unclear whether this scenario is consistent with observations. Further understanding of this scenario as well as other aspects of the DFB current system requires more comprehensive studies.

1.5 Outline of study

In this thesis, I use statistical studies to reveal flux transport properties of DFBs, the controlling factor and results of DFB motion, and the properties of the DFB-associated current system.

In Chapter 2, I build the database used for the statistical studies. I introduce the THEMIS data types I used and how I manipulate them. From THEMIS data I build an events list of DFBs using criteria based mainly on the sharpness of the B_z jump at the dipolarization front. This DFB list is utilized in Chapters 2 through 5. I also build an event list of bursty bulk flows from THEMIS data using the *Angelopoulos et al.* (1992) criteria. This BBF list will be used in Chapter 3. In Section 2.3 of Chapter 2, I infer the topology of DFBs because it is the basis for the statistical methods in later chapters. Using the normal direction of the dipolarization front, I determine that a DF is saddle-shaped. Therefore, it most likely has the shape of a dipolarized flux tube. In addition, using multi-point observations, I determine that DFBs have a typical width of $\sim 1 - 3$ R_E.

In Chapter 3, I investigate the importance and properties of DFBs in tail flux transport. I show that although BBF-embedded DFBs occupy only only $\sim 30\%$ of BBF duration, they contribute $\sim$ 70% of BBF magnetic flux transport. Therefore, because BBFs are major magnetic flux transporters in the magnetotail, DFBs are also major flux transporters in

near-earth tail convection. In this chapter I also show various DFB flux transport properties depending on tail location and geomagnetic activity. Due to the DFBs' importance, these characteristics may shape the entire near-earth magnetotail convection.

Chapter 4 discusses the factors that control DFB motion and the effects arising from DFB-motion-caused pressure and flow perturbations. The results show that DFB motion causes the total pressure to build up inside the DF layer, which exerts a tailward pressure gradient force that slows down the DFB's earthward motion. Then I establish that the pressure most relevant to DFB motion is a modified total pressure that is effective only in the radial (relative to the DFB center) direction. This radial total pressure also builds up inside the DF layer. On a statistical basis, the tailward radial total pressure gradient force is comparable to the magnetic curvature force, so the DFB is in approximate force balance. Based on results in Chapter 3, I conclude that in a statistical sense the pressure gradient force is a little higher than the curvature force earthward of 15 R_E downtail, whereas the curvature force is stronger beyond 15 R_E downtail. Dipolarizing flux bundle motion also builds up thermal pressure earthward of it; the buildup is strongest at the DFB's meridian of symmetry. When combined with the flux tube volume distribution around the DFB, such thermal pressure buildup requires generation of region-2-sense FACs earthward of the DFB and region-1-sense FACs inside the DF layer.

In Chapter 5 I infer the DFB current system from magnetic field variations. The field variations indicate the existence of region-2-sense FACs earthward of the DFB and region-1-sense FACs inside the DF layer, consistent with what is required by the pressure distribution in Chapter 4 and in a configuration to that of a substorm current wedge. I investigate the region-1-sense FACs inside the DF layer and find that they are more prominent away from the neutral sheet and at the DFB's flanks. The density variation of the DF current suggests that it is connected to the cross-tail current. Also from the DF current density I estimate that the amount of current carried by several DFBs is enough to form a SCW of typical strength. I conclude that DFBs are "wedgelets"—the traveling building blocks of the SCW.

In Chapter 6, the results of this thesis are summarized.

CHAPTER 2

Dataset and methodology

All my studies, which are based on data from the Time History of Events and Macroscale Interactions during Substorms (THEMIS) mission, are statistical. Using THEMIS observations, I built lists of dipolarizing flux bundle (DFB) and bursty bulk flow (BBF) events that enabled me to investigate various attributes of DFBs. In this chapter I briefly introduce the THEMIS mission and how I use its data. Then I explain how I select DFBs and BBFs from THEMIS measurements. To provide a basis for the methodology in later chapters, I infer that a DFB has the shape of a dipolarized flux tube with a Y-width of 1-3 R_E.

2.1 THEMIS data

THEMIS consists of five satellites (probes P1-P5) that traveled through the magnetotail covering the region from 6 to 30 R_E downtail (*Sibeck and Angelopoulos*, 2008). The five satellites are equipped with identical instruments: a fluxgate magnetometer (FGM), an electrostatic analyzer (ESA), a solid state telescope (SST), and an electric field instrument (EFI). The FGM measures the direct-current (DC) magnetic field (*Auster et al.*, 2008). I used quarter-second resolution FGM data for dipolarization front normal determination and 3-second resolution spin-fit data for all other applications. The ESA measures 5 eV to 25 keV ion and electron distribution functions (*McFadden et al.*, 2008). The ESA data I use has been applied background (penetrating) electron removal and accurate subtraction of spacecraft potential. The SST detects high-energy (25keV to 1 MeV) ion and electron fluxes (*Angelopoulos*, 2008). The SST software enables sun-contamination removal, detector calibration, and accurate partial moment computation from energetic particles. For plasma

parameter computation I combined 3-second resolution fast-survey ESA and SST flux measurements; then I calculate the plasma pressure and flow velocity as the second and first moments of the combined fluxes, respectively. The plasma pressure was computed as a scalar with the simplifying assumption of isotropy. I used spin-fit EFI (*Bonnell et al.*, 2008) data to evaluate DFB flux transport and infer the convective velocity after correcting them (see Appendix A).

2.1.0.1 The convective velocity of the dipolarization front

When investigating the perturbations the dipolarizing flux bundle brings to the ambient plasma, I need the propagation speed of its leading edge, the dipolarization front. Since the frozen-in condition breaks down at the thin DF layer (e.g., *Runov et al.*, 2011), the plasma velocity cannot represent the propagation of the DF. As a magnetic field structure, the DF moves at the velocity of field lines $\mathbf{v_B} = \mathbf{E} \times \mathbf{B}/B^2$. Therefore, I calculate each DF's convective velocity v_{DF} as the average $\mathbf{v_B}$ over the DF layer using electric field data from the EFI (Appendix B explains how I mark the DF layer with t_{in} and t_{out}).

2.2 Event selection

My statistical database comes from THEMIS's four tail science mission phases plus one month of data prior to and after each phase for additional data coverage at the fringes of the central tail sector. Specifically, I selected events from 1 November 2007 to 30 June 2008, 1 December 2008 to 30 June 2009, 1 February 2010 to 30 June 2010, and 1 February 2011 to 31 July 2011. During the 2008 and 2009 tail seasons, the five probes traveled through the magnetotail with different apogees (*Sibeck and Angelopoulos*, 2008) P1 had an apogee of $\sim$ 30 $\mathrm{R_E}$; P2, $\sim$ 20 $\mathrm{R_E}$; and P3, P4, and P5, 10-12 $\mathrm{R_E}$ (all in downtail distance). The database contains all five probes' measurements from these two seasons. In 2010 and 2011, I only used P3, P4, and P5 (apogees at $\sim$ 12 $\mathrm{R_E}$ downtail) measurements because P1 and P2 moved to higher altitudes and eventually into lunar orbit to become the ARTEMIS (Acceleration Reconnection Turbulence and Electrodynamics of Moon's Interaction with the

Sun) mission. I consider only the measurements in the magnetotail, defined as the region of $-6\mathrm{R_E} < X < -30\mathrm{R_E}$ and $\sqrt{Y^2 + Z^2} < 12\mathrm{R_E}$. I also exclude observations made when the probes were in Earth's shadow.

2.2.1 Selection of dipolarizing flux bundles

My dipolarizing flux bundle selection criteria deal solely with the spin-fit magnetic field B_z. According to previous published work (e.g., *Runov et al.*, 2009), the dipolarization front's (the DFB's leading edge) most prominent signature is a sharp B_z increase. Therefore, my first criterion was that the B_z rate of change dB_z/dt exceeds a certain value. Because of this criterion's sensitivity to short-term field variations (from waves, thermal fluctuations, or plasma sheet flapping), I applied a three-point running average to the input data (for this dB_z/dt criterion only). This criterion alone does not rule out events that show only a transient fluctuation in their B_z profile but no net increase. Therefore, my second requirement was that the B_z value behind the DF be larger than that ahead of the DF by a certain value. After surveying several tens of DF events (including all those in *Runov et al.* (2011)), I were able to hone in on reasonable operational values for these criteria that enable DF event selection and noise exclusion:

1. $dB_z/dt > 0.5$ nT/s (applied on the three-point running average data). The first point that meets this criterion denotes the DFB's t_0.

2. The maximum B_z in the t_0 to $t_0 + 30$ s time range should be at least 5 nT greater than that in the $t_0 - 30$ s to t_0 time range (30 s is about half the typical extent of the DFB structure).

3. The maximum B_z in the t_0 to $t_0 + 30$ s time range should be greater than 5 nT.

Dipolarizing flux bundles are often observed in groups (e.g., *Zhang et al.*, 2011). The DF of the first DFB in each group usually exhibits the clearest, sharpest changes. Subsequent DFBs are deposited and interact with already-perturbed plasma, so they are rather perturbed in all observables. However criteria 1 to 3 are still able to pick some of the subsequent ones

up. To deal with the cleanest possible signatures for further study, I designed my analysis to select the leading DFB of each DFB group. Of the DFBs selected by criteria 1-3, I keep only those not proceeded by other selected DFBs within 3 min prior to t_0. Then I require the magnetic field to be relatively unperturbed prior to the DF arrival as follows (all applied to the time range from $t_0 - 3$ min to $t_0 - 30$ s):

4. $dB_z/dt < 0.25$ nT/s for the entire time range (using the three-point running average data).

5. The standard deviation about the mean B_z, $\sigma_{B_z} < 1.5$ nT.

6. The maximum B_z be smaller by 2 nT than that in the time range from t_0 to $t_0 + 30$ s.

Applying these criteria to my survey sample of events, I confirmed that they do a good job in keeping the leading DFB in each DFB group but removing subsequent perturbations.

When applied to the entire database, criteria 1 through 6 result in 1951 DF events. Fast-survey collection of particle distribution functions was available for 1329 of them, enabling accurate computation of plasma moments and, in particular, plasma pressure. Figure 2.1 shows the selected events' spatial distribution in the magnetotail. For the vertical axes of Figures 2.1b and 2.1d, which express the location relative to the neutral sheet, I do not use the distance from a model neutral sheet, as that introduces errors due to model efficacy, hinge point location, solar wind velocity fluctuations, and activity. Instead, I use the parameter $B_{\mathrm{q}x}/B_{\mathrm{lobe,q}}$ as a proxy for the observation point's distance to the neutral sheet prior to DF arrival, scaled to the typical cross-tail current sheet thickness ahead of the approaching front. In this ratio, $B_{\mathrm{q}x}$ is the quiet time average B_x before each DF arrival. I used the average B_x in the $t_0 - 3$min to $t_0 - 2$ min time range (I intentionally utilized only the early portion of the pre-DFB range to avoid any precursor effects from the approaching DF). To ensure that the signed value of $B_{\mathrm{q}x}$ in the ambient (pre-DFB) plasma can be used to classify the DFBs, I checked how often B_x changes sign from before DFB arrival ($B_{\mathrm{q}x}$) to after DF crossing (B_x immediately behind the DF, at the maximum B_z point of t_0 to $t_0 + 15$ s). I found that in 94% (1828 out of 1951) of the events, the sign of B_x remained the same on either side of the

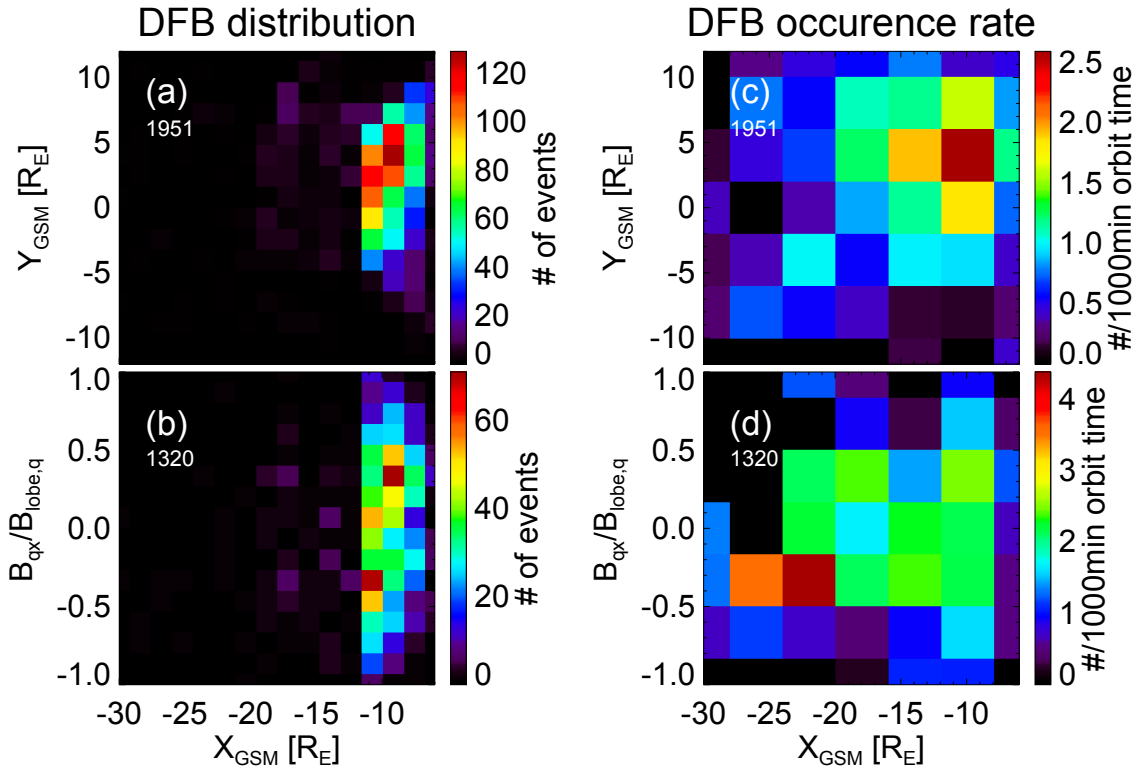

Figure 2.1: (a and c) Dipolarizing flux bundle event location distributions in the XY plane and (b and d) the X-neutral sheet distance plane. In Figures 2.1c and 2.1d, the event number in each bin is normalized to the probes' orbit time in that bin. $B_{qx}/B_{lobe,q}$ is a proxy of the probe's distance from neutral sheet, where B_{qx} and $B_{lobe,q}$ are the quiet time B_x and lobe field before each event, respectively. Figures 2.1a and 2.1c include all 1951 events. Figures 2.1b and 2.1d include only 1320 events because of limited high-resolution plasma data availability and data gaps.

DF. The lobe field $B_{\rm lobe}$ is inferred from the pressure balance assumption in Z direction:

$$B_{\rm lobe} = \sqrt{2\mu_0 P_{\rm total}}$$

where $P_{\rm total}$ is the average total pressure containing only B_x and B_y contributions (see *Xing et al.* (2009) for a detailed discussion of this choice). $B_{\rm lobe,q}$ is from the average $P_{\rm total}$ over the $t_0 - 3$min to $t_0 - 2$min time range. Nine of the 1329 fast-survey events have data gaps in the $t_0 - 3$min to $t_0 - 2$min time range, so 1320 events are shown in Figures 2.1b and 2.1d. Although most of my events are around the central plasma sheet, some are far from the neutral sheet. Because of the 12 R_E apogee and high eccentricity of the inner THEMIS probes, most events in Figures 2.1a and 2.1b are located around 10 R_E downtail.

Normalizing the event number in each bin to the THEMIS orbit time in that bin, I generate the event occurrence rate distributions shown in Figures 2.1c and 2.1d. Consistently increased occurrence rates are seen in the pre-midnight sector at $\sim$ 9 to 15 R_E downtail (Figure 2.1c). Previous statistical studies on magnetotail transients (e.g., *Schödel et al.*, 2001) have also shown that this region is the most active. Although the reasons for this preference are unclear, the effect is likely related to the well-known pre-midnight preference of substorm onset. Figure 2.1d shows that the DFB occurrence rate is higher inside the central plasma sheet ($|B_{qx}/B_{\rm lobe,q}| < 0.5$) than farther away from the neutral sheet. Although there are high DFB occurrence rates beyond 20 R_E downtail, these rates fluctuate significantly because the probes resided there only briefly.

To confirm my selection gives real dipolarizing flux bundles, in Figure 2.2 I do a superposed epoch analysis of key quantities surrounding DFBs from $t_0 - 2$min to $t_0 + 2$ min using t_0, the first point of sharp B_z jump at the DF (see selection criterion 1), as the epoch zero. Previously reported DF-related signatures (*Runov et al.*, 2009, 2011) are evidently showing up in my database: Figures 2.2a and 2.2i show the asymmetric B_z bipolar signature; Figures 2.2e and 2.2m show the earthward flow burst of 1min rise-and-fall time typically accompanying DFs (*Angelopoulos et al.*, 1992); Figures 2.2d, 2.2f, 2.2l, and 2.2n show the density and plasma pressure decrease behind the front; and Figures 2.2g, 2.2h, 2.2o, and 2.2p show

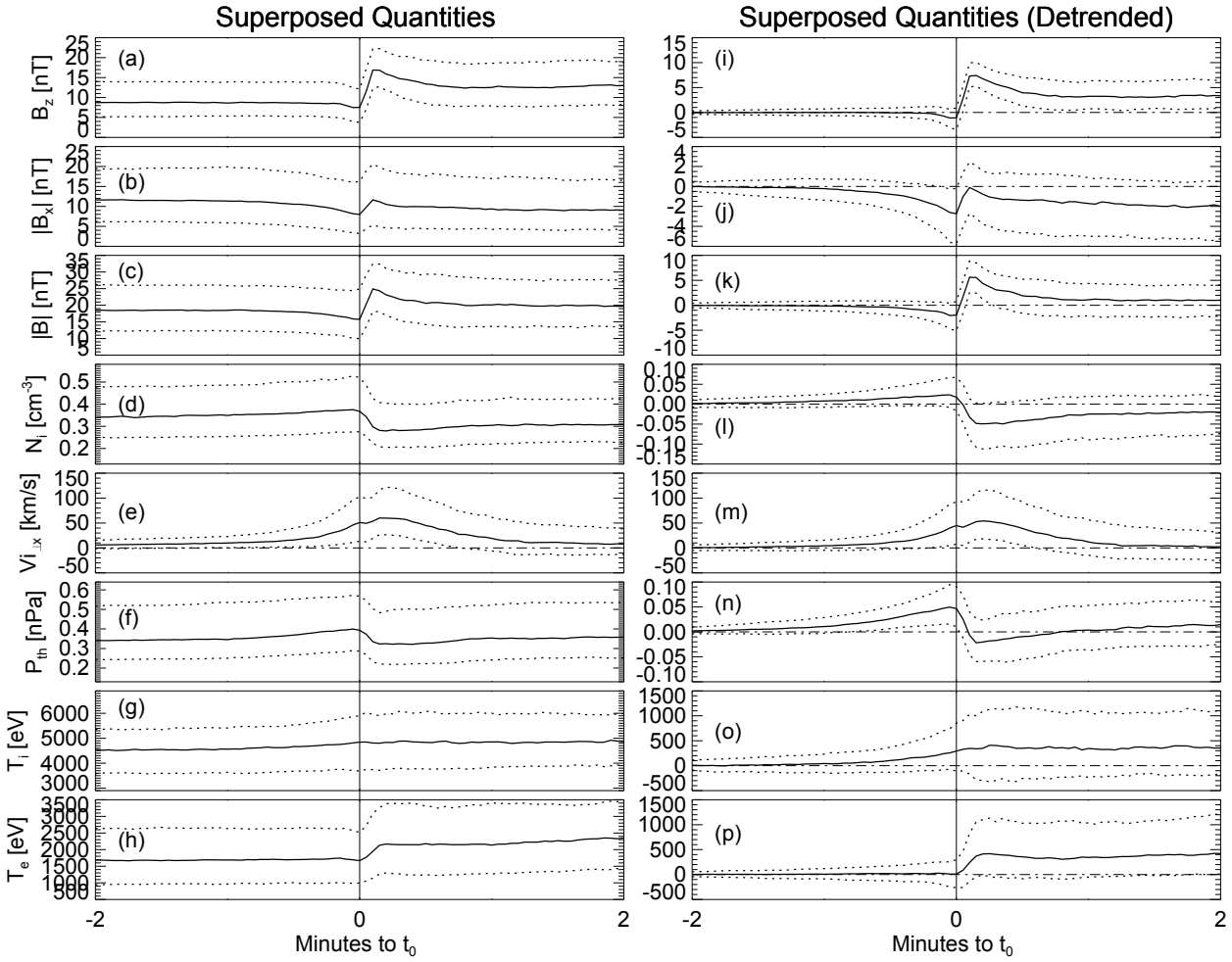

Figure 2.2: (a and i) Superposed epoch analysis of magnetic field z component, (b and j) magnetic field x component's absolute value, (c and k) magnetic field strength, (d and l) ion density, (e and m) perpendicular ion bulk velocity x component, (f and n) thermal (ion plus electron) pressure, (g and o) ion temperature, and (h and p) electron temperature. Figures 2.2i-2.2p represent the superposed epoch analysis of the quantities in Figures 2.2l-2.2h detrended with their average values of the time range $t_0 - 3$min to $t_0 - 2$min. The three curves in each panel are the upper quartile (dotted), median (solid), and lower quartile (dotted) of the superposed data. This figure includes only the fast-survey events (1329).

the temperature increase across the front. Even for the lower quartile in Figure 2.2a, the minimum value at the B_z dip is significantly higher than zero. In fact, only 13% of the DFBs have B_z dips that become negative ahead of them; most are inconsistent with the flux rope model hypothesis, which predicts the B_z dip to be a southward field. $|B_x|$ profiles in Figures 2.2b and 2.2j and total magnetic field profiles in Figures 2.2c and 2.2k also show asymmetric bipolar variations. The bipolar variations in $|B_x|$— and in field strength have profiles similar to the B_z bipolar signatures; they all minimize and maximize at the same time. The field strength variation casts more doubt on the efficacy of the flux rope explanation. In a flux rope, the magnetic field strength must be symmetric about the rope center: either peaked at the center or crater-like with a trough at the center and peaks on either side. Neither signature is observed based on my statistics. Figures 2.2g and 2.2o show that the ion temperature increases gradually beginning about 1min before DF arrival. This and the gradual increase in thermal pressure ahead of the DF (Figures 2.2f and 2.2n) have been interpreted by *Zhou et al.* (2010, 2011) as DF precursor signatures caused by ions accelerated after reflection at the DF. These signatures extend ahead of the DF near the equatorial plane over a scale comparable to the ion gyroradius in the ambient B_z. The electron temperature in Figures 2.2h and 2.2p, on the other hand, jumps near DF: the rise occurs only over a scale comparable with the B_z jump, even though it lasts for minutes afterwards. The electron energization may be due to betatron or Fermi acceleration (*Birn et al.*, 2004b; *Fu et al.*, 2011) or both. All the quantity profiles in Figure 2.2 confirm that my selection criteria picked up real DFBs.

In the following chapters I utilize this list of leading DFBs, which posses cleanest signatures unaffected by ambient perturbations, for statistical studies.

2.2.2 Selection of bursty bulk flows

To compare the DFB flux transport to that of BBFs in Section 3.3.1, I build a BBF event list using the same selection criteria as *Angelopoulos et al.* (1992): First I identify the central plasma sheet where the ion pressure is > 0.01 nPa and the plasma beta > 0.5. There I select each BBF as (1) a continuous > 100 km/s flow with at least one point > 400 km/s or

(2) a time range that contains two or more > 400 km/s points separated from their nearest neighbors by less than 10 min. The first time the flow exceeds 100 km/s marks a BBF's start time t_0; the last time the flow is above 100 km/s ends the BBF. With these criteria I identified 1208 BBFs.

2.3 The topology of dipolarizing flux bundles

The experimental designs in later chapters are based on the shapes and sizes of dipolarizing flux bundles. From the normal direction of the dipolarization front (DF, the leading edge of a DFB), I infer that an equatorial cross section of a DFBs' leading portion is convex when viewed from Earth; its meridional cross section is concave, similar to that of a dipolar flux tube. When viewed in three dimensions, the leading edge of a DFB resembles a saddle. The typical Y-width of a DFB is 1-3 R_E.

2.3.1 Background

Chen and Wolf (1993) suggested the simplest model for DFB topology—it resembles an ordinary dipolar flux tube (Figure 1.1). Thus, any dipolarization front's sagittal section (note: a sagittal section, a cross section that divides a body into right and left halves, is used here to refer to a DF cross section parallel to the XZ plane, or the DF's meridional cross section; the plane containing this section is a sagittal plane) including the DF mid-sagittal section (which bisects the DF into equal dawn and dusk halves; the plane containing the mid-sagittal section is the midsagittal plane) will have the shape of a dipolarized magnetic field line (Figure 2.5a). Magnetohydrodynamic (MHD) simulations by (*Birn et al.*, 2004a) indeed reveal such a dipolar cross section of the DFB.

Observations showing that B_z dips slightly ahead of the DFB complicates our understanding of DFB topology in that plane. The B_z profile around a DFB is thus at first decrease, then increase. If the DFB topology is consistent with the *Chen and Wolf* (1993) picture, such B_z variation can be produced by a finite vertical current sheet inside the DF layer (*Liu et al.*, 2013d). On the other hand, such magnetic field variation is also similar to

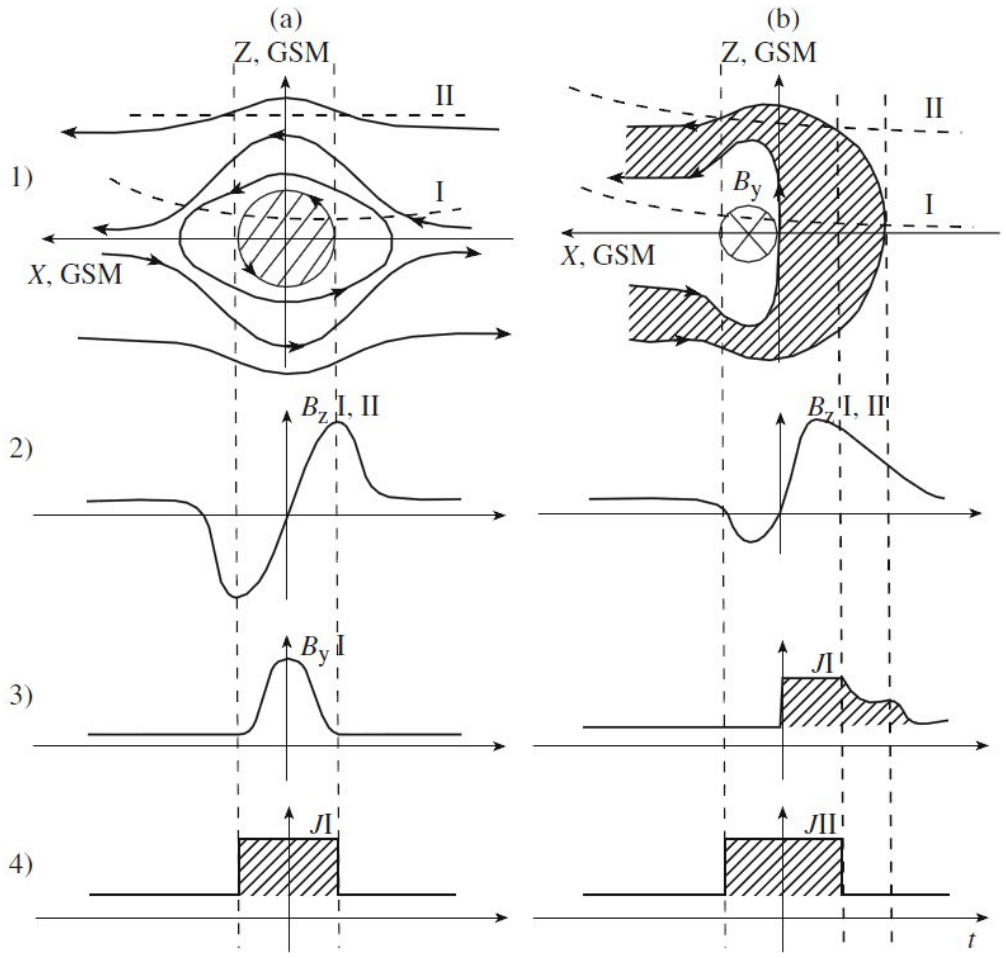

Figure 2.3: (After *Sormakov and Sergeev* (2008)) Examples of two types of structures: (a) magnetic flux rope and (b) single reconnected tube and variations in the magnetic field components and energetic electron flux (J) corresponding to them on various trajectories of the spacecraft (I and II).

the expected signatures of magnetic flux ropes, flux tubes formed by helical field lines (Figure 2.3a), and to the expected signatures of nightside flux transfer events (NFTEs, Figure 2.3b) (*Sergeev et al.*, 1992), structures generated when the background field is compressed ahead of earthward-moving reconnected flux tubes. In the flux rope interpretation, the sagittal cross-section resembles an egg (e.g., *Zong et al.*, 2004). In the NFTE interpretation, however, one expects a spindle-like (or teardrop-shaped) sagittal cross section (see *Sergeev et al.*, 1992, Figure 11a).

In both the NFTE and flux rope models, the B_z dip ahead of the DFB goes negative (Figures 2.3c and 2.3d). Figure 2.2a, however, shows that the B_z dip is far from being

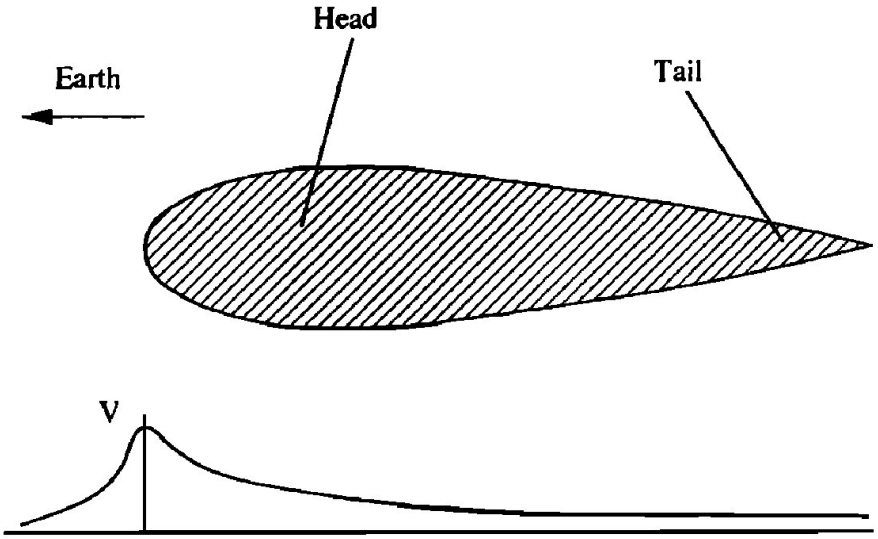

Figure 2.4: (After *Chen and Wolf* (1993)) A sketch of the equatorial cross section of a bubble.

negative even for the lower quartile of the superposed profiles, contradictory to the NFTE and flux rope models. Therefore, the dipolar flux tube picture is the most likely model for DFBs.

A DFB's transverse cross section (parallel to the XY plane) has been modeled as a teardrop (Figure 2.4) (*Chen and Wolf*, 1993) with its leading edge, the dipolarization front, being an approximate semicircle that is convex when viewed from Earth (Figure 2.5b). This shape arises from differential gradient/curvature drifts that tend to cause the DFB to "dissolve" into the surrounding medium. If a DFB is defined as an object that drifts with average low-energy ions, energetic ions would drift into the DFB from the dawnside, and low-energy ions would drift in from the duskside. The eastern and western sides of the DFB should have levels of $pV^{5/3}$, gradient/curvature drift current, electric field, and earthward flow velocity v_x that are intermediate between the values at the center of the DFB and those in the surrounding medium. A DFB of an initially arbitrary shape will deform such that the plasma on the east and west sides is dragged tailward relative to its center. From the head of a DFB to its tail, $pV^{5/3}$ is expected to increase monotonically; the $pV^{5/3}$ value near the tailward end of a DFB should be close to that of the surrounding medium. Moreover, the velocity peak is expected at the head of a DFB. Various simulations, such as the 3-D

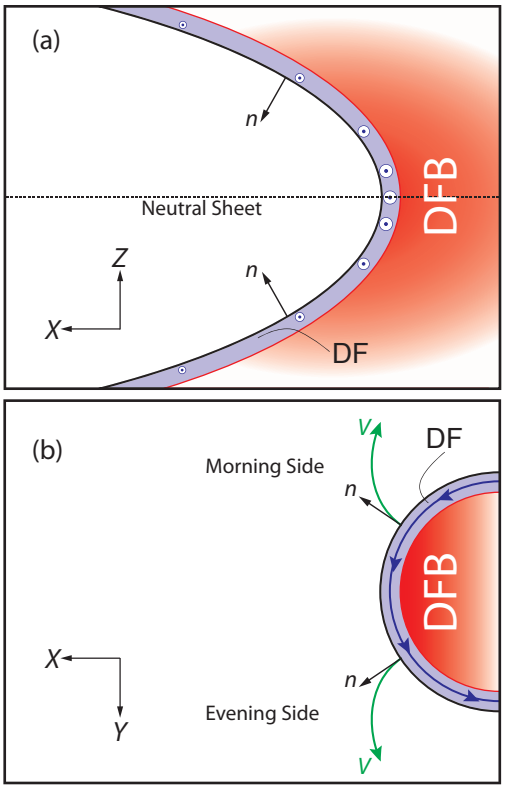

Figure 2.5: The (a) sagittal and (b) transverse sections of a dipolarizing flux bundle (DFB), adapted from (*Chen and Wolf*, 1993) and (*Sergeev et al.*, 1996). This figure shows the ideal case when the DFB moves entirely along the $+X$ direction. Current directions are indicated by blue arrows, and plasma bulk flow directions are indicated by green arrows. Red areas indicate strong magnetic field; the blue region is the dipolarization front. Morning/evening sides in panel b are relative to the DFB, a localized structure; they do not indicate the morning/evening portion of the magnetotail. A DFB can appear in any local time of the magnetotail.

PIC simulation of ballooning/interchange instability in the tail by *Pritchett and Coroniti* (2011) and the 2.5-D MHD simulation of multiple dipolarization fronts by *Guzdar et al.* (2010), have produced results consistent with this picture. Minimum variance analysis has confirmed the rounded head of the DFBs recently in the multi-case study by *Runov et al.* (2009) and earlier by *Sergeev et al.* (1996). *Sergeev et al.* (1996) also estimated that the semicircular cross section of a DFB's leading portion has typical radius of 0.5-1.5 R_E, which means the typical DFB width in Y is 1-3 R_E.

Even though the above theoretical and observational investigations of the DFB topology have been done, more comprehensive studies are still necessary. In the following I infer the

typical shape and size of the DFBs with the DF normal directions determined in Appendix B. Because of limited number of tailward-normal dipolarization fronts (I defined the normal direction as pointing from the DFB interior towards the ambient plasma. So a tailward normal direction means that the satellite enters the DFB from its tailward side. A tailward-normal event is approximately equivalent to a tailward-moving event), in this section I focus on the topology of earthward-normal DFs (see Appendix B for detailed explanation of the two types of DFs).

2.3.2 Results

2.3.2.1 The shape of the sagittal cross-section

As I discussed in Section 2.3.1, the sagittal section of a dipolarization front most likely conform to the shape of a dipolarized magnetic field line (see Figure 2.5a). When an earthward-normal DF is observed north (south) of the neutral sheet, its normal direction points southward (northward). As one moves away from the neutral sheet, the elevation angle of vector n relative to the XY plane ($\theta_{\mathbf{n}\text{-}XY}$) varies from 0° to 90° south of the neutral sheet and from 0° to 90° north of the neutral sheet. This effect is clearly evident in Figure 2.6 for all three earthward-normal event subsets corresponding to the different normal definitions (with the $\mathbf{B_{in}} \times \mathbf{B_{out}}$ method organizing the events best). In each subset, red dots correspond to events with a less than 30° angle between $\mathbf{n}$ and the XZ plane (defined as $\sin^{-1}|n_y|$). The $\sin^{-1}|n_y| < 30°$ events are interpreted as follows: assuming the DF's transverse (parallel to XY) cross section is convex (Figure 2.5b), a traversal with $\sin^{-1}|n_y| = 0$ corresponds to a crossing through the center of the structure. I refer to the point on the DF where $\sin^{-1}|n_y| = 0$ as a transverse cross section's "head point". The curve connecting the head points of all the DF's transverse cross sections is called the DF's "head line". In the ideal case when the head line lies on a plane parallel to the XZ plane, that plane is also the DFB's mid-sagittal plane. In reality the head line may distort away from the XZ plane; single spacecraft cannot sense this distortion. The red dots in Figure 2.6 are then observations near the DF's head line; they show cleaner trend (especially in Figures 2.6b and 2.6c) than

those far from the head line (black dots) do.

2.3.2.2 The shape of the transverse cross-section

Next I explore DFB's transverse (parallel to the XY plane) properties statistically by investigating the ambient plasma perturbation ahead of the DF. Following *Sergeev et al.* (1996), I expect flow perturbation ahead of a convex, earthward-normal DF to exhibit a component in the $+/-Y$ direction at the DFB's evening/morning side (Figure 2.5b). The probe's crossing point at the curved DF is indicated by the sign of n_y ($n_y < 0$ at the DFB's evening side and $n_y > 0$ at its morning side). Figure 2.7 shows a superposed epoch analysis of the perpendicular (to the magnetic field) ion bulk flow's dawn-dusk component $V_{\mathrm{i}\perp,y}$ for evening side ($n_y > 0.2$, Figures 2.7a, 2.7c, and 2.7e) and morning-side ($n_y < -0.2$, Figures 2.7b, 2.7d, and 2.7f) DF crossings. I intentionally exclude events near $n_y \sim 0$,where the effect is smaller and likely masked by waves, flow burst propagation velocity deviations, or external (solar wind) conditions. For all DF-normal determination methods, $V_{\mathrm{i}\perp,y}$ increases ahead of the DF at the DFB's evening side and decreases at its morning side, consistent with expectation. I also note that the median $V_{\mathrm{i}\perp,y}$ in the ambient plasma is always positive; around the DF, $|V_{\mathrm{i}\perp,y}|$ is larger on its evening side than on its morning side. (*Angelopoulos et al.*, 1993, 1994) attributed the ambient duskward flow to the azimuthal diamagnetic current in the plasma sheet, carried predominantly by thermal ions and caused by both neutral-sheet-ward and earthward pressure gradients. These pressure gradients and associated currents, which are still present (in fact, more intense) ahead of and during the passage of the flow bursts, can contribute to the dawn-dusk difference in peak $|V_{\mathrm{i}\perp,y}|$.

To confirm the convex shape of the transverse cross section, I investigate the occasions when two probes separated in the Y-direction observe the same DFB (a dual observation). (Note that a multi-point observation with three/four/five probes observing the same DFB can be split into three/six/ten dual observations.) For conciseness, I only investigate the dual observations of $\mathbf{B}_{\mathrm{in}} \times \mathbf{B}_{\mathrm{out}}$ events (see Appendix B for explanations). In this event subset, I identify a dual observation when two different probes observe events within 30s of

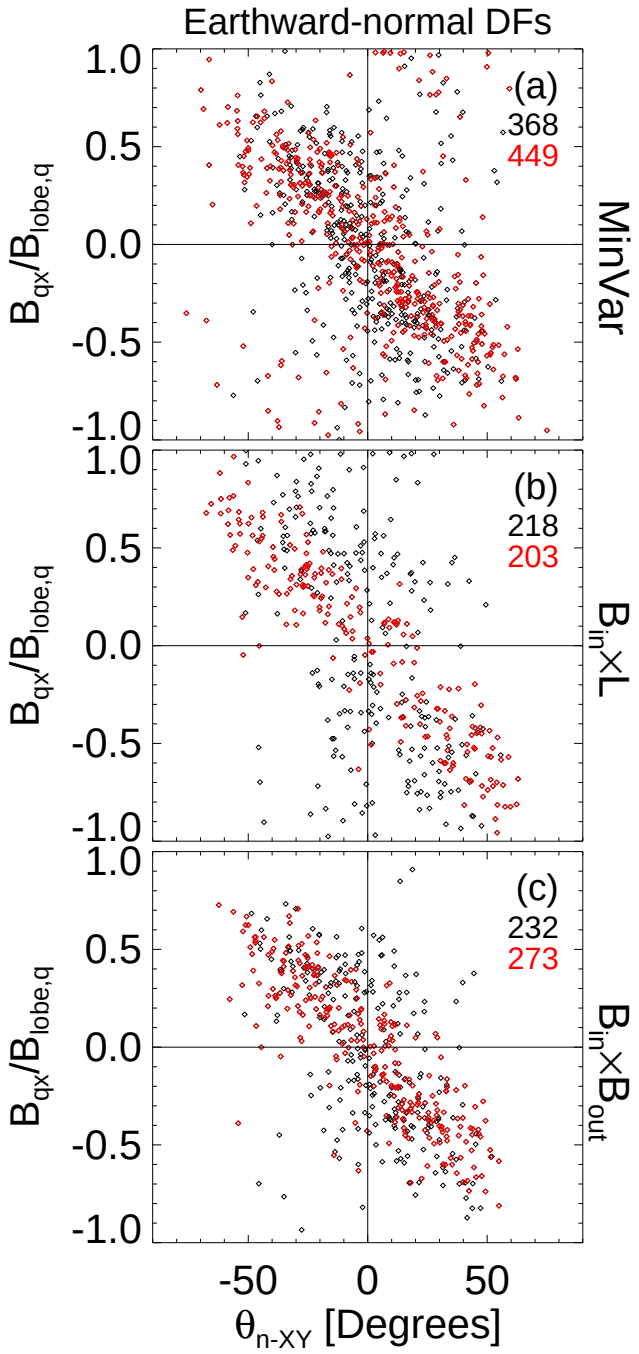

Figure 2.6: The earthward-normal dipolarization fronts' normal elevation angles from the XY plane ($\theta_{\mathbf{n}-XY} = \sin^{-1} n_z$) plotted against the proxy distance from the neutral sheet ($B_{\mathrm{q}x}/B_{\mathrm{lobe,q}}$) for (a) MinVar events, (b) $\mathbf{B_{in}} \times \mathbf{L}$ events, (c) and $\mathbf{B_{in}} \times \mathbf{B_{out}}$ events. Red points represent events with $|n_y| < 0.5$ (closest azimuthally to the DF's head line); black points represent the remainder of the events (near the DF's flanks). The black/red numbers in each panel are the total number of black/red dots (events) in that panel.

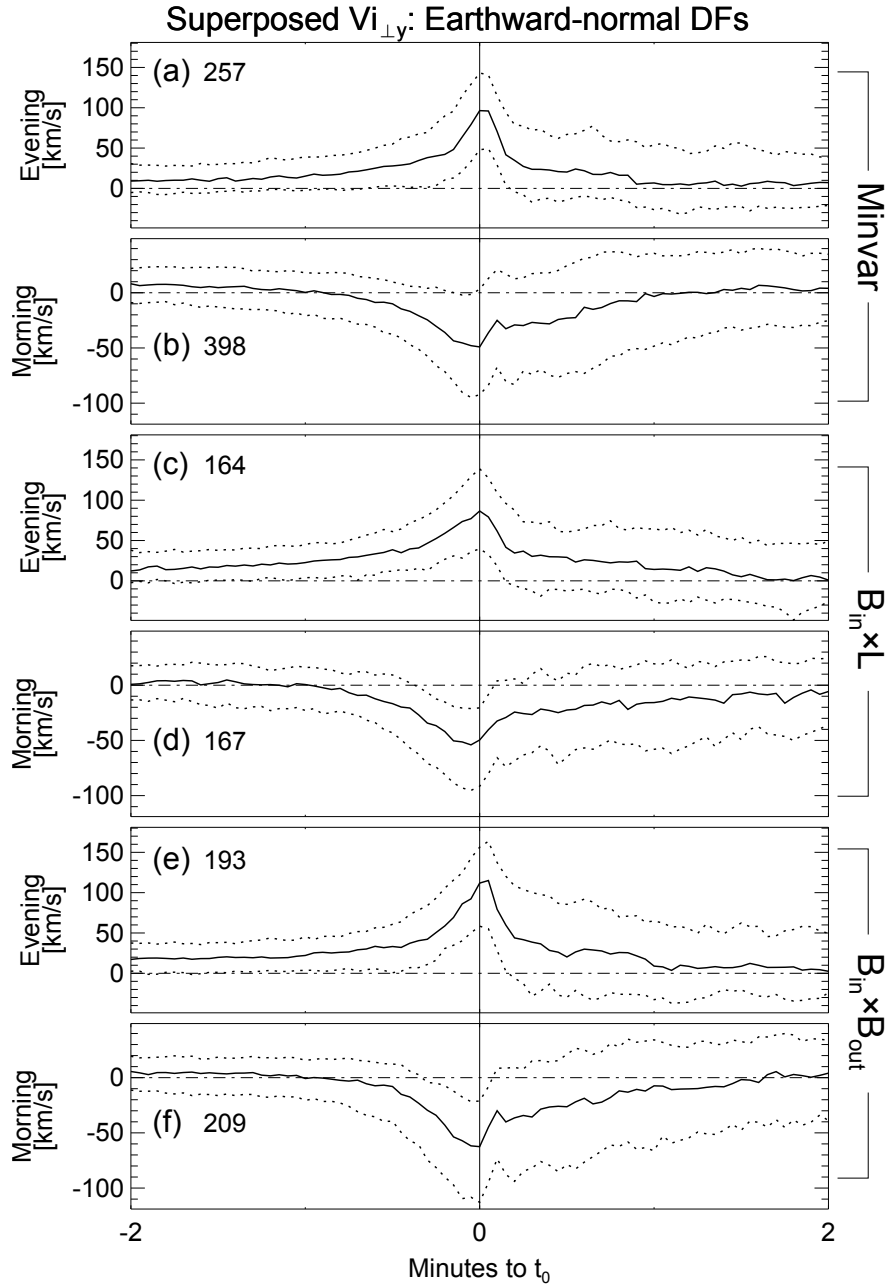

Figure 2.7: Superposed epoch analysis of $V_{\mathrm{i}\perp,y}$ for earthward-normal dipolarization fronts: (a and b) "MinVar" events, (c and d) $\mathbf{B_{in}} \times \mathbf{L}$ events, and (e and f) $\mathbf{B_{in}} \times \mathbf{B_{out}}$ events. The three curves in each panel are the upper quartile (dotted), median (solid), and lower quartile (dotted). "Evening" represents $n_y > 0.2$ in Figures 2.7a, 2.7c, and 2.7e; "Morning" represents $n_y < -0.2$ in Figure 2.7b, 2.7d, and 2.7f. The number in each panel is the total number of events used in that panel.

each other. To enable high-quality DFB radius estimation, I also require that the two probes making the dual observation have small X and Z separations ($\Delta X < 3$ R_E, $\Delta Z < 2$ R_E). Eighty-nine dual observations from the $\mathbf{B}_{in} \times \mathbf{B}_{out}$ events meet these criteria.

If the DFB's transverse cross section is convex, the probe more duskward of the DFB during a dual observation should see a more duskward-pointing DF normal direction: $\Delta n_y/\Delta Y$ should be positive, where Δn_y and ΔY are the difference between n_y and Y at the two probes. If the transverse cross section is concave, $\Delta n_y/\Delta Y$ should be negative. Using this $\Delta n_y/\Delta Y$ method, *Sergeev et al.* (1996) found that all five DFB dual observations they investigated using the ISEE 1 and 2 satellites were of DFBs with a convex transverse cross section. Applying this method to my 89 dual observations, I found that 66 (74%) are of DFBs with a convex transverse cross section. The remaining 23 dual observations are determined to be concave by the $\Delta n_y/\Delta Y$ method, perhaps because of DF surface ripples, distortion of the DFB flux tube, errors in DF normal determination, or observation of multiple DFBs. I also applied the $\Delta n_y/\Delta Y$ method only for cases where the two probes were on opposite sides of DFB's center, i.e., one on the dawn side and the other on the dusk side (as determined by n_y having opposite sign at the two probes). Of 27 such opposite-side observations, 23 (85%) showed convex transverse cross sections; the percentage of convexity increased.

2.3.2.3 The size of DFBs

That the transverse cross section of a DFB's leading portion is predominantly convex supports the assumption that it is a semicircle. I thus infer the DFB size by estimating the radius of this semicircle (hereafter referred to as the "DFB radius"). Using the dual observations, I make the estimation with two methods.

The first method roughly estimates the DFB radius as half the DFB width in Y by comparing the probes' Y separations during dual observations (Figure 2.8a) with those during single observations (Figure 2.8b). According to Figure 2.8a, most dual observations took place when the observing probes had less than 1.5 R_E Y-separation; none were made when the probes' Y-separation exceeded 3 R_E. If not biased by satellite orbits, such a

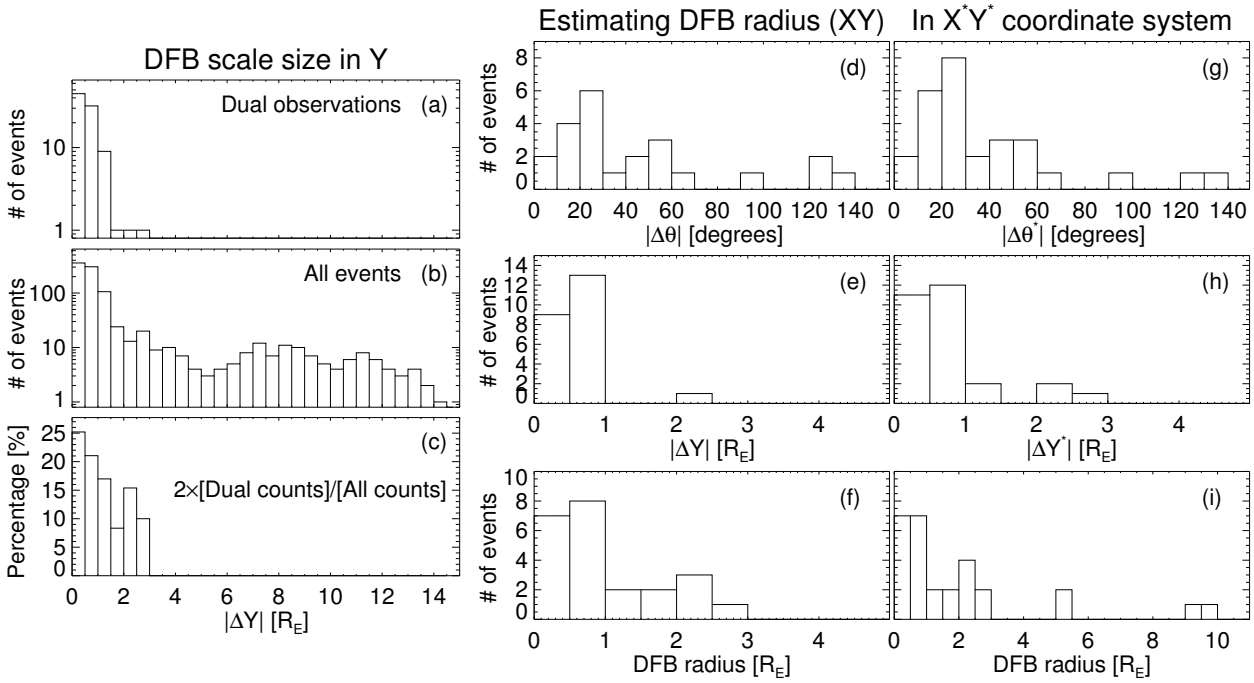

Figure 2.8: Estimates of the radius (half the width in Y) of the DFB's semicircular transverse cross section in histogram form. Figure 2.8a shows the Y-separation distribution for probes that made the 89 dual observations. Figure 2.8b is the distribution of Y-separation of other probes from the probe seeing the DFB for all the DFB encounters in my event list. In Figure 2.8c, the histogram in Figure 2.8a is divided by that in Figure 2.8b (the division is done for each individual bin in Y) and then doubled. Figures 2.8d-2.8f illustrate another way of estimating the radius from 23 dual observations made simultaneously at the dawn and dusk sides (two-side dual observations) of convex DFBs. Figure 2.8d is the distribution of the azimuth ($\theta = \text{atan}(n_y/n_x)$, it gives where on the DFB the probe hit it.) difference of the two probes making each dual-observation. Figure 2.8e is the two probes' Y-separation distribution, and Figure 2.8f is the calculated DFB radius distribution. Figures 2.8g-2.8i, which are ordered in the same way as Figures 2.8d-2.8f, show the radius distribution in the X^*Y^* coordinate system (results are from 28 two-side dual observations of convex DFBs).

distribution suggests that the DFBs are typically narrower than 3 R_E and thus have radii smaller than 1.5 R_E. To examine whether the distribution in Figure 2.8a is biased by satellite orbits, I show the histogram for all Y-separations in Figure 2.8b: for each of the 506 $\mathbf{B}_{in} \times \mathbf{B}_{out}$ events, I count the Y-separations from the probe observing the event to all other probes within 3 R_E in X and 2 R_E in $Z$of it, even if the other probes did not observe a DFB. Although most Y separations are within 2 R_E, the probes can be separated by up to 14 R_E; the histogram in Figure 2.8b has significant counts between 2 and 14 R_E (around 10 for each 0.5-R_E-wide bin). Therefore, the lack of dual observations beyond 3 R_E Y-separation in Figure 2.8a is due not to biased satellite orbits but to the less-than-1.5 R_E DFB radius. I obtain an estimate of the DFB radius in Figure 2.8c by dividing the dual-observation histogram in Figure 2.8a by the histogram of Figure 2.8b. I multiply the quotient by two because dual-observation separations are counted twice in Figure 2.8b but only once in Figure 2.8a. The normalized occurrence rate of a dual observation as function of the Y separation is shown in Figure 2.8c. As expected, smaller Y separations result in a higher likelihood of a dual observation. (Note that the observed, 25% likelihood at the smallest Y separation (0-0.5 R_E) is lower than expected given the anticipated 1-3 R_E-wide DFBs, mainly due to my strict selection criteria. Each of the dual-observation percentages for 1.5-3 R_E separations comes from only one count in Figure 2.8a, so their values are not quite suggestive.) In summary, Figures 2.8a-2.8c indicate that DFBs are usually narrower than 3 R_E and thus have radii smaller than 1.5 R_E.

I can also calculate the DFB radius r as follows (Figure 2.9a):

$$r = |\frac{\Delta Y}{\sin\theta_1 - \sin\theta_2}| \tag{2.1}$$

where θ_1 and θ_2 are the DF normal directions' (signed) azimuths from the X direction observed by the two probes making the dual observation. In this thesis "azimuth" and "azimuthal" are always relative to the DF/DFB's semicircular transverse cross section. The azimuth given by $\theta = atan(n_y/n_x)$ marks the point at which each probe crosses the DFB (black dots in Figure 2.9a). For precision, I apply equation 2.1 to only the 23 two-side dual

observations with a convex-DFB signature; the results are summarized in Figures 2.8d-2.8f. Figure 2.8f shows that the DFB radii never exceed 3 R_E and are usually less than 1 R_E. The median (average) DFB radius of these 23 dual observations is 0.8 (1.0) R_E, similar to the estimates in Figures 2.8a-2.8c and in the literature (e.g., *Sergeev et al.*, 1996; *Nakamura et al.*, 2004). Figure 2.8f also shows that the DFB radius can occasionally reach 3 R_E. Such a large radius has also been reported in previous studies (e.g., *Nakamura et al.*, 2001).

The above methods assume that the DFB's leading edge is its earthward edge and that it is symmetric about the X axis. Because the convex nature of the DFB's transverse cross section is a result of the DFB motion, a more precise assumption is that the DFB's leading edge is a semicircle symmetric about its direction of motion. Under this assumption, I can apply the same methods in a rotated coordinate (X^*Y^*) system, as illustrated in Figure 2.9b. Here the X^* axis, which represents the DFB's direction of motion, is given by the XY component of the DF convective velocity $\mathbf{v}_{DF}$ (for dual observations, X^* represents the XY component of the average $\mathbf{v}_{DF}$ measured by the two probes). The direction of Y^* is in the XY plane and is perpendicular to X^*. Transforming observations into the X^*Y^* coordinate system, I identified 35 two-side dual observations; each is a dual observation with the two probes observing the DFB having n_{y^*} of opposite signs. Twenty eight (80%) of these two-side dual observations show a convex DFB signature (positive $\Delta n_{y^*}/\Delta Y^*$). Next, I repeat the computation of the DFB radius from Equation 2.1 with these 28 two-side dual observations and display the results in Figures 2.8d-2.8i. The inferred radii have a median (average) of 1.0 (2.0) R_E. The radius histogram in Figure 2.8i drops sharply at 1 R_E and disappears beyond 3 R_E, confirming the typical DFB radius of 1 R_E. In Figure 2.8i the four counts at 5-5.5 R_E and 9-10 R_E are unreliable due to small transecting azimuth differences—$\Delta\theta^*$ ranges from 5° to 25° for these four cases—that causes the radius in Equation 2.1 to be dominated by noise. Without these the inferred radii have a median (average) of 0.9 (1.1) R_E. Therefore, the DFB topology (convex or concave transverse cross section) and scale size obtained in the X^*Y^* coordinate system are similar to those obtained in the GSM coordinate system.

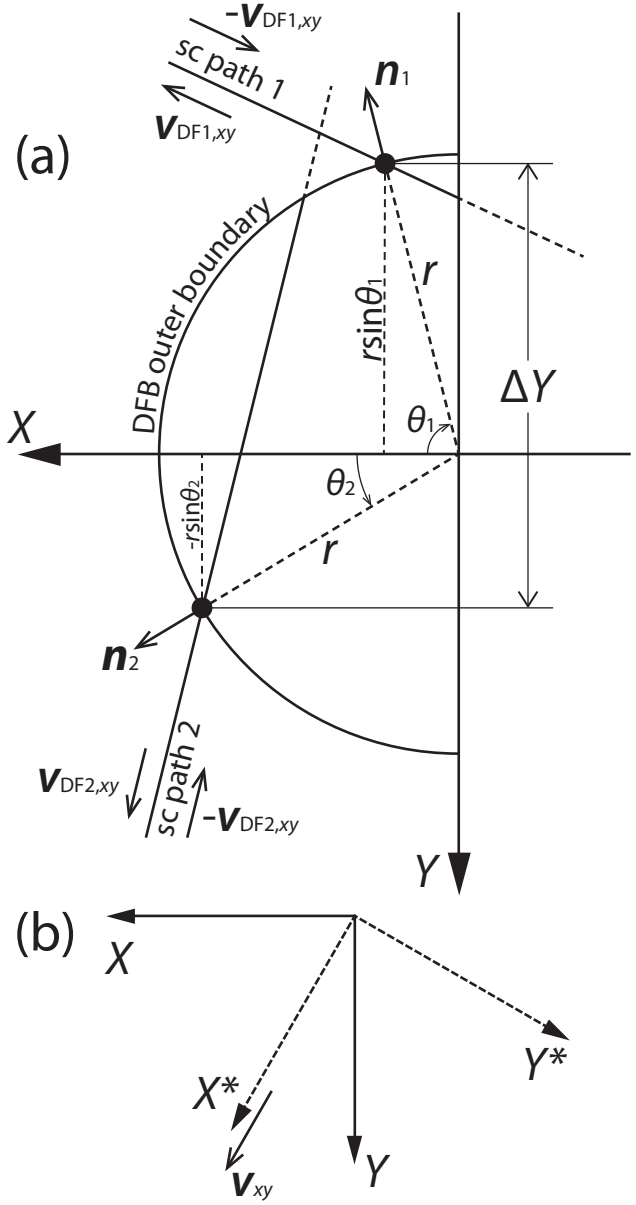

Figure 2.9: (a) Illustration of the DFB radius derivation from a dual observation. The DF convective velocities of the two encounters are represented by $\mathbf{v}_{\mathrm{DF1}}$ and $\mathbf{v}_{\mathrm{DF2}}$; the satellite velocities relative to the DFB are $-\mathbf{v}_{\mathrm{DF1}}$ and $-\mathbf{v}_{\mathrm{DF2}}$ (see Section 2.1.0.1 for how I obtain $\mathbf{v}_{\mathrm{DF}}$). Note that θ, the angle from X to the DF normal direction $\mathbf{n}$, is signed. The two black dots on the DFB outer boundary are satellite transecting points. (b) Illustration of the X^*Y^* coordinate system. For DFB radius derivation, the X^*-determining $\mathbf{v}$ is the average DF convective velocity of the two dual-observation encounters. For statistical quantity map reconstruction, $\mathbf{v}$ is each individual encounter's DF convective velocity $\mathbf{v}_{\mathrm{DF}}$.

2.3.3 Summary and discussion

I found that the shape of the earthward-normal DF's sagittal section (parallel to the XZ plane) is consistent with a quasi-dipolar magnetic field line; its transverse cross section (parallel to the XY plane) is convex when viewed from Earth. Therefore, the DF's 3-D shape is saddle-like and the DFB resembles a dipolar flux tube. The typical width of a DFB is 1-3 R_E. These informations on DFB topology are the basis for the methods in the following chapters. As we shall see in those chapters, although DFBs are small compared to the $\sim$ 30 R_E-wide near-earth magnetotail, they play a major role in the near-earth tail dynamics.

Given such a shape of the DFB, observations by multiple satellites and accurate normal determination are required to infer their timing and propagation speed and to interpret their internal processes, such as wave particle interactions, dissipation, and heating. For example, when two probes are separated only along Z, the one farther from the neutral sheet should observe an earthward moving DF first; when two probes are separated only in Y, the one closer to the DFB's midsagittal plane should detect an earthward moving DF first.

The DFB's shape allows the duskward current on the DF (e.g., *Runov et al.*, 2011) to affect the ambient plasma. Due to the DF's concave sagittal section, north of the neutral sheet, the presence of high-latitude (far from the neutral sheet) duskward current creates a negative B_x variation in the lower-latitude (closer to the neutral sheet) ambient plasma, reducing the ambient $|B_x|$ ahead of the DF at the lower-latitude location. South of the neutral sheet, the effect is the same, except that the B_x variation in the lower-latitude ambient plasma is positive, still reducing the ambient $|B_x|$. This effect can contribute to the slow $|B_x|$ and B decreases before DF arrival in Figure 2.2b, 2.2c, 2.2j, and 2.2k.

CHAPTER 3

Magnetic flux transport by dipolarizing flux bundles

Knowledge of a dipolarizing flux bundle's flux transport properties leads to better understanding of near-Earth ($X = -6$ to -30 R_E) magnetotail flux transport and thus conversion of magnetic energy to kinetic and thermal plasma energy following magnetic reconnection. To establish the importance of DFB flux transport, I compare it with transport by bursty bulk flows (BBFs) that typically envelop DFBs. Because DFBs coexist with flow bursts inside BBFs, they contribute $\sim$ 67% of BBF flux transport, even though they last only $\sim$ 30% as long as BBFs. The rate of DFB flux transport increases with proximity to Earth and to the pre-midnight sector, as well as with geomagnetic activity and distance from the neutral sheet. Under the latter two conditions the total flux transport by a typical DFB also increases. Dipolarizing flux bundles appear more often during increased geomagnetic activity. Since BBFs have been previously shown to be the major flux transporters in the tail, I conclude that DFBs are the dominant drivers of this transport. The occurrence rate of DFBs as a function of location and geomagnetic activity informs us about processes that shape global convection and energy conversion.

3.1 Introduction

Dipolarizing flux bundles are generated at 20-30 R_E downtail (*Runov et al.*, 2011), most likely by reconnection (e.g., *Angelopoulos et al.*, 2008b; *Sitnov et al.*, 2009; *Nagai et al.*, 1998; *Angelopoulos et al.*, 2013), and then move earthward. The DFBs' earthward motion results in 1-min timescale plasma flow bursts an order of magnitude larger than the quiet-time convection flow. Dipolarizing flux bundles and flow bursts are enveloped by 10min-

timescale intervals of enhanced bursty bulk flows (*Angelopoulos et al.*, 1992). On multiple fortuitous occasions, the THEMIS spacecraft have captured DFBs traveling coherently from the reconnection site to the inner magnetosphere within short-duration BBFs (*Runov et al.*, 2011); other times several DFBs have been observed together, one after another and their flows coalescence towards a long-duration BBF (e.g., *Zhang et al.*, 2011).

Due to its intense magnetic field and high speed, a DFB transports a large amount of magnetic flux within a short time. This flux is transferred from the tail lobes to the DFB during the reconnection process; as the field line shrinks and its equatorial footprint convects towards the inner magnetosphere magnetic energy is converted to plasma kinetic and thermal energy (*Angelopoulos et al.*, 2013). Therefore, DFBs take part in both magnetotail flux transport and energy conversion and are critical aspects of the *Dungey* (1961) global circulation cycle. Thus, clarifying the relative importance of DFBs for magnetic flux transport can improve my understanding of global magnetotail convection and energy transport.

Although the importance of fast flows for magnetotail convection varies with modes of convection (*Kissinger et al.*, 2012), *Angelopoulos et al.* (1994) made an overall estimation—BBFs contribute $60-100\%$ of the magnetotail flux transport in the $13-22$ R_E downtail region, even though they occur only $10-15\%$ of the time in the central plasma sheet. The percentage of total flux transport accomplished by BBFs reduces earthward of $X=-13$ R_E but can still reach $\sim 50\%$. Therefore, BBFs are the major flux carriers in the near-earth magnetotail. Early studies have demonstrated that the efficiency of transport by BBFs is due to the high degree of correlation between the 1-min timescale flow bursts and the Z-component of the magnetic field, i.e., the embedded DFBs (*Angelopoulos et al.*, 1992). But since a BBF contains not only DFBs but also flows outside the DFBs, it is unclear presently what fraction of the total BBF transport is accomplished by DFBs and, by extension, how important DFBs are for global flux circulation.

Another magnetotail transient phenomenon related to the DFBs is the "rapid flux transport event" (RFT), defined as an interval of high electric field (*Tu et al.*, 2000; *Schödel et al.*, 2001) (*Tu et al.* (2000) called RFTs "impulsive electric field" events). It is called an RFT because the electric field $\mathbf{E}=-\mathbf{V}_c\times\mathbf{B}$ represents the magnetic flux transport rate. Here $\mathbf{B}$

is the magnetic field; $\mathbf{V}_c$ is the convective velocity of the field line; it equals the perpendicular (to $\mathbf{B}$) component of the plasma bulk velocity $\mathbf{V}_c$ when the frozen-in condition is valid. A DFB, even though it is defined based on the magnetic field, is expected to possess also an RFT signature, since its strong magnetic field and flow lead to a strong electric field. The importance of RFTs in tail flux transport is suggestive of the DFB importance—groups of RFTs are observed only $\sim 5\%$ of the time in the central plasma sheet but are responsible for $\sim 30 - 50\%$ of the flux transport in the magnetotail (*Schödel et al.*, 2001). However, RFTs are not equivalent to DFBs as they may also include other types of tail transients with strong electric field.

On the theoretical side, *Chen and Wolf* (1993) made a rough calculation and showed that the potential drop across plasma bubbles (the theoretical model for DFBs) can be up to 80% of the entire cross-tail potential drop, indicating that DFBs might be expected to contribute up to 80% of the tail flux transport. On the observational side, *Li et al.* (2011) showed that the magnetic curvature force of the DFB is the driver of its associated BBF, and thus flux transport. However, to my knowledge only a few case studies show limited examples of the importance of DFBs (*Angelopoulos et al.*, 2013). A comprehensive study of DFB flux transport is needed to establish the DFBs' importance in magnetotail convection and energy circulation.

If DFBs accomplish significant flux transport in the tail, their spatial characteristics under different activity conditions can inform us about the drivers of large-scale, near-Earth tail convection. Previous studies of fast flows, BBFs and RFTs have indicated some of these characteristics. *Tu et al.* (2000) found that RFTs have preferentially higher flux transport rate at the dusk tail than at the dawn tail, implying a similar expectation for the DFBs. However, some results for fast flows and RFTs have been apparently contradictory. For example, *Hsu et al.* (2012) found that the flux transport rate of fast flows decreases with proximity to Earth, while *Tu et al.* (2000) found the RFTs' transport rate to increase. An investigation of DFBs, their transport and related flows ought to resolve these questions and reveal whether and how DFB flux transport characteristics affect global tail circulation.

In the following, I use statistical approaches to establish the importance of DFBs in near-

earth magnetotail flux transport and then examine the DFBs' flux transport characteristics as function of position and geomagnetic activity.

3.2 Dataset

Since the importance of bursty bulk flows in flux transport has already been established, I seek to determine the importance of DFBs by showing that those of them embedded in BBFs are the predominant flux carriers of those BBFs. I utilize the BBF event list I built in Section 2.2.2 for this study. To identify the DFBs inside these BBFs, I apply only the DFB selection criterion 1—the B_z jump sharpness criterion (see Section 2.2.1). Omission of criteria 2-6 allows the selection of both leading and non-leading DFBs. The BBF list and the DFB identification within them are used for constructing Figures 3.1 and 3.3.

For all other investigations of DFB properties, I use the leading DFB list built in Section 2.2.1 which results from the full set of selection criteria. The DFBs in this list have clean signatures unaffected by preceding perturbations such as interactions with the dipole. This leading DFB list is used in all figures except Figures 3.1, 3.3, and 3.8).

The flux transport of DFBs and BBFs is given by the time integration of the electric field which represents flux transport rate. As I am interested mainly in the flux transport along the sun-earth line, I investigate only the Y component of the electric field (E_y). In the magnetotail, this component represents the earthward transport of B_z and neutral-sheet-ward transport of Bx with the former dominating in most cases. Before using E_y measured by THEMIS's electric field instrument, I first correct the EFI data following the method in Appendix A.1. The Y axis of the despun satellite coordinate system, Y_{DSL}, is nearly parallel to Y_{GSM} for P3-P5 (on which the spin axis is roughly due ecliptic north) and nearly anti-parallel to Y_{GSM} for P1 and P2 (on which the spin axis is roughly due ecliptic south) (*Angelopoulos*, 2008). I thus use $E_{y,\mathrm{DSL}'}$ (DSL prime) to approximate $E_{y,\mathrm{GSM}}$. I define Y_{DSL}' as identical to Y_{DSL} for P3-P5 and opposite to Y_{DSL} for P1 and P2. Next, I remove the EFI offsets, one event at a time, by subtracting from $E_{y,\mathrm{DSL}'}$ its average value over the preceding ambient condition time range from $t_0 - 3\mathrm{min}$ to $t_0 - 2\mathrm{min}$ (see also Section A.1).

By subtracting the pre-event average value I also remove the flux transport of the ambient convection electric field, so the resultant $\delta E_{y,\mathrm{DSL}'}$ represents the flux transport rate of the DFB or BBF excluding the large-scale magnetotail convection. In practice, the large-scale, non-BBF convection is small compared to the BBF/DFB transport (*Angelopoulos et al.*, 1993), so $\delta E_{y,\mathrm{DSL}'}$ is very close to actual $E_{y,\mathrm{DSL}'}$. In the following sections I utilize $\delta E_{y,\mathrm{DSL}'}$ to study DFB flux transport properties.

3.3 Results

In this section I first establish that dipolarizing flux bundles are the major flux transporters inside bursty bulk flows and are thus important flux transporters in the magnetotail. Then I investigate DFB flux transport as function of equatorial location, distance from the neutral sheet, and AE index.

3.3.1 The importance of dipolarizing flux bundles for flux transport

First I identify the DFBs inside each BBF following the B_z jump sharpness criterion. Figure 3.1 shows an example of an $\sim$ 8-min-long BBF and the seven DFBs identified within it.

To compute the integral or average flux transport contributed by the DFBs I need to determine their durations. This is rather difficult to do because the field and plasma perturbations inside and surrounding a DFB are very complicated. As a compromise I define the duration of each DFB to be equal to the nominal, statistical duration of the ensemble of DFBs. To determine this statistical duration, in Figure 3.2a I superpose the B_z profiles of all DFBs in the leading DFB list. For the median profile in Figure 3.2a, I take the first point behind the dipolarization front which falls below the average value of B_z in the $t_0 + 2$min to $t_0 + 3$min interval as the end of the median DFB. This end point gives a statistical DFB duration of $\sim$ 40s.

In Figure 3.1 I illustrate the 40s duration of each DFB by a shaded region. When a DFB starts before the previous one has ended, I consolidate the overlapping DFBs into a single,

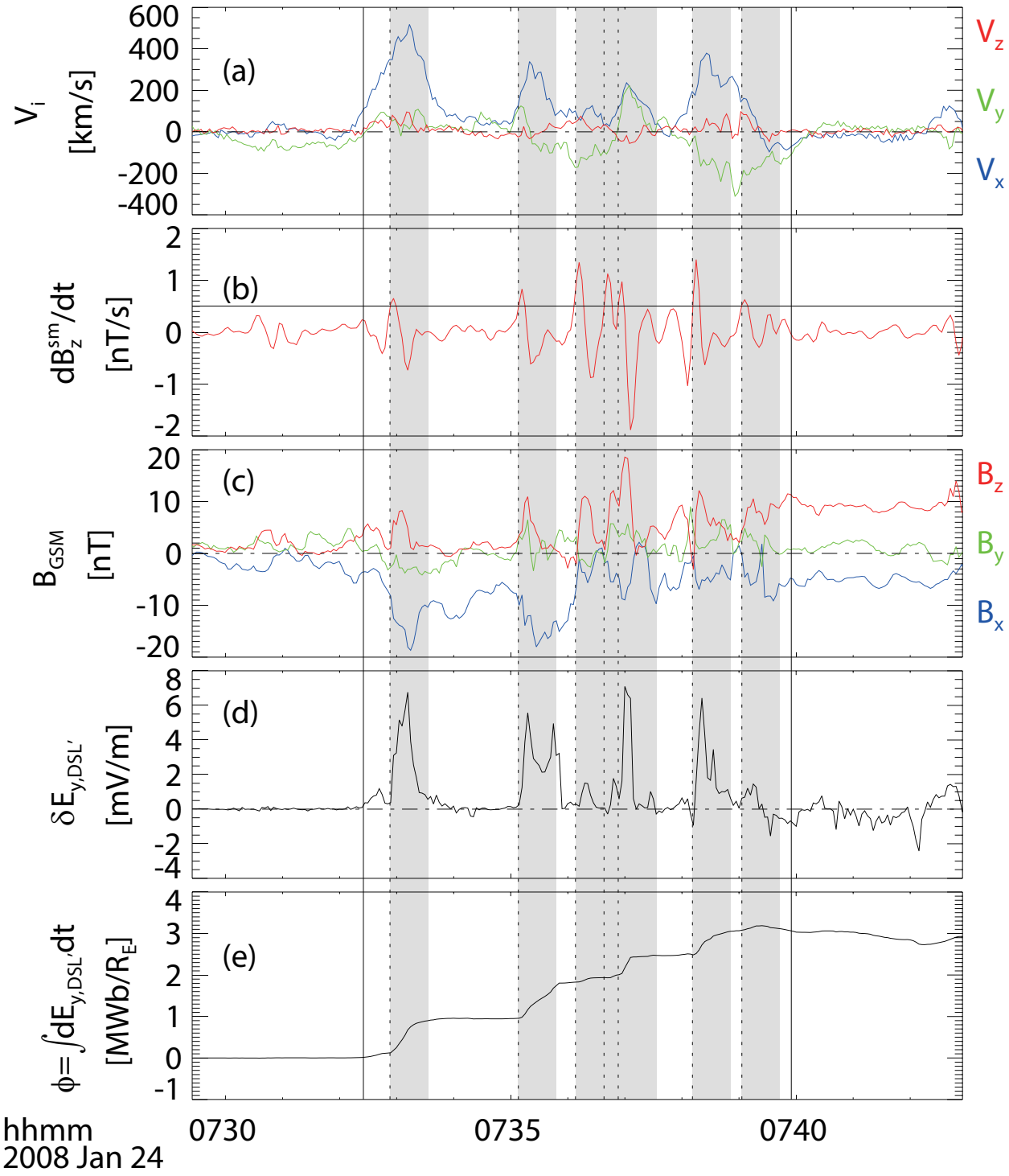
(a)
(b)
(c)
(d)
(e)
V_i [km/s]
dB_z^{sm}/dt [nT/s]
B_{GSM} [nT]
$\delta E_{y,DSL'}$ [mV/m]
$\phi = \int dE_{y,DSL'} dt$ [MWb/R_E]
V_z
V_y
V_x
B_z
B_y
B_x
600
400
200
0
-200
-400
2
1
0
-1
-2
20
10
0
-10
-20
8
6
4
2
0
-2
-4
4
3
2
1
0
-1
hhmm
2008 Jan 24
0730
0735
0740

longer duration (hence the long 3rd duration in Figure 3.1). The DFBs are associated with not only strong magnetic field increases (Figure 3.1c) but also flow bursts (Figure 3.1a). As a result, DFBs are correlated with strong electric field impulses (Figure 3.1d). These associations are also evident in the superposed epoch analysis (Figure 3.2). Due to their strong electric field, the DFBs contribute significant cumulative magnetic flux transport (time-integral of $E_{y,\mathrm{DSL}'}$)—for this event, the DFBs take $< 55\%$ of the BBF duration but contribute $> 90\%$ of the BBF's flux transport (Figure 3.1e).

Next I repeat what I did in Figure 3.1 for each of my 1208 BBFs and display the statistical results in Figure 3.3. Since the identification of DFBs and the amount of flux transport they accomplish depend on the DFB selection criteria, I wish to determine how these and other DFB properties change as the selection criteria vary. In particular I ask if there exists a specific range of thresholds that can be used to reveal their characteristic transport efficiency, such that I can use it to further quantify the DFBs' other properties. As expected (Figure 3.3a), the median number of DFBs identified inside each BBF decreases from 6 to 1 as the identification threshold increases from $dB_z^{sm}/dt = 0.1$ to 0.9 nT/s. For $dB_z^{sm} = 0.5$ nT/s, which was used to build the leading DFB list, there are typically 1-6 DFBs inside each BBF (with a median of 3). For different selection criteria, the averages of B_z, v_x, and $\delta E_{y,\mathrm{DSL}'}$ of the DFBs selected inside each BBF do not change much relative to the same averages for the entire BBF. In particular, only a modest, 50%, increase is observed in the typical DFB efficacy for transport relative to BBF transport (Figure 3.3d), across this wide range of selection criteria. Embedded DFBs have a value of B_z typically ~ 1.4 times that of the BBF's average B_z (Figure 3.3b). Their average flow, v_x is about twice that of the BBF's average (Figure 3.3c), which confirms the expected DFB association with individual flow

Figure 3.1 *(preceding page)*: An example of a bursty bulk flow event (observed by P3) illustrating how I identify dipolarizing flux bundles inside a BBF. From top to bottom are: (a) ion bulk velocity, (b) time derivative of 3-point (9 s) running-averaged B_z, (c) magnetic field, (d) Y_{DSL} component of the electric field measured by the electric field instrument, (e) magnetic flux transport calculated by integrating $E_{y,\mathrm{DSL}'}$. The two solid vertical lines mark the start and end of the BBF. The dashed vertical lines mark DFBs inside the BBF. The DFBs are identified with the criteria $dB_z^{\mathrm{sm}}/dt > 0.5$ nT/s, as illustrated by the solid horizontal line in Figure 3.1b. The shaded regions are the ranges of DFBs.

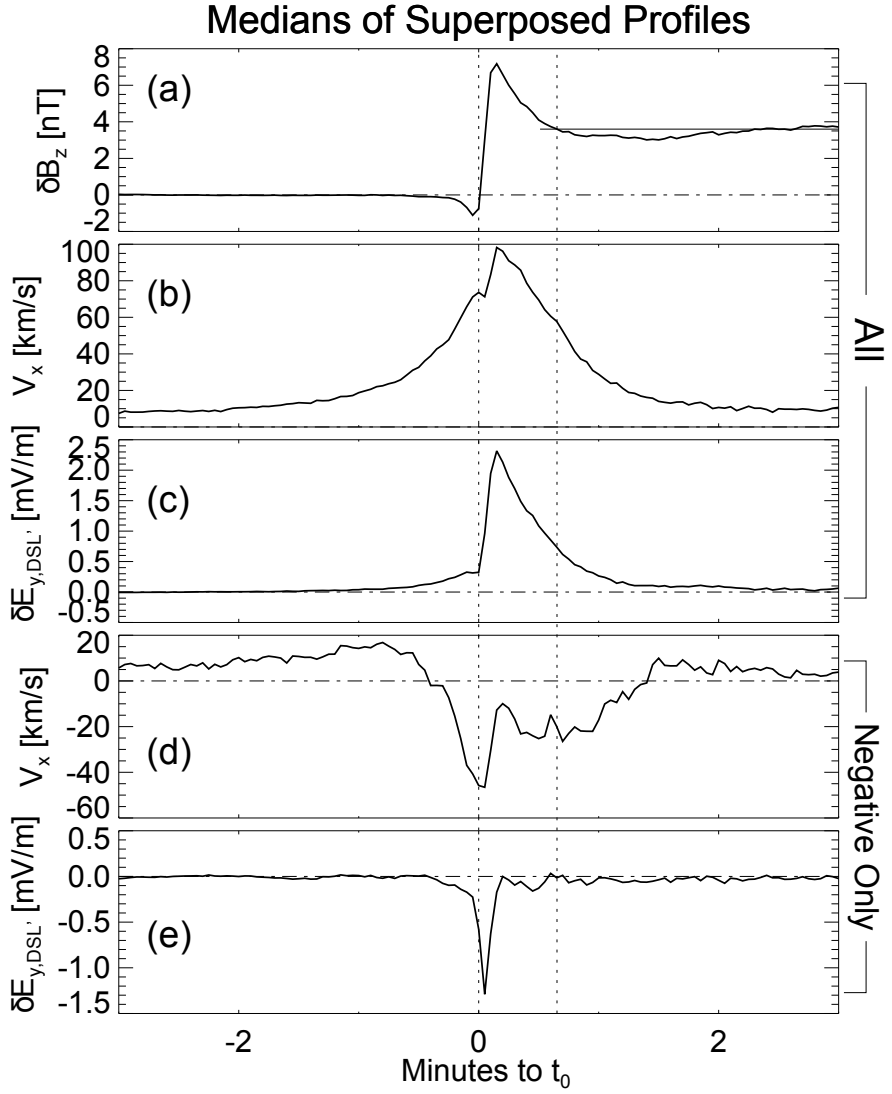

Figure 3.2: Superposed epoch analysis of leading DFBs. The profiles are superposed regarding each DFB's start time t_0. From top to bottom are: (a) B_z with quiet-time average value subtracted, (b and d) X component of ion bulk speed, (c and e) $E_{y,\mathrm{DSL}'}$ with quiet-time average value subtracted. Figures 3.2a-3.2c include both earthward and tailward moving DFBs. Figures 3.2d and 3.2e include only tailward events selected to have a negative peak v_x or $E_{y,\mathrm{DSL}'}$ respectively. (Here the "peak" value of each DFB event is the value that has the maximum absolute value between t_0 and $t_0 + 40$s.) The solid horizontal line in Figure 3.2a represents the average δB_z (of the superposed median profile) from $t_0 + 2$min to $t_0 + 3$min. Where this horizontal line intersects the median profile defines the typical end-time of DFBs.

bursts within the BBF (by Figure 3.2b and previous studies (e.g., *Angelopoulos et al.*, 1992; *Ohtani et al.*, 2004)). The intense magnetic field and correlated high speed flow inside DFBs lead to a high flux transport efficiency: the DFBs' $\delta E_{y,\mathrm{DSL}'}$ is 2-3 times the BBFs' $\delta E_{y,\mathrm{DSL}'}$ for the wide range of selection criteria examined (Fig. 3.3d).

In Figure 3.3e I compare the duration and flux transport of all BBFs and their embedded DFBs. As the DFB selection criteria increase, the number (hence duration) and flux transport of the DFBs decrease, but the flux transport efficiency increases because the more intense ones are being selected. In the range of 0.4-0.6 nT/s criteria, DFBs take only ∼20-40% of the BBF time but contribute ∼60-75% to the transport. I thus maintain 0.5 nT/s as a reasonable selection criterion that epitomizes the efficient role of DFBs for transport (∼30% BBF time but ∼67% transport at this criterion). Dipolarizing flux bundles are the effective agents of BBF flux transport. Even more so than BBFs, DFBs are the major flux transporters in the tail.

3.3.2 Spatial distribution of DFBs and their transport

Since DFBs are significant enough to affect global magnetotail convection, they deserve further study. Here I explore the DFB flux transport characteristics as function of proximity to Earth, cross-tail location, distance from the neutral sheet, and AE index, using the leading DFB list as my statistical dataset. I expect leading DFBs to be representative of the initial stage of DFB propagation, a stage that has fewer complications from the DFB interaction with the Earth's strong dipole or the expanding dipolarization during substorm recovery.

My leading DFB list contains both earthward and tailward moving events. Indeed, the superposed epoch analysis of all leading DFB events in Figures 3.2b and 3.2c exhibits signatures of earthward moving events (positive v_x and E_y), showing that the DFB list is dominated by earthward events. However, as shown in Figures 3.2d and 3.2e, tailward events also exist (few, ∼15% of the database) and they have weaker and more transient flow and electric field than earthward ones. The latter suggests that tailward events are (at least in part) rebounding DFBs. In the following I mostly focus on earthward moving

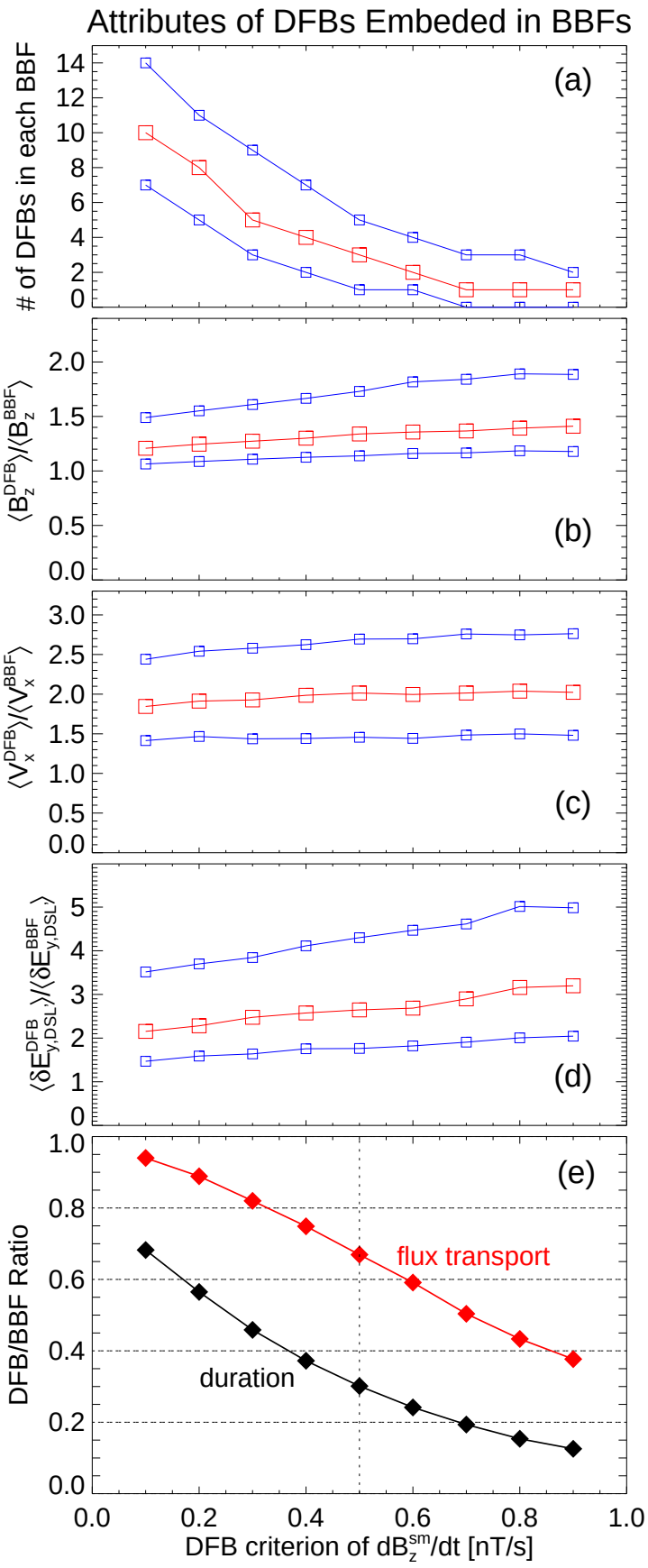
Attributes of DFBs Embeded in BBFs
# of DFBs in each BBF
(a)
$\langle B_z^{DFB}\rangle/\langle B_z^{BBF}\rangle$
(b)
$\langle V_x^{DFB}\rangle/\langle V_x^{BBF}\rangle$
(c)
$\langle \delta E_{y,DSL}^{DFB}\rangle/\langle \delta E_{y,DSL}^{BBF}\rangle$
(d)
DFB/BBF Ratio
(e)
flux transport
duration
DFB criterion of dB_z^{sm}/dt [nT/s]

DFBs, in particular in superposed epoch analyses, defined by positive v_x, E_y, or integral flux transport, to avoid earthward and tailward DFB profiles cancelling each other in my database. Occasionally I segregate and investigate tailward DFB for comparison, but they are not considered a main aspect of this study.

3.3.2.1 X dependence of DFB flux transport (Figures 3.4 and 3.5

Due to the THEMIS orbit to-date, $X < -12$ R_E DFB events are available only from 2008-2009 THEMIS tail seasons, but $X > -12$ R_E events are available from all four tail seasons in my study (2008-2011). However, 2008-2009 are solar minimum years, while 2010-2011 are during the rising phase of the solar cycle. To avoid bias from different solar cycle conditions, in Figures 3.4 and 3.5 I only use the 2008-2009 events of the leading DFB list.

In Figures 3.4a-3.4c I plot the dependence of the DFBs' peak δB_z (detrended), v_x, and $\delta E_{y,\mathrm{DSL}'}$ on downtail distance X. I use peak values (the value having maximum absolute value) of these quantities from t_0 to $t_0 + 40$s. Note that 40s is a typical duration of DFBs and that the peak value is not affected by the uncertainty in that duration.

In Figure 3.4a I subtracted from B_z the average value of $t_0 - 3$min to $t_0 - 2$min for each event, in order to reduce the contribution from the large-scale B_z variation in the magnetotail and the past state of the magnetosphere. Figure 3.4a shows that when one moves earthward from the reconnection site the DFB's δB_z decreases and reaches a minimum at $X{=}\sim -14$ R_E; then it increases as one moves further earthward reaching values larger than near the reconnection site.

Figure 3.3 *(preceding page)*: Comparison of bursty bulk flows and their embedded dipolarizing flux bundles defined using nine selection criteria. Medians and quartiles are shown as red and blue squares, respectively. Figure 3.3a shows the number of DFBs inside each BBF. Figures 3.3b-3.3d show medians and quartiles of the ratio of two averages of quantities specified in the figure labels. The numerator of the ratio corresponds to the time range of the BBF-embedded DFBs; the denominator corresponds to the entire BBF range. In Figure 3.3e, I calculate the total duration and flux transport of all my BBFs and their embedded DFBs, and then compute the ratio between total embedded DFB duration/transport and total BBF duration/transport as solid diamonds.

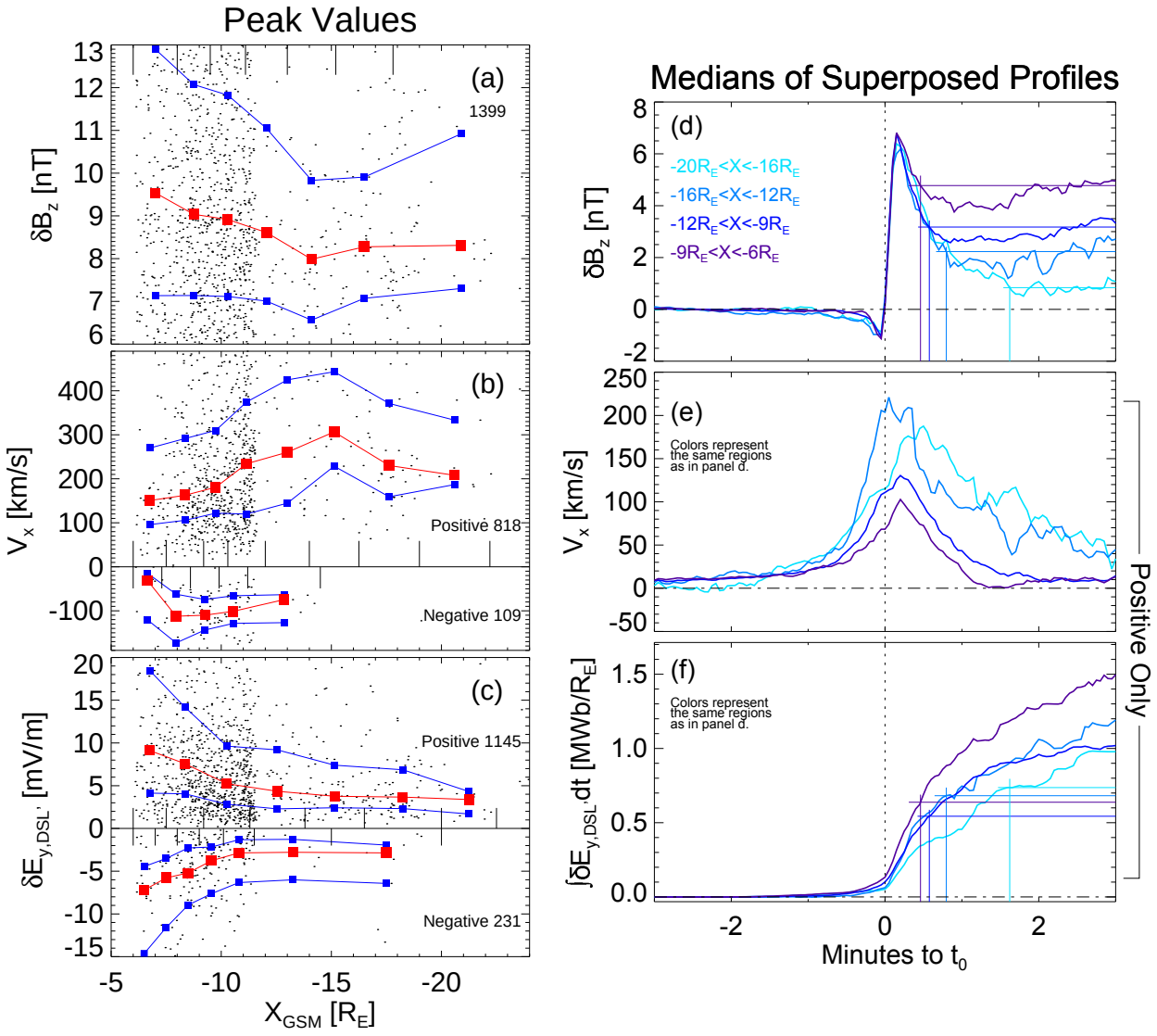
Peak Values
(a)
1399
δB_z [nT]
(b)
Positive 818
Negative 109
V_x [km/s]
(c)
Positive 1145
Negative 231
δE_y,DSL [mV/m]
X_GSM [R_E]
Medians of Superposed Profiles
(d)
-20R_E<X<-16R_E
-16R_E<X<-12R_E
-12R_E<X<-9R_E
-9R_E<X<-6R_E
δB_z [nT]
(e)
Colors represent the same regions as in panel d.
V_x [km/s]
(f)
Colors represent the same regions as in panel d.
∫δE_y,DSL dt [MWb/R_E]
Minutes to t_0
Positive Only

Figure 3.4b shows that the earthward DFBs' velocity increases as one moves away from the reconnection site towards Earth; it maximizes at $X =\sim -15$ R_E and then starts to decrease further earthward. This suggests that DFBs start to decelerate at $X =\sim -15$ R_E. After their deceleration some DFBs may rebound tailward at the inner edge of the plasma sheet; the lower part (negative v_x) of Figure 3.4b displays these tailward events. The DFBs' tailward velocity increases initially after the rebounding, reaches maximum at $X =\sim -10$, and then decreases. Such velocity variations are consistent with the overshoot-rebound picture (e.g., *Chen and Wolf*, 1999). I also note that along the Sun-Earth line tailward DFBs always travel slower (have smaller median peak $|v_x|$) than earthward DFBs.

Figure 3.4c shows the distribution of the DFBs' peak $\delta E_{y,\mathrm{DSL}'}$ (flux transport rate). The peak $\delta E_{y,\mathrm{DSL}'}$ profile demonstrates that for both earthward and tailward transporting DFBs (given by positive or negative peak flux transport rates respectively), their flux transport rate is higher when they are observed closer to Earth. Earthward transporting DFBs are

---

Figure 3.4 *(preceding page)*: Dependence of leading DFB properties on downtail distance, X. Figures 3.4a-3.4c show the distributions of peak (the value having maximum absolute value between t_0 and $t_0 + 40$s) detrended B_z (a); X component of ion bulk flow (b); and $E_{y,\mathrm{DSL}'}$ (c). Each dot represents a single event. Only those events with high-resolution plasma data were included in Figure 3.4b, fewer than in other figures. I only bin the region earthward of the near-earth reconnection site ($X =\sim -20$ R_E) because tailward of it there are too few events. The red (blue) squares are medians (quartiles) in the X bins. Each bin's boundaries are represented by thin vertical bars. In Figures 3.4b and 3.4c I bin the events with positive peak value and those with negative peak value separately. Figures 3.4d-4f show the superposed epoch analysis of (d) detrended B_z; (e) X component of ion bulk flow; and (f) time-integrated $E_{y,\mathrm{DSL}'}$ starting from t_0-3min. Results are color-coded by event downtail distance (see insert in Figure 3.4d). Figure 3.4e includes only events with positive peak v_x; Figure 3.4f includes events with positive time-integrated $E_{y,\mathrm{DSL}'}$ from t_0 to $t_0 + 2$min. For each downtail distance range (color), the horizontal line in Figure 3.4d represents the quasi-steady dipolarization state achieved after DFB passage; it is determined from the average δB_z of the superposed epoch profile from $t_0 + 2$min to $t_0 + 3$min. The vertical line marks the first time when the δB_z profile intersects this horizontal line; it defines the end-point for typical DFBs in each distance range, and determines the typical DFB duration in that range. In Figure 3.4f, the vertical lines are carried over from Figure 3.4d. The horizontal lines are defined by the intersections of the cumulative flux transport curves with the vertical lines. Each horizontal line denotes the cumulative flux transport by a typical-duration DFB in each downtail distance range (color).

much more frequently observed than tailward transporting ones (83% vs 17%). At the same location, the transport rate of Earthward transporting DFBs is higher than that of tailward ones, which is most likely due to the faster speed of earthward DFBs.

The X-dependence of the DFB flux transport rate is opposite to that of fast flows which show an E_y decrease with proximity to Earth (*Hsu et al.*, 2012). This contradiction may be cause by different event selection criteria, the choice of epoch zero for the superposed epoch analysis by *Hsu et al.* (2012), and their inclusion of both earthward and tailward flows when superposing the data (tailward flows near earth drags down the superposed median electric field).

Since a DFB travels along the tail coherently (*Runov et al.*, 2009), it is expected to transport the same amount of flux along its way. Therefore, the enhancement of flux transport rate closer to Earth may be caused by the reduction of DFB duration. To examine whether the DFB duration decreases with smaller distance to Earth, I apply the DFB-duration determination technique of Figure 3.2a to the (leading) DFBs at four downtail regions, as shown in the superposed epoch analysis of Figure 3.4d (due to the small number of events in each region, to get cleaner profiles I have applied a 3-point running average to the data before superposing them; I did the same to all superposed epoch analysis of events in split groups, in the following). Figure 3.4d shows that the duration of the leading DFBs is shorter closer to Earth. As the DFB velocity does not increase towards Earth within 15 R_E downtail, the reduction of DFB duration is due to the squeezing of DFBs in their lines of motion, at least for $X > -15$ R_E.

I note that although the DFB duration changes, my use of a 40s duration to determine the peak quantity value is still valid: as illustrated by Figures 3.4d and 3.4e, the peak δB_z and v_x (and also $\delta E_{y,\mathrm{DSL}'}$, not shown) at the four downtail regions are all within 40s after t_0. The summits of the superposed δB_z median profiles in Figures 3.4d first decrease, then increase as one moves closer to Earth, confirming the trend in Figure 3.4a. The summits of the median v_x first increase then decrease (Figure 3.4e), confirming the trend of earthward events in Figure 3.4b.

I also note (Figure 3.4d) that as one moves closer to Earth the B_z level after the passage of leading DFBs relative to that ahead of leading DFBs increases. At 16-20 R_E downtail, the post-DFB B_z returns to almost its pre-DFB value, while at 6-9 R_E downtail, the post-DFB B_z is larger than the pre-DFB B_z by $\sim$70% of the B_z jump at the dipolarization front. This means that leading DFBs correspond to transient dipolarizations further away from Earth but bring about more permanent dipolarizations close to Earth. This is consistent with the pileup model of the substorm current wedge, whereby the DFBs stop and pile up the newly reconnected flux against the dipole-like region (e.g., *Zhang et al.*, 2007). In other words, the observed increase in δB_z relative to the pre-DFB level is interpreted here as due to the tailward expansion of the broad dipolarization. It is consistent with the interpretation of the DFBs and their associated flow bursts as identical to observations of current disruption (*Angelopoulos et al.*, 1999) which is also known to expand tailward.

In Figure 3.4f I superpose the cumulative flux transport of the DFBs in different downtail regions (for earthward transport only). The cumulative flux transport takes into account both the increasing flux transport rate and the decreasing DFB duration toward Earth. The sharp flux transport increase immediately after t_0 is contributed by the leading DFB; the ensuing, slower increase is accomplished by DFBs that follow behind the leading one. (Follow-on DFBs result in a broad, not a sharp, increase in flux transport because they are not arriving with the same time-delay relative to the leading DFB, so their epochs are not coincident with each other.) The cumulative flux transport from both leading and follow-on DFBs plateaus by t_0+3min to approximately the same level in the three outer regions beyond $X = -9$ R_E. In the region inside $X = -9$ R_E, however, the cumulative flux transport at $t_0 + 3$min is 50% higher than outside that region and that difference continues to increase at that time. This is either due to more flux transport by each DFB (leading or follow-on), or due to the pileup of more follow-on DFBs after the leading one Earthward of $X = -9$ R_E, than tailward of $X = -9$ R_E.

The net flux transport typical of leading DFBs in each of the four regions can be estimated by considering the cumulative transport at the end of the typical leading DFB durations, the latter denoted by the vertical lines in Figure 3.4d. Transferring those vertical lines in

Figure 3.4f I see that the highest net flux transport (cyan horizontal line, -20 R_E¡X¡-16 R_E) is only ∼30% more than the lowest (dark blue line, -12 $R_E < X < -9$ R_E) and only 15% more than the innermost range (purple line, -9 $R_E < X < -6$ R_E). These differences in net transport by leading DFBs are likely not significant. The approximate constancy in net flux transport amongst leading DFBs in the four spatial regions is thus due to the reduction in DFB duration with proximity to Earth, even when their flux transport rate increases.

I therefore favor the second possibility, more follow-on DFBs, to explain the increased net transport closer to Earth. More follow-on DFBs are likely the result of azimuthal expansion of the large-scale permanent dipolarization region that exhibits only a limited radial expansion in sectors adjacent to the activation meridian (*Angelopoulos et al.*, 1996, Figure 3.17). A spacecraft near Earth is likely to experience more follow-on DFBs due to azimuthal expansion of the dipolarized magnetosphere. Such DFBs, located at the edges of the permanent dipolarization and collocated with fast flows, expand also azimuthally and are likely visible near-Earth more often than further away, given the localized nature of mid-tail flows and the well-documented extended nature of near-Earth dipolarization (e.g., *Nagai*, 1982).

To quantify the net flux transport shown in Figure 3.4f, and determine its dependence on downtail distance I construct Figure 3.5, by first interpolating the DFB durations in the four regions from Figure 3.4d onto the location of each leading DFB's location to determine its nominal anticipated duration. I next determine each DFB's average $\delta E_{y,\mathrm{DSL}'}$ during each event's duration. Figure 3.5a shows the transport rate averages of DFBs as function of distance. For both earthward and tailward DFBs, the typical average $\delta E_{y,\mathrm{DSL}'}$ is larger when the DFB is observed closer to Earth, consistent with the peak $\delta E_{y,\mathrm{DSL}'}$ trends in Figure 3.4c. Multiplying the average $\delta E_{y,\mathrm{DSL}'}$ of each event with its nominal (X-dependent) duration gives the flux transport of leading DFBs. This is shown in Figure 3.5b. For both earthward and tailward DFBs, the DFB flux transport is higher in the nearest and farthest bins from Earth than that in the middle bins, which is likely due to the rough determination of DFB durations. However, the amounts of magnetic flux transported by earthward DFBs at different downtail regions are approximately the same (there is only a small variation of ±15% with distance), consistent with Figure 3.4f.

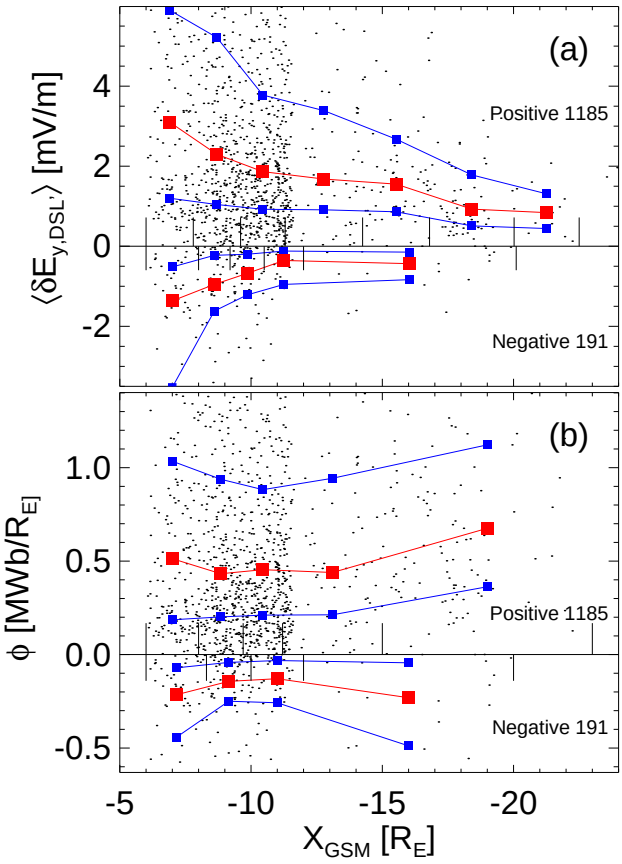

Figure 3.5: The X-dependence of (a) average. $E_{y,\mathrm{DSL}'}$; and (b) flux transport of dipolarizing flux bundles. The results are based on the leading DFB list and are organized in the same way as those in Figure 3.4: I first infer each DFB's duration by linearly interpolating the typical durations in Figure 3.4d (see Section 3.3.2.1 for details), and then use these durations to compute each DFB's average $E_{y,\mathrm{DSL}'}$ (Figure 3.5a) and flux transport ϕ (Figure 3.5b).

3.3.2.2 Y dependence of DFB flux transport

In Figure 3.6 I examine the leading DFB flux transport properties as function of cross-tail location, Y. The dots in Figures 3.6a-3.6c reveal that more leading DFBs appear in the dusk sector of the tail ($Y > 0$); this is also consistent with past reports of a higher occurrence rate of leading DFBs there (see Figure 2.1c). Figure 3.6a shows that the DFBs' peak δB_z maximizes at the pre-midnight sector of the tail ($Y = 0 - 5$ R_E). Figures 3.6b and 3.6c show that the peak v_x and $\delta E_{y,\mathrm{DSL}'}$ in the dusk sector are larger than those in the dawn sector of the tail ($Y < 0$). Except the unclear v_x trend for tailward DFBs (lower part of Figure 3.6b), such clear dawn-dusk asymmetry is obvious for both earthward and tailward events.

In Figures 3.6d and 3.6e I repeat for dusk and dawn sector events what I did in Figures 3.4d and 3.4f. The events in the dusk sector transport more flux than those in the dawn sector within a given time (Figure 3.6e). However, as the DFB duration in the dusk sector is shorter than that in the dawn sector (indicated by the vertical colored lines in Figure 3.6d), the dusk-sector DFBs transport approximately the same amount of net flux as the dawn-sector DFB (indicated by the horizontal colored lines in Figure 3.6d). The shorter DFB duration in the dusk sector is most likely caused by the fast DFB velocity there (Figure 3.6b). Therefore, there is little dawn-dusk asymmetry in the amount of flux transport done by each individual DFB; DFBs in the dusk sector has higher flux transport rate (Figure 3.6b) and transport more flux within a fixed time (Figure 3.6e) because the DFBs (leading and following ones) travel faster there.

3.3.2.3 DFB flux transport dependence on distance from the neutral sheet

Next I investigate the variation of DFB flux transport on distance from the neutral sheet (represented by $B_{\mathrm{q}x}/B_{\mathrm{lobe,q}}$, see Section 2.2.1) in Figure 3.7. Figure 3.7a shows that for both earthward and tailward moving DFBs (given by positive and negative transport respectively), the typical flux transport rate (represented by the peak $\delta E_{y,\mathrm{DSL}'}$) increases with increasing distance from the neutral sheet. In Figure 3.7b I superpose the cumulative flux transport for events at different distances from the neutral sheet (including only positive-transport

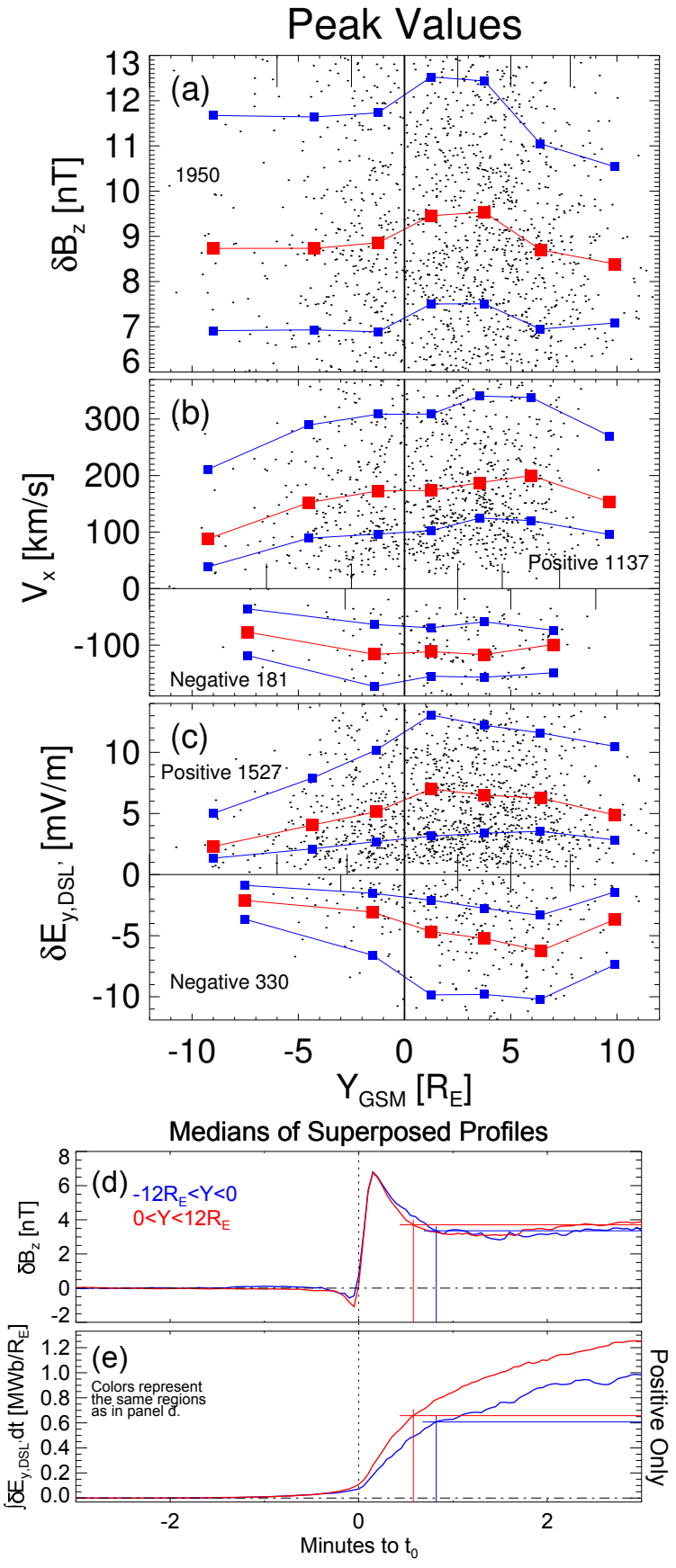
Peak Values
(a)
1950
δB_z [nT]
(b)
Positive 1137
Negative 181
V_x [km/s]
(c)
Positive 1527
Negative 330
δE_y,DSL' [mV/m]
Y_GSM [R_E]
Medians of Superposed Profiles
(d)
-12R_E<Y<0
0<Y<12R_E
δB_z [nT]
(e)
Colors represent the same regions as in panel d.
∫δE_y,DSL'dt [MWb/R_E]
Positive Only
Minutes to t_0

events). The superposed medians show that within a fixed amount of time leading DFBs perform also increasingly more net flux transport with increasing distance from the neutral sheet. Dipolarizing flux bundle durations at the four distances are approximately the same in the four distance regions (not shown). Therefore, with increasing distance from the neutral sheet leading DFBs also transport increasingly more net flux.

This result is counter-intuitive because I expect a DFB, defined by its flux tube, to transport the same amount of magnetic flux at different distances from the neutral sheet if it moves like a hard body along X. Indeed, under most conditions E_y is mainly contributed by the transport in X—on average my events have a $v_x B_z$ term that is five times the $-v_z B_x$ term. However, far from the neutral sheet the hard body picture may no longer be appropriate; the transport by $-v_z B_x$ may be important due to finite Vz and strong Bx. To examine whether the variation of DFB flux transport with distance from the neutral sheet is contributed by the flux transport along X or Z, I superpose the $v_x B_z$ and $-v_z B_x$ terms in Figures 3.7c-3.7e from plasma measurements. Here I only show positive transports; negative transports share the same trends.

Figure 3.7c shows the flux transport calculated as the integration of $E_{y,\mathrm{plasma}} = v_x B_z - v_z B_x$, where v_x and v_z are from plasma (ion) measurements. Although the transport values in Figure 3.7c are smaller than those from electric field measurements in Figure 3.7b (due to break-down of frozen-in condition), the increase of flux transport with distance from the neutral sheet is consistent with the increase in Figure 3.7b. Therefore, using plasma measurements to analyze the cause of this increase is applicable.

The flux transport along X (integration of $v_x B_z$, Figure 3.7d) increases only slightly when one moves away from the neutral sheet. Two effects related to the shape of the DFB may

---

Figure 3.6 *(preceding page)*: Dependence of dipolarizing flux bundle properties on cross-tail location Y (given by the average satellite position from $t_0 - 1.5$min to $t_0 + 1.5$min). The results are based on the leading DFB list and are organized in the same way as those in Figure 3.4. Figures 3.6a-3.6c show the distributions of peak values. In the superposed analysis of Figures 3.4d and 3.4e events are separated regarding their cross-tail location as indicated by the colors in Figure 3.4d. Figure 3.4e is from only the events that have a positive time-integrated $E_{y,\mathrm{DSL}'}$ from t_0 to $t_0 + 2$min.

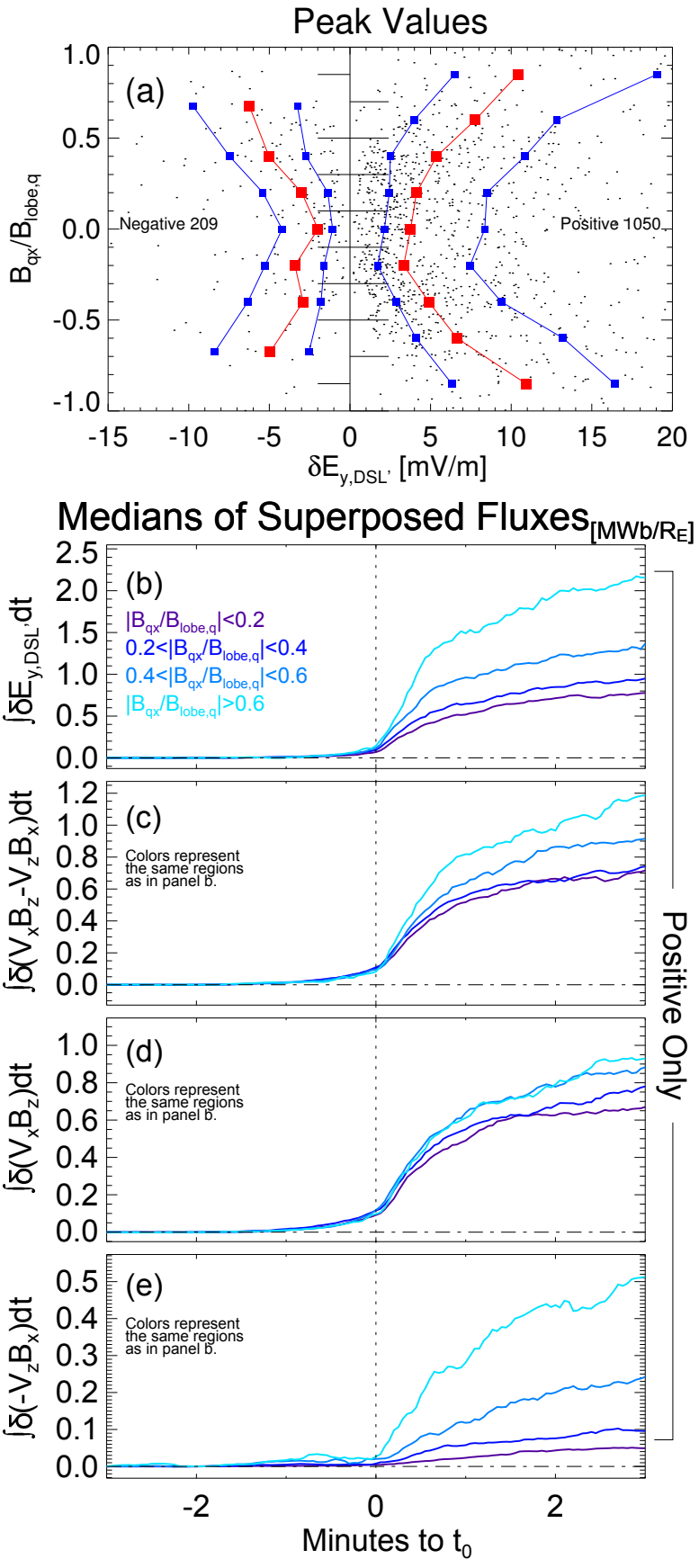
Peak Values
(a)
Negative 209
Positive 1050
$B_{qx}/B_{lobe,q}$
$\delta E_{y,DSL}$, [mV/m]
Medians of Superposed Fluxes[MWb/R_E]
(b)
$|B_{qx}/B_{lobe,q}|<0.2$
$0.2<|B_{qx}/B_{lobe,q}|<0.4$
$0.4<|B_{qx}/B_{lobe,q}|<0.6$
$|B_{qx}/B_{lobe,q}|>0.6$
$\int\delta E_{y,DSL}dt$
(c)
Colors represent the same regions as in panel b.
$\int\delta(V_xB_z-V_zB_x)dt$
(d)
Colors represent the same regions as in panel b.
$\int\delta(V_xB_z)dt$
(e)
Colors represent the same regions as in panel b.
$\int\delta(-V_zB_x)dt$
Positive Only
Minutes to t_0

lead to this increase, as illustrated in Figure 3.8. The shape of a DFB is similar to that of an ordinary flux tube, or bundle (*Chen and Wolf*, 1993, Section 2.3) in the 9-12 R_E downtail region. Figure 3.8a shows the XZ-view of such shape—the DFB transect along X is shorter far from the neutral sheet even though the bundle contains the same amount of flux. As a result, the flux transport rate along X should be higher farther away from the neutral sheet. Figure 3.8b illustrates the XY view of the DFB—it is also narrower in Y farther away from the neutral sheet while containing the same amount of flux. As a result, this flux tube flaring increases both the earthward transport rate ($v_x B_z$) and the total amount of observed transport per unit Y-length (the integral of $v_x B_z$) with distance from the neutral sheet.

On the other hand, the DFB B_x flux transport along Z (integral of $-v_z B_x$, Figure 3.7e) increases a lot when it is observed farther away from the neutral sheet. The integrated Z-transport at $|B_{qx}/B_{lobe,q}| > 0.6$ is ~ 10 times more than that at $|B_{qx}/B_{lobe,q}| < 0.2$. The increase of DFB flux transport farther away from the neutral sheet (Figure 3.7c) is mainly contributed by the flux transport along Z. For positive (negative) transport events, this Z-transport corresponds to a contraction (expansion) of DFB field lines in Z. The leading DFB list contains more contraction events than expansion events. I conclude that during its dipolarizing motion the dipolarizing flux bundle also contracts, leading to significant increases in equatorward transport with increasing distance from the neutral sheet.

Figure 3.7 *(preceding page)*: The dependence of dipolarizing flux bundle flux transport on the proxy distance from the neutral sheet. The results are based on the leading DFB list and are organized in the same way as those in Figure 3.4. Figure 3.7a shows the distributions of peak $\delta E_{y,DSL'}$. Bin boundaries are represented by horizontal thin bars. $E_{y,DSL'}$ in Figures 3.7a and 3.7b is from the electric field instrument. In Figures 3.7c-3.7e v is the ion bulk velocity. In Figures 3.7b-3.7e the results are from only events with a positive time-integrated quantity from t_0 to $t_0 + 2$min. The events are separated according to their distance from the neutral sheet. Different regions are represented by different colors (see Figure 3.7b).

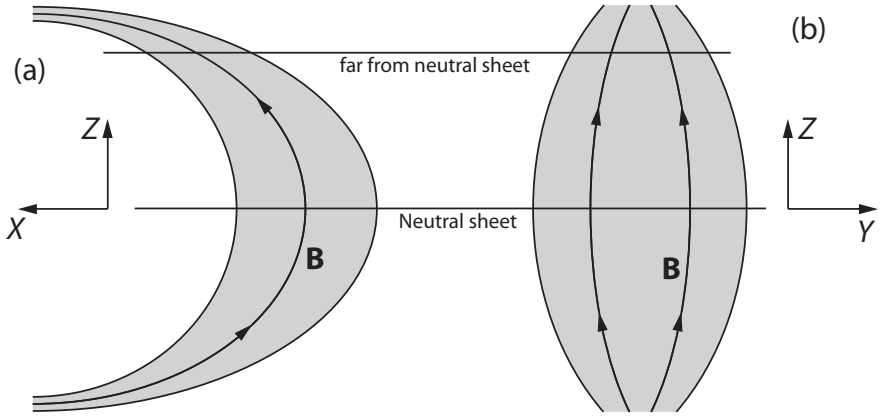

Figure 3.8: Illustrations of a dipolarizing flux bundle viewed in (a) XZ and (b) YZ planes.

3.3.2.4 DFB flux transport dependence on AE index

The flux transport of dipolarizing flux bundles is one of the most important observables during substorms and has been used as a tool of substorm timing (e.g., *Angelopoulos et al.*, 2009; *Liu et al.*, 2009, 2011a,b). Since substorms are associated with a considerable and rapid release of energy stored in the lobes, I expect DFBs to transport more magnetic energy, and thus magnetic flux during high AE activity intervals compared to non-substorm, low AE times.

In Figure 3.9 I investigate the variation of DFB flux transport with geomagnetic activity level, as represented by AE index. During substorms the ground magnetic perturbations usually commence after the DFB appearance in the tail (*Angelopoulos et al.*, 2008b; *Nishimura et al.*, 2012), so I compute each DFB's corresponding AE value as the average AE over that DFB's interval: $t_0 + 1.5$min to $t_0 + 4.5$min. As expected from the causal relationship of tail activations and ground intensifications, the magnetic field perturbation of DFBs during higher AE values is more intense (Figure 3.9a). This is expected because the DFB current system is proportional to this perturbation, and I know that DFBs are likely wedgelets (e.g., *Rostoker*, 1991, ; Chapter 5) that contribute, in part or as a whole, to the substorm current that is the major contributor to AE during substorms. This is the first documented association between DFB intensity and AE activity, that provides additional confirmation to the controlling role of DFBs and associated flow bursts to the AE index.

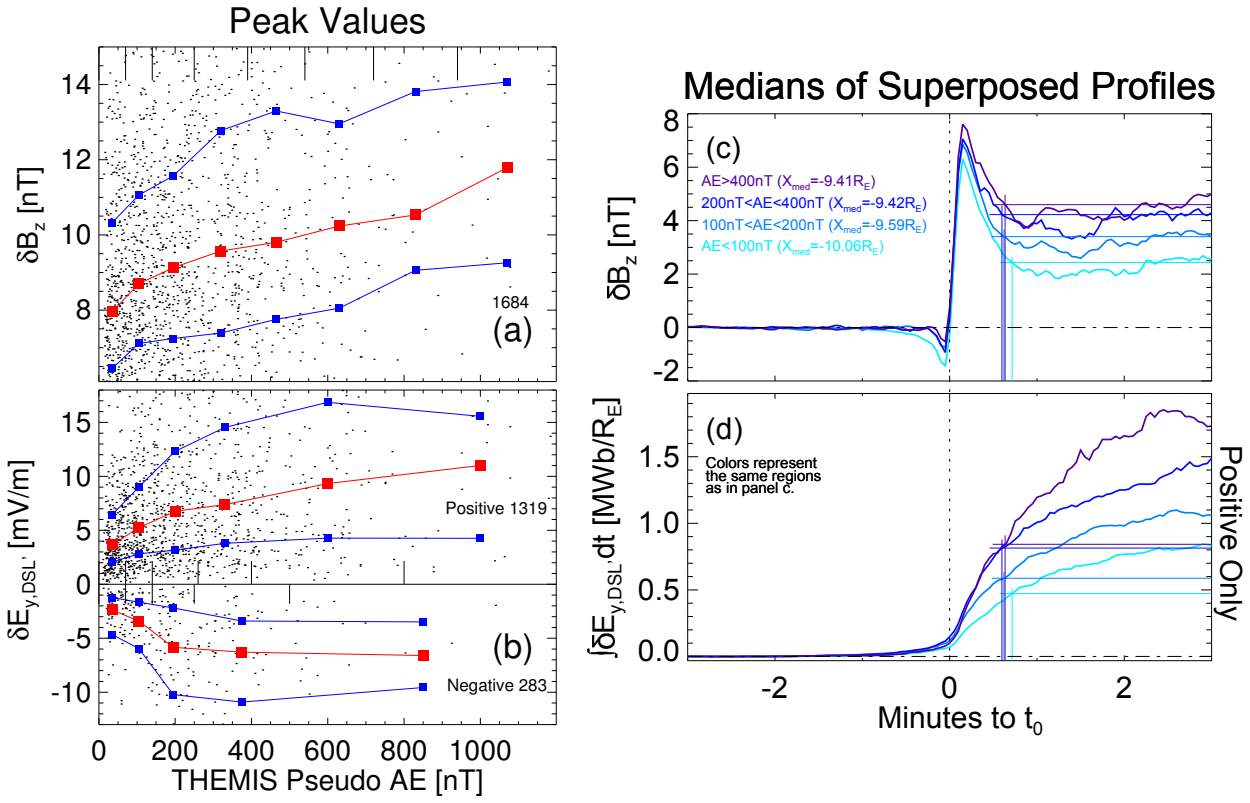

Figure 3.9: Dependence of dipolarizing flux bundle properties on geomagnetic activity as determined by the THEMIS pseudo AE index. The results come from the leading DFBs observed during 0-14UT when the THEMIS AE is available. The plots are organized in the same way as those of Figure 3.4,. The AE index is the average value over each event's $t_0 + 1.5$min to $t_0 + 4.5$min. In Figures 3.9a and 3.9b δB_z and $\delta E_{y,\mathrm{DSL}'}$ are peak values. In Figures 3.9c and 3.9d events are separated according to their AE index; the results for events at different regions are represented by different colors (see Figure 3.9c). In Figure 3.9d the results are from only the events that have a positive time-integration from t_0 to $t_0 + 2$min.

Based on the previous discussion, it is not unexpected to find (Figure 3.9b) that DFBs have also generally a higher flux transport rate during higher substorm activity since. However, I see that the transport rate is not proportional to AE, but plateaus at a maximum level of about 10 mV/m (for positive transport) and approximately half that, -6 mV/m for tailward transport for high AE (AE$>$ 400nT).

Examination of DFB durations during different AE values shows that they are approximately the same (Figure 3.9c), $\sim$40sec. Because of the approximate constancy of in their duration but increasing peak flux transport rate (Figure 3.9b) with AE up to a point of saturation, individual DFBs transport more net flux (Figure 3.9d) during higher substorm activity—the net flux transport by an individual DFB during AE$>$ 400 nT (purple horizontal line in Figure 3.9d) is nearly twice that during AE$<$ 100 nT (cyan horizontal line in Figure 3.9d). However it is only a few percent ($\sim$5%) higher than that for the level 200nT$<$AE$<$ 400nT (the dark blue line).

Another point I note in Figure 3.9c is that the level of δB_z several minutes after the DFB passage is finite, and in fact increases with higher substorm activity. The level of semi-permanent δB_z increase depends also on downtail distance as I have seen in Figure 3.4d. Since my database is dominated by events at -9 R$_E$ $< X <$ -12 R$_E$ I take that to be the range for which my results apply quantitatively, and assume only qualitative applicability for other distances. The increase of the semi-permanent dipolarization level with increasing AE (at a given distance, in my database -9 R$_E$ $< X <$ -12 R$_E$), indicates that during higher substorm activity the pile-up of the DFBs is more severe. In other words, the B_z changes (from stretched to dipolar configuration) brought about by the DFBs is more intense for high AE. Additionally, the level of semi-permanent dipolarization (δB_z increase) saturates too (like the flux transport and flux transport rate), as evident in the fact that the dark blue and purple horizontal lines in Figure 3.9c (corresponding to the δB_z increases for the highest two AE groups) are within $<$ 0.25nT of each other, yet they are both about a factor of 2 greater than the cyan line (corresponding to the δB_z increase for the AE lowest level). Apparently, at a given distance there exists a maximum achievable level of stretching-to-recovery changes; further ground response (AE intensification) is not caused by inward

penetration of more dipolarization fronts. This is understandable since local dipolarization reduces local flux tube volume content per unit flux unit, and renders the local plasma sheet more impenetrable to incoming low entropy flow bursts. Further AE increases are then due to other effects, possibly further accumulation of dipolarization fronts at larger distances or local times.

The enhancements of δB_z, flux transport rate and DFB pileup with increasing AE are similar to their enhancements with proximity to Earth (Section 3.3.2.1. Suspicion thus arises that the results in Figure 3.9 are actually influenced by the DFBs' X-dependence, because DFBs may penetrate closer to Earth during higher substorm activity. To clear away this point, I recorded, in Figure 3.9c, the median X value of the DFBs observed in each AE range. These averages indicate that the DFBs penetrate inward by only a little deeper ($\sim$0.65 R_E) during higher substorm activity. Additionally, I have repeated the analysis using only DFBs from the same region, $-9\ R_E < X < -10\ R_E$, and found that my results hold for this fixed downtail distance. Thus, the trends in Figure 3.9 are due not to inward penetration of DFBs but reflect true dependence on the value of AE.

In Figure 3.10 I examine the dependence of (leading) DFB occurrence rate on substorm activity, as well as downtail location. At all downtail locations, leading DFBs appear more often during higher substorm activity. At each AE level, the DFBs' occurrence rate peak at $X = -10$ to $-12\ R_E$. This is the location where the DFBs get diverted east or west before they finally stop (e.g., *Kissinger et al.*, 2012), so they linger there longer and have a greater chance to be observed.

In Figure 3.10b I investigate the occurrence rate of DFB samples in each downtail location and AE range. This approach folds into the occurrence rate the DFB durations, as determined by interpolation of typical duration values from Figure 3.4d at each DFB position. The resultant trend is thus a combination of the increasing DFB duration with downtail distance and the DFB occurrence rate trend of Figure 3.10a. Similar to the trends in Figure 3.10a, DFBs are more likely to be observed during higher AE. On the other hand, the occurrence rate of DFB samples as function of downtail distance is dominated by DFB durations: it is increasingly more likely to observe a DFB further from Earth at all AE levels.

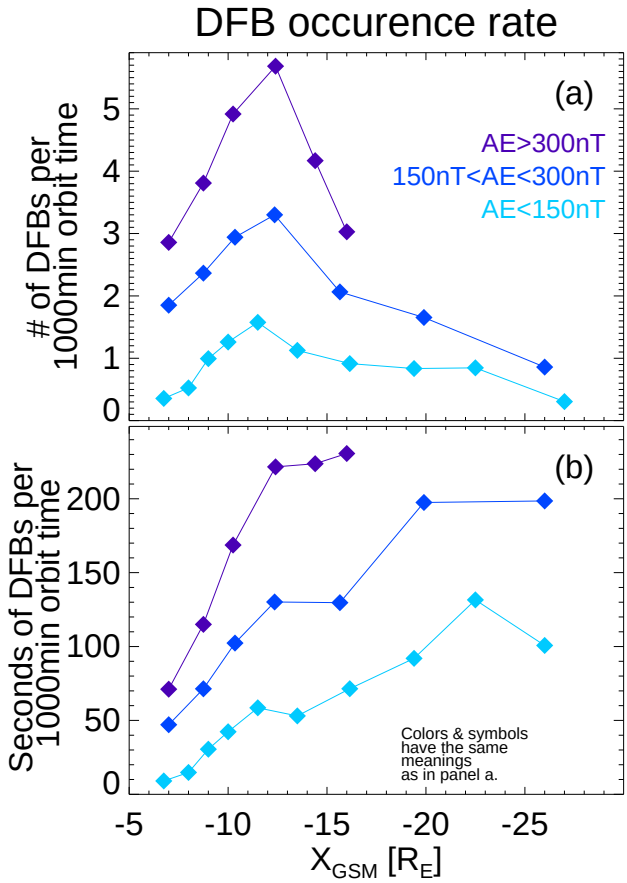

Figure 3.10: Occurrence rate of dipolarizing flux bundles depending on AE (average AE over each event's $t_0 + 1.5$min to $t_0 + 4.5$min) and downtail location. The results come from the leading DFBs observed during 2008-09 (to avoid solar cycle interference on X-dependence) and 0-14UT (when THEMIS AE is available). Furthermore, I include only DFBs with positive peak $E_{y,\mathrm{DSL}'}$ within t_0 to $t_0 + 40$s. I bin the THEMIS orbit in the range of $\sqrt{Y^2 + Z^2} < 12$ $\mathrm{R_E}$ under different AE conditions. Figure 3.10a shows the number of observed DFBs per 1000 minutes of THEMIS orbit time when its probes fall into a particular X bin and AE was in a particular range (the occurrence rate of DFB events). Figure 3.10b shows the total duration of all the DFBs in each X bin and AE range normalized by THEMIS orbit time in that X bin and AE range (the occurrence rate of DFB samples). The total duration is obtained by adding each DFB's duration; each DFB's duration is interpolated from the typical durations in Figure 3.4d.

3.4 Summary and discussion

In this section I first summarize and briefly interpret my findings. Next, I discuss how my findings establish dipolarizing flux bundles as a major contributor to tail flux transport in Section 3.4.1. Then I draw a picture of the DFB life as a flux transporter based on my results and interpretation in Section 3.4.2. Last I compare DFBs with other flux-transporting tail transients in Section 3.4.3.

To investigate the importance of DFB flux transport, I examined DFBs embedded in bursty bulk flows and found:

- There are typically 1-6 DFBs inside each BBF. The average magnetic field B_z, flow v_x, and electric field E_y (flux transport rate) of the BBF-embedded DFBs are typically 1.5 times, 2 times, and 1.5-4.5 times of those of the entire BBF, respectively.

- Dipolarizing flux bundles take only ∼30% of the BBF duration but contribute ∼67% of the BBF flux transport (for the DFB selection criterion used by Section 2.2.1). They are the effective carriers of the BBFs' magnetic flux. As the BBFs transport 60-100% of the near-earth tail flux while they are observed only for 10-15% of the time (*Angelopoulos et al.*, 1994), the DFBs last ∼4% of the time but are responsible for 40-67% of the flux transport in the near-earth magnetotail (see Section 3.4.1 for more details).

Then I studied the leading DFBs of the leading DFB list and found the following DFB flux transport characteristics:

- Most (∼83%) of leading DFBs travel and transport magnetic flux earthward; only a few (∼17%) rebounding ones transport flux tailward. These percentages are similar to those of earthward and tailward fast flows (e.g., *McPherron et al.*, 2011; *Lee et al.*, 2012). Consistent with fast flows (e.g., *McPherron et al.*, 2011), earthward DFBs travel and thus transport flux faster than tailward ones.

- The leading DFB flux transport rate is higher when the DFBs are observed closer to

Earth or in the tail's pre-midnight sector. The transport rate increases with proximity to Earth and is due to the DFBs magnetic field enhancement; the higher transport rate in the pre-midnight sector is caused by both stronger magnetic field and the faster DFB motion there. However, because the DFB duration is anti-correlated with the flux transport rate, individual DFBs at different downtail and cross-tail locations transport approximately the same amount of flux.

- The leading DFB flux transport rate is higher farther away from the neutral sheet or during higher substorm activity. The higher transport rate leads to more flux transport by individual DFBs under these two conditions. The higher flux transport farther away from the neutral sheet is mainly contributed by vertical flux transport (along Z). The higher flux transport during higher substorm activity is due to the stronger magnetic field inside DFBs. During higher substorm activity, the occurrence rate of leading DFBs (those meeting the DFB selection criteria) is also higher, which further increases the flux transport done by DFBs under high AE.

- Closer to Earth or during higher substorm activity, the semi-permanent increase in B_z after the DFB passage relative to that ahead of the leading DFB is progressively higher, indicating increasingly severe pileup of DFB flux under these two conditions. The DFB pileup close to Earth ($X = -6$ to -10 R_E) leads to a long-term enhancement of the local magnetic field. Far away from Earth ($X = -16$ to -20 R_E), DFBs make little change to the background field after their passage—B_z returns to its pre-DFB level.

- As AE increases the flux transport rate and the net flux transported by leading DFBs as well as the semi-permanent dipolarization accomplished in their aftermath saturate to limited values. Those are likely dependent on location (most of my DFBs are around 9-12 R_E downtail) and represent the fact that after sufficient dipolarization the magnetotail at a given location becomes impermeable to further DFB penetration. AE increases are likely to occur by DFBs at other locations further downtail or towards the flanks.

In addition, I also found the following miscellaneous phenomena that contribute to the DFB flux transport properties:

- The DFBs' δB_z has a minimum at $X =\sim -14$ R_E; it increases toward both the $X =\sim -20$ R_E near-earth reconnection site and the inner edge of the plasma sheet where it reaches maximum. This δB_z minimum location is close to the minimum point of the background B_z ($X =\sim -12$ R_E) (e.g., *Hau et al.*, 1989; *Sergeev et al.*, 1994; *Saito et al.*, 2010), suggesting a possible relationship between the two minimums. The DFBs' v_x shows an anti-correlation with δB_z—it peaks at $X \sim -15$ R_E and decreases toward both the near-earth reconnection site and the inner edge of the plasma sheet where it reaches minimum. The X-dependent magnetic field and flow variations of DFBs are consistent with those of fast flow events (*Hsu et al.*, 2012; *Shiokawa et al.*, 1997).

- The leading DFB's v_x typically decreases within 15 R_E downtail. This reduction in DFB duration with proximity to Earth is evidence of contraction of the DFBs along their streamlines. Likely, this contraction partly leads to an enhancement of the DFB's magnetic field, which overcomes the v_x reduction to result in a continuing enhancement of the DFB flux transport rate from outside to inside of 15 R_E downtail.

- The occurrence rate of DFB samples increases with distance from Earth. This trend is similar to those of bursty bulk flows and rapid flux transport events (*Angelopoulos et al.*, 1994; *Schödel et al.*, 2001); it suggests a close relationship of the three types of events.

3.4.1 The importance of DFBs in magnetotail convection

Dipolarizing flux bundles embedded in bursty bulk flows take only ∼30% of the BBF time but contribute ∼67% of the BBF magnetic flux transport (for a typical DFB selection criterion). So they are responsible for the majority of BBF flux transport due to their high transport efficiency. The rest of the BBF time (∼70%) consists of non-convective flows, background

flows, and DFB-related ambient flow perturbations preceding or trailing the DFBs (e.g., *Zhou et al.*, 2011; *Zhou et al.*), which contribute only little flux transport.

Based on the estimates of *Angelopoulos et al.* (1994) about the percentage of BBFs' contribution in tail flux transport, I can roughly estimate that of DFBs. Due to the THEMIS orbit, most BBFs in my study are observed in the 9-12 R_E downtail region. *Angelopoulos et al.* (1994) showed that the BBFs in this region contribute 30-50% of the tail flux transport in this region, although they are observed for ∼5% of the time in the central plasma sheet (CPS) at that distance. Therefore, although the DFBs embedded in BBFs are observed for ∼1.5% of the time in the 9-12 R_E downtail region, they contribute 20-35% of the tail flux transport there. Because a DFB travels along the tail coherently (*Runov et al.*, 2009) and carries approximately the same amount of flux, I assume DFBs embedded in BBFs tailward of $X =\sim -12$ R_E contribute a similar percentage of BBF flux transport as those in the 9-12 R_E downtail region do. In the 12 to 22 R_E downtail region, BBFs are observed for 10-15% of the CPS time but are responsible for 60-100% of the tail flux transport (*Angelopoulos et al.*, 1994). With my assumption, these BBFs' embedded DFBs appear only 3-4.5% of the CPS time but contribute 40-67% of the tail flux transport.

I can extend the DFBs' 40-67% transport estimation to the entire near-earth magnetotail—from the inner edge of the plasma sheet where the DFBs and BBFs stop to the reconnection site at $X = -20$ to -30 R_E) with further assumptions. The reduction of the BBFs' flux transport with proximity to Earth (from 60-100% to 30-50%) is caused by the reduction of their occurrence rate (from 10-15% to ∼5%). The reduction in the BBF occurrence rate is likely due to the braking of the BBFs closer to Earth (*Shiokawa et al.*, 1997)—flows there slow down below the BBF selection criteria. These slower flows, however, likely have the same flux transport capacity as BBFs further downtail. Therefore, the DFBs embedded inside these slower flows have also the same flux transport capacity as DFBs within BBFs. It is therefore likely that DFBs embedded in BBFs or former-BBF flows are responsible for 40-67% of the near-earth tail flux transport while they appear for only 3-4.5% of the CPS time regardless of downtail distance. Due to the different significance of fast flows for flux transport under different modes of magnetotail transport (*Kissinger et al.*, 2012), the per-

centage of the tail flux transported by DFBs also changes with convection type—it should be highest during steady magnetospheric convection, high during substorms, and low during quiet time. Overall, however, traveling DFBs will be observed a little more than 3-4.5% of the time, but will contribute more than 40-67% of the near-earth tail flux transport. Dipolarizing flux bundles are the dominant and the most effective carriers of flux in the near-earth magnetotail. As these flux finally gets convected to the inner magnetosphere, DFBs play a major role in magnetotail convection.

I can make a rough estimation about what portion of the lobe flux is transported by the DFBs. The typical flux transport of each individual DFB is ∼0.6MWb per R_E in Y (e.g., Figure 3.6e). Considering its typical Y-width of ∼3 R_E (e.g., *Sergeev et al.*, 1996, ; Section 2.3.2.3), the total amount of magnetic flux carried by a DFB is ∼1.5 MWb, which is transported within the typical ∼40s DFB duration. Therefore, during a typical 60-min substorm expansion and recovery phase (*Akasofu*, 1964), DFBs transport ∼135MWb magnetic flux, assuming that their flux transport is continuous (satellites do not observe continuously appearing DFBs because after the first DFBs have dipolarized the inner magnetosphere later DFBs stop tailward of the satellite). The ∼ 135MWb flux is transferred from the lobe to the DFBs and then transported earthward by the DFBs to the geosynchronous orbit, during which some of the magnetic energy is converted to plasma kinetic and thermal energy. This amount transferred to the DFB is consistent with previous estimates of lobe flux reduction during substroms; it is a significant portion of the 500-1500 MWb tail lobe flux (e.g., *Milan et al.*, 2007; *Shukhtina et al.*, 2009). More quantitative estimates of total transport, including energy conversion can be done for individual cases, or even statistically, assuming a total lobe flux monitor such as ARTEMIS (*Angelopoulos et al.*, 2013).

3.4.2 A picture of the DFB life as a flux transporter

Further interpreting the aforementioned DFB flux transport characteristics, especially the X-dependent characteristics, I can understand the history of an individual DFB. Through reconnection at $X < -20$ R_E, magnetic flux, and thus energy, stored in the lobes is released

to newly-generated DFBs. More flux is transferred to the DFBs from the lobes when the substorm activity level is higher, leading to stronger δB_z. Then each newly-generated DFB moves earthward carrying along its magnetic flux. At the beginning, the DFB is accelerated because in its vicinity the earthward magnetic curvature force is larger than the tailward total pressure gradient force (*Li et al.*, 2011). Its speed peaks at $X =\sim -15$ R_E; then its earthward motion is inhibited because within 15 R_E downtail the tailward pressure gradient force exceeds the earthward curvature force (e.g., Chapter 4; *Shiokawa et al.*, 1997). The location where the DFB velocity starts to decrease ($X =\sim -15$ R_E) is the same as that inferred by *Shang et al.* (2013) from multi-point observations. Finally the DFBs stop (some of them overshoot, rebound and then stop (e.g., *Chen and Wolf*, 1999; *Panov et al.*, 2010)) and deposit their magnetic flux and energy at the inner edge of the plasma sheet. Overall in the near-earth tail, 40-67% of the lobe flux is transported to the inner magnetosphere in this way during a very short time.

Dipolarizing flux bundles do not only transport flux earthward but contract at the same time. The contraction of the DFB flux tube in Z also results in north-south flux transport which is especially significant at large distances from the neutral sheet. The Z-expansion of the DFB can transport flux away from the neutral sheet too; this expansion may be more likely to happen at the near-earth portion of the DFB flux tube (*Ober et al.*, 2001). To understand the relative importance of the DFBs' flux transport towards and away from the neutral sheet, more careful studies are needed with multiple spacecraft at various altitudes observing the same flux tube. This is possible using past THEMIS alignments during solar minimum and future THEMIS-MMS alignments during solar maximum.

3.4.3 The relationship between DFBs and other tail transients

Dipolarizing flux bundles possess the rapid flux transport signature of a strong electric field, so a lot of DFBs can also be classified as RFTs. My results indeed show that DFBs share similar flux transport properties with rapid flux transport events. They both have strong B_z, v_x, E_y, a similar occurrence rate variation with downtail distance, and a similar E_y variation

with cross-tail distance (*Tu et al.*, 2000). In addition, they both have a time scale much shorter than bursty bulk flows. These similarities confirm the strong relationship between DFBs and RFTs. However, not all RFTs coincide with DFBs. Any tail transient that has a strong electric field (E_y, v_xB_z, or v_yB_z according to different definitions) is an RFT (for example, a flux rope).

One difference between DFBs and RFTs is their durations—the typical duration of DFBs is ∼40s, while that of RFTs is ∼20s (*Schödel et al.*, 2001). As the definition of the RFT necessitates a strong electric field, a DFB-related RFT is most likely the transport-effective part of a DFB. Therefore, magnetotail transients follow a hierarchy: a ∼10-min-duration bursty bulk flow contains flow bursts of $>$ 1-min time scale (see Figure 3.1a); a flow burst envelops a ∼40s-duration DFB; a DFB contains an RFT of ∼20s duration.

The DFBs are the central link of the hierarchy. *Li et al.* (2011) showed that the strong magnetic field inside the DFB results in an earthward magnetic curvature force which overcomes the tailward pressure gradient force to lead to the DFB's flow. Thus, the DFBs are the drivers of the flow bursts which combine with strong magnetic field to be RFTs and collage to be BBFs. In addition to contributing 67% of the BBF flux transport, the DFBs also excite ambient flows preceding and trailing them, which are responsible for most of the rest of the BBF flux transport. Therefore, DFBs drive nearly all the BBF flux transport, which is 60-100% of the near-earth tail flux transport. I conclude that DFBs are not only the carriers but also the drivers of the major and most efficient flux transport in the near-earth magnetotail.

CHAPTER 4

The controlling factor and the results of the dipolarizing flux bundles' motion

As a dipolarizing flux bundle (DFB) moves earthward, it creates pressure and flow perturbations. These perturbations may play a significant role in controlling DFB motion and generating field-aligned currents (FACs). To investigate this hypothesis I use DFB observations from the THEMIS mission to reconstruct the spatial profiles of the thermal and total (thermal plus magnetic) pressures and of the plasma flow near the DFB. The total pressure reaches maximum inside the dipolarization front (DF, the leading edge of the DFB). The resultant pressure gradient force pushes ambient plasma in the direction normal to the front and exerts a gradient force density of $\sim$0.15 nPa/R_E against the DFB motion. The thermal pressure in the equatorial plane is strongest immediately ahead of the DFB's leading point; it decreases with distance from that peak: toward the ambient plasma, toward the DFB interior, and toward the DFB flanks. Combining my estimate of the flux tube volume distortion by the flow profile with the measured equatorial thermal pressure distribution I obtain a region-1-sense FAC inside the DF layer and region-2-sense FAC in the $\sim$1-R_E thick region immediately ahead of it, similar to the FAC directions of a substorm current wedge.

4.1 Introduction

The earthward motion of a dipolarizing flux bundle results in buildup of total (magnetic plus thermal) and thermal pressures ahead of it (e.g., *Zhou et al.*, 2010; *Li et al.*, 2011; *Palin et al.*, 2012). The total pressure buildup exerts two pressure gradient forces—a tailward force directed toward the inside of the DFB and an earthward force directed toward the ambient

plasma. The tailward force decelerates the DFB's earthward motion; the earthward force pushes ambient plasma ahead of the DFB (*Li et al.*, 2011), forming a flow vortex on each side of it (e.g., *Keiling et al.*, 2009). Field-aligned currents (FACs) may arise as demanded by these vortices (e.g., *Birn et al.*, 2004a) or the thermal pressure buildup (e.g., *Yang et al.*, 2011).

The role of the total pressure gradient in controlling DFB motion and the generation of FACs near the DFB are still not fully understood. I will deal with these two topics by investigating the pressure and flow distribution near the DFB.

4.1.1 The mechanism controlling DFB motion

As a magnetized bulk plasma, a DFB's change of velocity ($d\mathbf{v}/dt$) is controlled by the magnetohydrodynamics equation

$$\rho\frac{d\mathbf{v}}{dt} = -\nabla(P_{\rm th} + \frac{B^2}{2\mu_0}) + \frac{1}{\mu_0}(\mathbf{B}\nabla)\mathbf{B}, \tag{4.1}$$

where $\mathbf{v}$ is the plasma bulk velocity, ρ is the plasma density, and $P_{\rm th}$ is the plasma pressure (e.g., *Shiokawa et al.*, 1997). Therefore, the relative magnitudes of the total pressure ($P_{\rm th} + B^2/2\mu_0$) gradient force and the magnetic curvature force ($(\mathbf{B}\nabla)\mathbf{B}/\mu_0$) decide the acceleration or deceleration of the DFB motion. As mentioned above, the total pressure exerts a tailward force that opposes the DFB's earthward motion. An earthward magnetic curvature force caused by the DFB's dipolar field lines accelerates the plasma earthward. *Li et al.* (2011) found that for a single event this curvature force dominates at some portion of the DFB's lifetime. A statistical study by *Shiokawa et al.* (1997), however, showed that BBFs (which envelop DFBs) eventually slow down near the Earth, indicating that the tailward pressure gradient force dominates there. At the end of the earthward motion of a DFB, it may even rebound tailward (*Chen and Wolf*, 1999; *Panov et al.*, 2010) due to this tailward force. More investigation is needed to determine the relative magnitude of the total pressure gradient and curvature forces.

4.1.2 Dipolarizing flux bundle-associated FACs

Although the major current of the DFB is a duskward current on the dipolarization front (DF, the leading edge of the DFB) (e.g., *Runov et al.*, 2011; *Zhang et al.*, 2011; *Fu et al.*, 2012), an association between field-aligned currents and DFBs has been suggested by observations of equatorward-moving auroral streamers in the ionosphere that coincide with DFBs in the magnetotail (e.g., *Nakamura et al.*, 1993, 2001; *Zesta et al.*, 2000; *Kauristie et al.*, 2003). Direct observations of dipolarization front current have confirmed this association (e.g., *Nakamura et al.*, 2008).

The substorm current wedge (SCW), a current system critical to the substorm process (*McPherron et al.*, 1973), also consists of FACs, which have been considered related to the DFBs' FACs (e.g., *Birn et al.*, 1999). The study of DFB FAC generation can improve our understanding not only of DFB evolutionary dynamics but also of substorm current wedge formation.

4.1.2.1 Field-aligned current associated with thermal pressure distribution

Field-aligned currents appear when thermal pressure isosurfaces do not overlap surfaces of equal flux tube volume (*Vasyliunas*, 1970) in the magnetosphere:

$$j_{\parallel,\mathrm{i}} \approx \frac{B_\mathrm{i}}{B_\mathrm{eq}} \mathbf{b}_\mathrm{eq} \cdot (\nabla V \times \nabla P_\mathrm{eq}), \tag{4.2}$$

where $j_{\parallel,\mathrm{i}}$ represents a FAC into (when positive) or out of (when negative) the ionosphere; B_i and B_eq are the field strength at the ionosphere and equatorial plane, respectively; $\mathbf{b}_\mathrm{eq}$ is magnetic field direction at the equatorial plane; and P_eq and $V = \int \frac{ds}{B}$ (ds is a length element along the magnetic field line) are the equatorial thermal pressure and the flux tube volume of unit magnetic flux, respectively. Equation 4.2, derived under the assumption of slow flow (force balance), may describe the closure of the substorm current wedge FACs (e.g., *Yao et al.*, 2012; *Birn and Hesse*, 2013) and the FACs near the DFB. In the multi-fluid simulation of (*Yang et al.*, 2011), also applicable for conditions of slow flow, an earthward-

moving DFB builds up a region of high thermal pressure ahead of it, that results in pressure gradients radially toward the DF and azimuthally towards the meridian of the DFB's leading point. When combined with the calculated flux-tube volume, these pressure gradients require region-1-sense (toward/away from Earth on the DFB's dawn/dusk side) FACs inside the dipolarization front layer, and region-2-sense (opposite to region-1-sense) FAC earthward of the DFB. Although (*Yang et al.*, 2011, 2012) focused on the time when the DFB stops near geosynchronous orbit, their simulated FAC locations may also apply to traveling DFBs. In addition, observational investigations of Equation 4.2's qualitative validity for incoming flow bursts showed that thermal pressure gradients in the Y-direction ahead of DFBs point toward the meridian of DFB-associated substorm auroral intensification (*Xing et al.*, 2011, 2012) and are consistent with the *Yang et al.* (2011, 2012) simulations of the pressure distribution. The multi-point pressure observations of *Xing et al.* (2011, 2012) are suggestive of FAC closure through equatorial azimuthal pressure gradients, but a comprehensive reconstruction of such FAC closure has not yet been possible due to the lack of a large number of satellites that can determine the equatorial pressure gradients at multiple locations simultaneously. As I shall see, this deficiency can now be overcome by constructing two dimensional profiles of median quantities over a large number of DFB crossings.

4.1.2.2 Field-aligned current associated with flow vortices

As mentioned above, when a DFB's earthward motion pushes the ambient plasma sideways, flow vortices form on the DFB's dawn and dusk sides. In simulations these two vortices lead to region-1-sense FACs (e.g., *Birn et al.*, 2004a). Simulations also show that region-2-sense FACs can also arise from flow shears created as a DFB diverts ambient plasma at the inner edge of the plasma sheet (e.g., *Birn et al.*, 1999). Only few multi-spacecraft case studies of the flow vortices on the DFB's sides have been published (e.g., *Keiling et al.*, 2009). To improve our understanding of FAC generation due to flow vortices and/or flow shear, a statistical study of the flow pattern surrounding DFBs is necessary.

In this paper I explore (1) how the force balance condition controls DFB motion and (2)

how DFB-associated FACs are generated, by investigating the pressure and flow distributions near the DFB. Using the XY statistical map reconstruction technique introduced in Appendix C, I examine the spatial distributions intuitively by means of ensemble medians for each quantity. For conciseness, I only show the results for the 506 earthward-normal (93% of them are earthward-moving) leading DFBs whose normal directions are determined by the $\mathbf{B}_{\text{in}} \times \mathbf{B}_{\text{out}}$ method (see Appendix B).

4.2 Results

I investigate the DFB force balance condition by reconstructing total pressure distribution, and explore the field-aligned current generation by reconstructing thermal pressure and plasma flow distributions.

4.2.1 Total pressure distribution

In this section I first examine the commonly-used total pressure which includes the plasma pressure and the contribution from all three magnetic field components. Second, I examine the radial total pressure (total pressure minus the magnetic pressure from the magnetic field's radial component) because it is more relevant to the DFB motion than the total pressure. Third, I examine the vertical total pressure (total pressure minus the magnetic pressure from the B_z), the distribution of which also shows interesting features.

I present the reconstruction of total pressure distributions inside and outside the DFB in Figure 4.1. The time-series of all the pressure data that went into Figure 4.1 have been detrended by subtracting the quiet time average (evaluated from $t_0 - 3$min to $t_0 - 2$min, see Section 2.2.1).

Figures 4.1a and 4.1b show the distribution of the total pressure, $P_{\text{ttl}} = B^2/2\mu_0 + P_{\text{th}}$; P_{th} is the thermal pressure. P_{ttl} is strongest in the radial bin immediately behind the DFB's outer boundary. This radial bin's thickness is ~1000 km, which is also the typical dipolarization front thickness (*Runov et al.*, 2011). Therefore, P_{ttl} peaks inside the DF layer and decreases

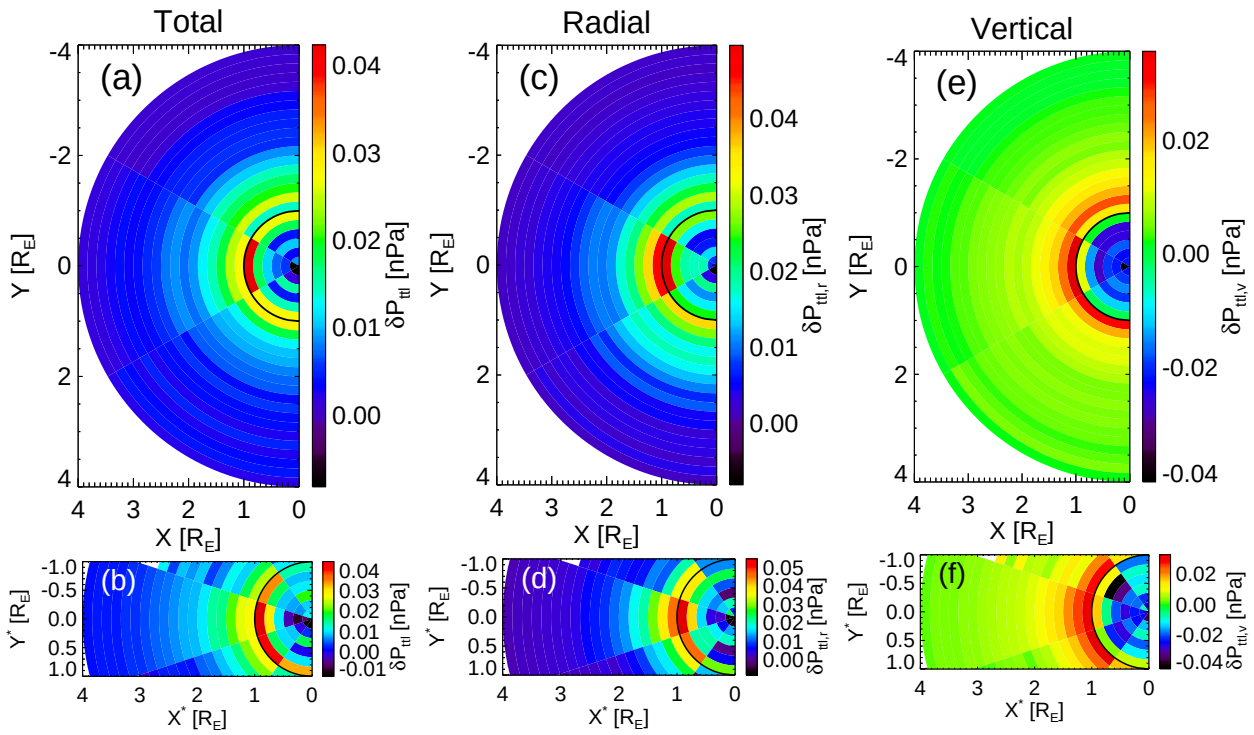

Figure 4.1: Spatial distribution of detrended (with quiet-time value) total pressures binned with azimuth and radial distance from the DFB center. The upper panels (a, c and e) are reconstructed from satellite paths in Figure C.1a and the lower panels (b, d, and f) from satellite paths in Figure C.1b. The color in each bin represents the median value of data points collected along all satellite-path segments (each segment from an individual event) that fall into that bin. The binning area is within 4 R_E radial distance of the DFB center and $\pm 90^o$ azimuth from the X or X^* axis. Bins containing less than five satellite-path segments are not colored (such bins appear in Figures 4.1b, 4.1d and 4.1f). The black semicircles denote the DFB's outer boundary. Figures 4.1a and 4.1b show the total pressure with magnetic pressure containing contributions from all magnetic field components. In Figure 4.1c and d the total pressure excludes the contribution from the magnetic field's radial (from the DFB center) component. In Figures 4.1e and 4.1f, B_z is excluded from the total pressure calculation.

towards the ambient plasma and towards the DFB's interior. This radial variation of $P_{\rm ttl}$ is consistent with the results of *Palin et al.* (2012). $P_{\rm ttl}$ also has an azimuthal variation near the DF—it peaks at the central azimuth (zero azimuth, the meridian of the DFB's earthward-most point or leading point) and decreases toward the DFB's flanks.

Although the total pressure affects DFB motion, it is not the most relevant quantity for DFB motion as its gradient includes other stresses associated with vertical tail pressure balance. To get the most relevant pressure, I need to subtract from the total pressure the part that is irrelevant to DFB motion, namely the pressure from the magnetic field component along the DFB motion. This is because the magnetic pressure force is not acting in the direction along the magnetic field. Therefore, I subtract from the total pressure the magnetic pressure from the component along the controlling force of the DFB motion. As the DFB motion is mainly parallel to the XY plane, its controlling force is in the direction of n_{XY}, the XY component of the DF normal direction. This direction is also the radial direction (relative to the DFB center) in my reconstruction. The most relevant pressure to DFB motion is thus the radial total pressure $P_{{\rm ttl},r} = (B^2 - B_r^2)/2\mu_0 + P_{\rm th}$, where B_r is the magnetic field's radial component.

Figures 4.1c and 4.1d show the distribution of detrended $P_{{\rm ttl},r}$. The distribution of the radial total pressure is similar to that of total pressure—it peaks inside the DF layer and the central azimuth; the $P_{{\rm ttl},r}$ gradient force points from the DF layer toward the ambient plasma and towards the interior of the DFB. I estimate the $P_{{\rm ttl},r}$ gradient with superposed epoch analysis in Figure 4.2. The vertical epoch-zero line in Figure 4.2 corresponds to the black semicircles in Figure 4.1. Behind the vertical line in Figure 4.2c, $P_{{\rm ttl},r}$ drops by $\sim$0.06 nPa within $\sim$20 seconds. Twenty seconds correspond to a thickness of 0.4 $\rm R_E$ given that the median DF-normal component of the DF convective velocity is 137 km/s. The radial total pressure gradient is thus $\sim$0.15 nPa/$\rm R_E$. The radial total pressure drop exists over the entire DFB region as the drop aligns well with the B_z enhancement region in Figure 4.2a.

In Figures 4.1a-4.1d I have used the smallest possible bins in which trends are clear. In Figures 4.1b and 4.1d azimuthal pressure trends show up in smaller bins than in Figures 4.1a and 4.1c, suggesting that data are better organized in the X^*Y^* coordinate system than in

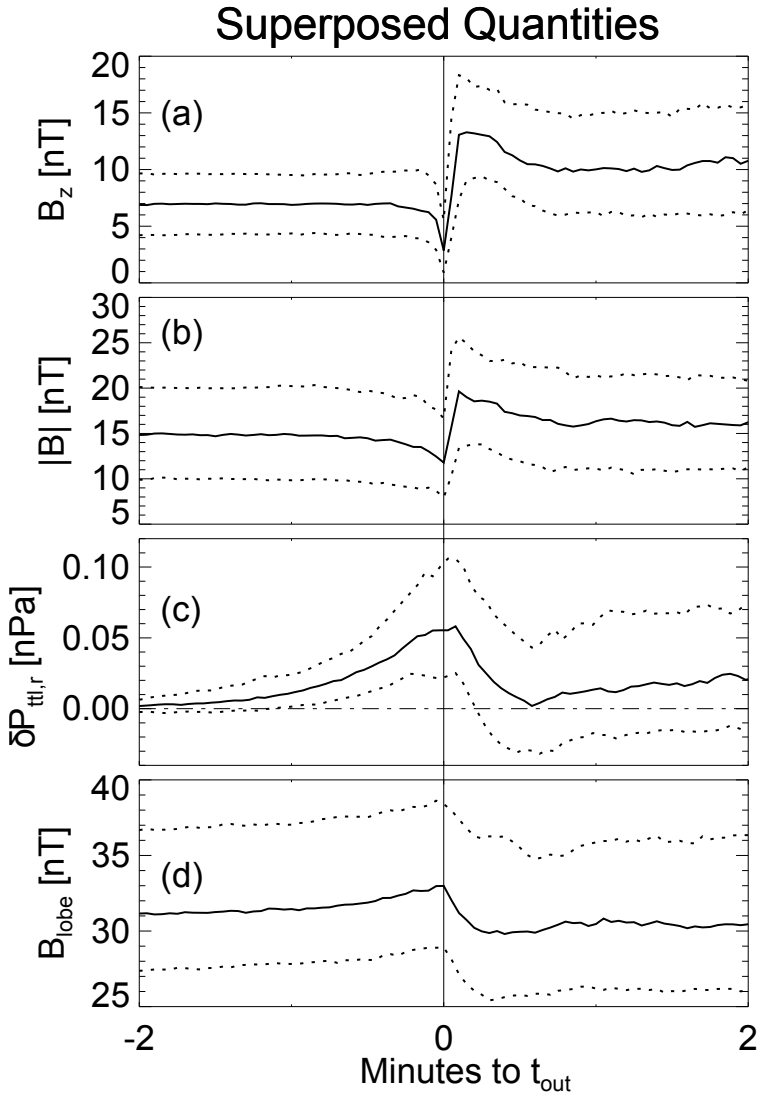

Figure 4.2: Superposed epoch analysis of B_z (a), field strength (b), detrended radial total pressure (c), and inferred lobe field (d). The three lines in each panel are the upper quartile, median, and lower quartile of the values from 506 events.

GSM coordinate system.

In Figures 4.1e and 4.1f I investigate the distributions of vertical total pressure, $P_{\mathrm{ttl,v}} = (B_x^2 + B_y^2)/2\mu_0 + P_{\mathrm{th}}$. The vertical total pressure takes part in the net force density along the Z direction, $f_z = -dP_{\mathrm{ttl,v}}/dz + B_x dB_z/\mu_0 dx + B_y dB_z/\mu_0 dy$, which is zero under the north-south force balance assumption. Assuming planar geometry along the XY plane, f_z's last two terms, which represent magnetic curvature force, can be ignored. Then $P_{\mathrm{ttl,v}}$ holds constant along the Z direction—it equals the plasma pressure at the neutral sheet (P_{eq}) and the magnetic pressure in the lobe. Figures 4.1e and 4.1f show that $P_{\mathrm{ttl,v}}$ builds up ahead of the DFB and drops drastically inside it. This drop suggests that the DFB causes lobe field reduction, which is also a reduction in the local cross-tail current. In Figure 4.2d I demonstrate the lobe field reduction in another form by calculating the lobe field as $B_{\mathrm{lobe}} = \sqrt{2\mu_0 P_{\mathrm{ttl,v}}}$. This DFB-related lobe field and cross-tail current reduction is consistent with the findings of *Palin et al.* (2012). Moreover, Figures 4.1e, 4.1f and 4.2d show that local cross-tail current reduces immediately when one moves from outside to inside the dipolarizing flux bundle. Such reduction is a natural result of diversion of the cross-tail current onto the DF (see Figure 5.4).

In addition to the vertical direction, the $P_{\mathrm{ttl,v}}$ gradient is also effective along other directions that are perpendicular to the magnetic field's XY component. The drop of $P_{\mathrm{ttl,v}}$ across the DFB's outer boundary in Figures 4.1e and 4.1f indicates that the $P_{\mathrm{ttl,v}}$ gradient force in these other directions tries to contract the DFB.

The total pressure distributions in Figure 4.1 are largely due to thermal pressure variations. Because the thermal pressure variation is closely related to the field-aligned current, I conduct a detailed investigation of it in the next section.

4.2.2 Thermal pressure distribution

To investigate field-aligned current closure near the DFB, I reconstruct thermal pressure maps around the DFB. First I show the general thermal pressure distribution regardless of distance from the neutral sheet. Then I project the thermal pressure to the equatorial plane

to get the distribution of equatorial thermal pressure, which is a factor in Equation 4.2.

Figure 4.3 shows the detrended thermal pressure distribution around the DFBs. The thermal pressure inside DFBs is much smaller than outside (e.g., *Runov et al.*, 2011, Section 2.2.1). To prevent this large difference from diminishing the variations inside or outside the DFBs by widening the color maps, I investigate the thermal pressure distribution for each side separately. Figures 4.3a-4.3c show the distribution outside the DFB. Thermal pressure increases from the ambient plasma towards the DFB in all azimuths and reaches ∼0.04 nPa more than the ambient thermal pressure. Such a thermal pressure buildup is a typical signature of approaching DFBs (e.g., *Zhou et al.*, 2010, 2011; *Runov et al.*, 2011). At small radial distances to the DFB, the thermal pressure peaks in the central azimuth and reduces monotonically towards large (in absolute value) azimuths. This azimuthal trend extends to ∼1 R_E ahead of the DFB, resulting in an azimuthal component of the thermal pressure gradient directed towards the central meridian. This trend can show up in even smaller radial and azimuthal bins in Figure 4.3b than in Figure 4.3a, indicating that thermal pressure is well organized in the X^*Y^* coordinate system.

In Figure 4.3b, at the radial distances very close to the DFB the thermal pressures at duskside bins are larger than those of dawnside bins. Such dawn-dusk asymmetry is also present in the GSM coordinate system if I use large bin size in Figure 4.3c.

Next I move inside the DFB. For this case, the X^*Y^* coordinate system orders the data so much better than the XY (GSM) system that I only show the result in the former system (Figure 4.3d). The thermal pressure peaks at the central azimuth in the ∼0.5-R_E-thick region behind the DFB's outer boundary—a thermal pressure gradient toward the central azimuth exists in the ∼1000-km-thick DF layer as well as deeper inside the DFB.

One can already evaluate the DFB-associated field-aligned currents based on the thermal pressure distributions in Figure 4.3. However, the evaluation is more convenient if I obtain the thermal pressure distribution in the equatorial plane (more precisely, the neutral sheet), which allows the direct application of Equation 4.2. (The evaluation also requires flux tube volume distribution, see Section 4.3.3.)

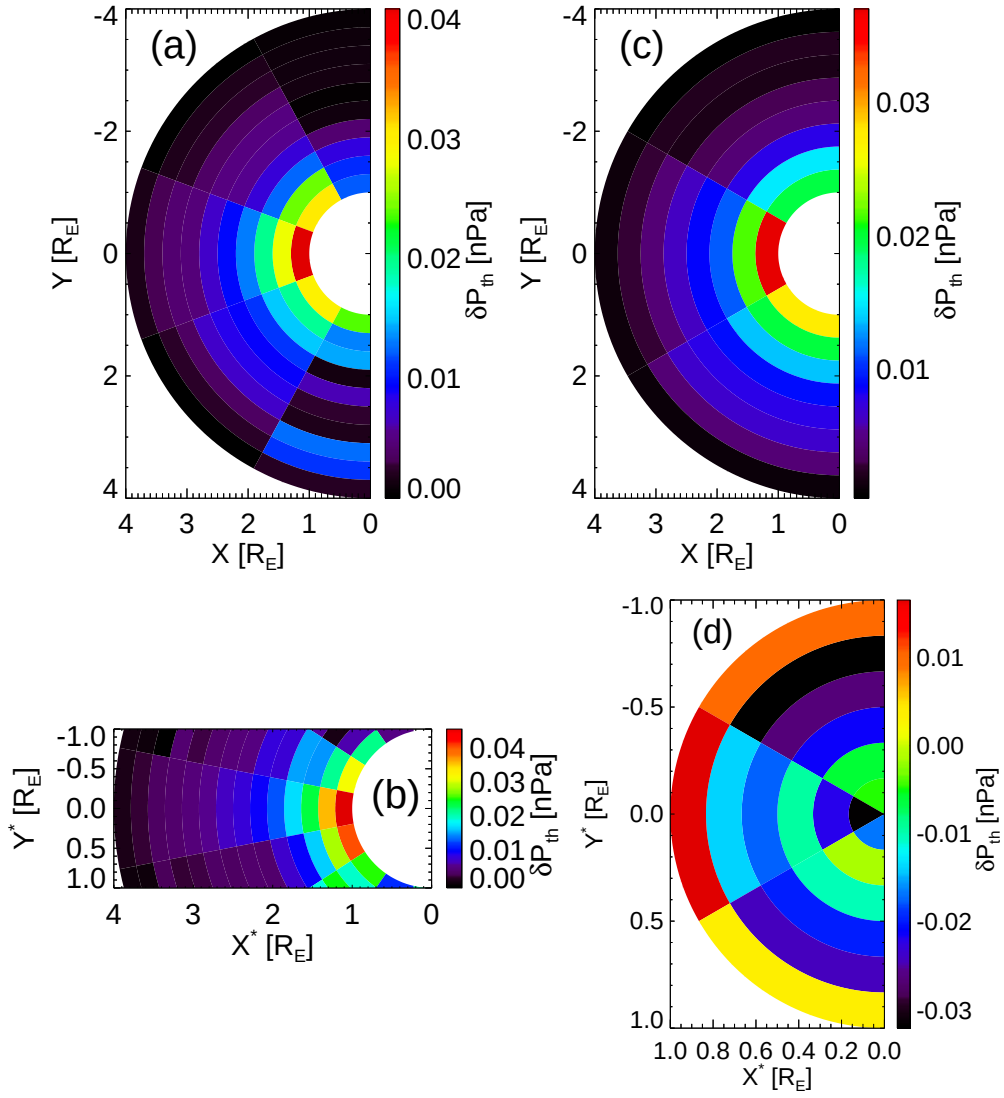

Figure 4.3: Detrended thermal pressure distribution in the same format as in Figure 4.1. Figures 4.3a and 4.3c are reconstructed from the satellite paths in Figure C.1a; Figures 4.3b and 4.3d are reconstructed from the satellite paths in Figure C.1b. Figures 4.3a-4.3c show only the distribution outside the DFB; Figure 4.3d shows only the region inside the DFB. Figure 4.3c is a larger-bin representation of Figure 4.3a.

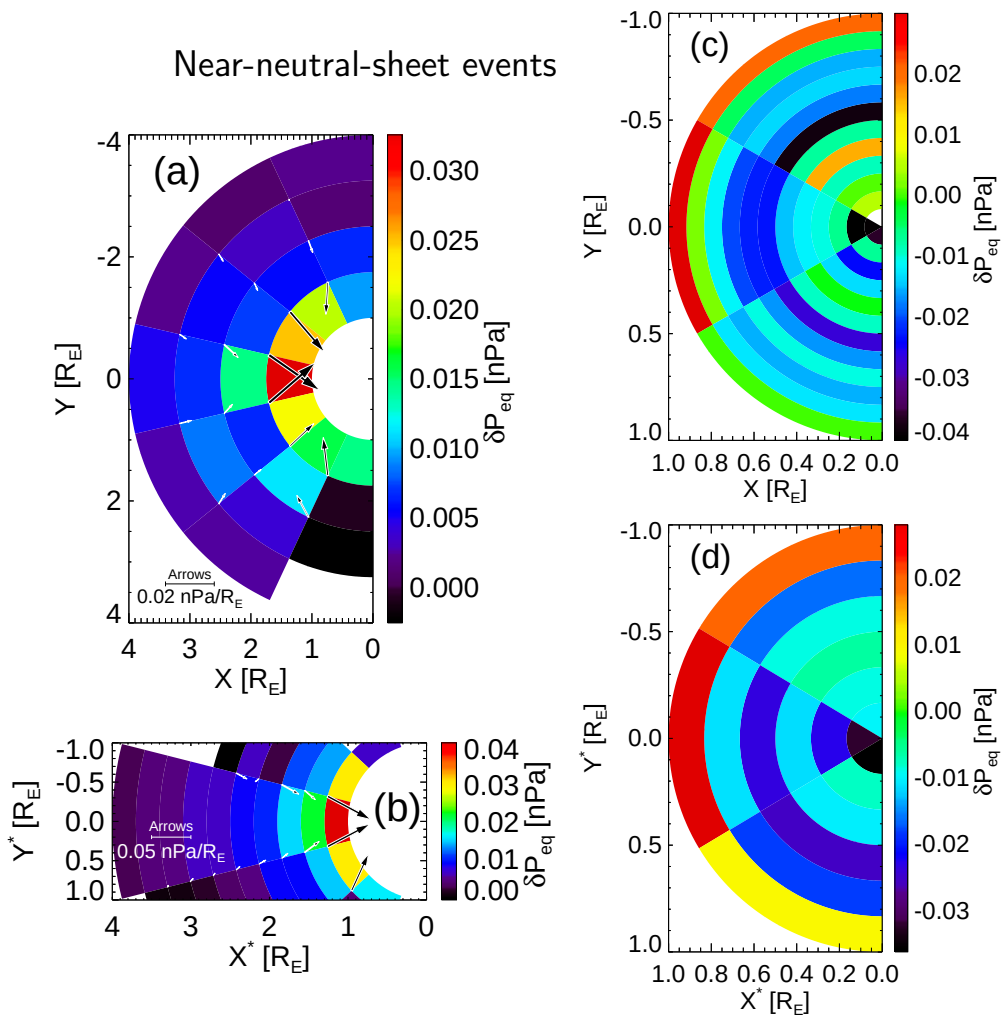

Figure 4.4: Distribution of detrended equatorial thermal pressure organized in the same format as Figure 4.3. All panels include only events near the neutral sheet ($|B_{qx}/B_{\mathrm{lobe,q}}| < 0.3$). Figures 4.4a and 4.4c are reconstructed from the satellite paths in Figure C.1a; Figures 4.4b and 4.4d are reconstructed from the satellite paths in Figure C.1b. Figures 4.4a and 4.4b show only the distribution outside the DFB; Figures 4.4c and 4.4d show only the region inside it. The arrows in Figures 4.4a and 4.4b illustrate the gradients of the bin medians. I calculate each gradient arrow from bin medians of the four bins surrounding the point where the arrow's tail is put. The gradient's radial component is the average of the radial gradients in the two azimuths (each containing two radial bins); the azimuthal component is the average of the azimuthal gradients in the two radial distances (each containing two azimuthal bins). The bin centers are used to infer distances in gradient calculation.

The equatorial thermal pressure $P_{\rm eq}$ equals the vertical total pressure $P_{\rm ttl,v}$ when the north-south force balance is valid and the Z component of magnetic curvature force is neglected (see Section 4.2.1). In reality, however, the Z component of the curvature force has integrated effect along Z. Due to such integrated contribution, the farther away from the neutral sheet the more $P_{\rm ttl,v}$ deviates from $P_{\rm eq}$. Thus, only for events near the neutral sheet can I use $P_{\rm ttl,v}$ to represent $P_{\rm eq}$ and show its distribution in Figure 4.4. Figure 4.4 shows that $P_{\rm eq}$ increases radially inward on both sides of the DFB's outer boundary towards it. Moreover, $P_{\rm eq}$ increases azimuthally on both sides of the central azimuth towards the central azimuth, as is obvious in both the 1-R_E-thick region ahead of the DF (Figures 4.4a and 7b) and the 1000-km-thick DF layer (Figures 4.4c and 4.4d).

The Y component of statistical $P_{\rm eq}$ gradients (arrows in Figures 4.4a and 4.4b) can reach 0.047 nPa/R_E, and is of the same scale as those in the *Xing et al.* (2012) events (0.03 to 0.1 nPa/R_E). I note that the gradients in Figures 4.4a and 4.4b underestimate the maximum $P_{\rm eq}$ gradient ahead of a DFB: Each arrow is obtained from the values of the four surrounding bins resulting in spatial resolution of $\sim$1 R_E, which is likely smaller than the gradient scale length. Further evidence for this aliasing effect is evident in the fact that the gradient vectors in the larger bin-size panel of Figure 4.4a are much smaller than those in smaller bin-size panel of Figure 4.4b.

I will further discuss how these $P_{\rm eq}$ gradients necessitate the existence of field-aligned currents in Section 4.3.3.

4.2.3 Plasma flow distribution

Plasma flow vortices may also lead to field-aligned currents. To explore this possibility further, I reconstruct the plasma flow distribution near the dipolarizing flux bundle.

Figure 4.5 shows the reconstructed plasma flow distribution. Because my reconstruction method is applied in the XY plane, the distribution is of only the XY component of the plasma flow. In Figures 4.5a and 4.5b, the strongest flows appear immediately inside the DFB. Figure 4.5a shows that these flows are mostly in the earthward direction. They also

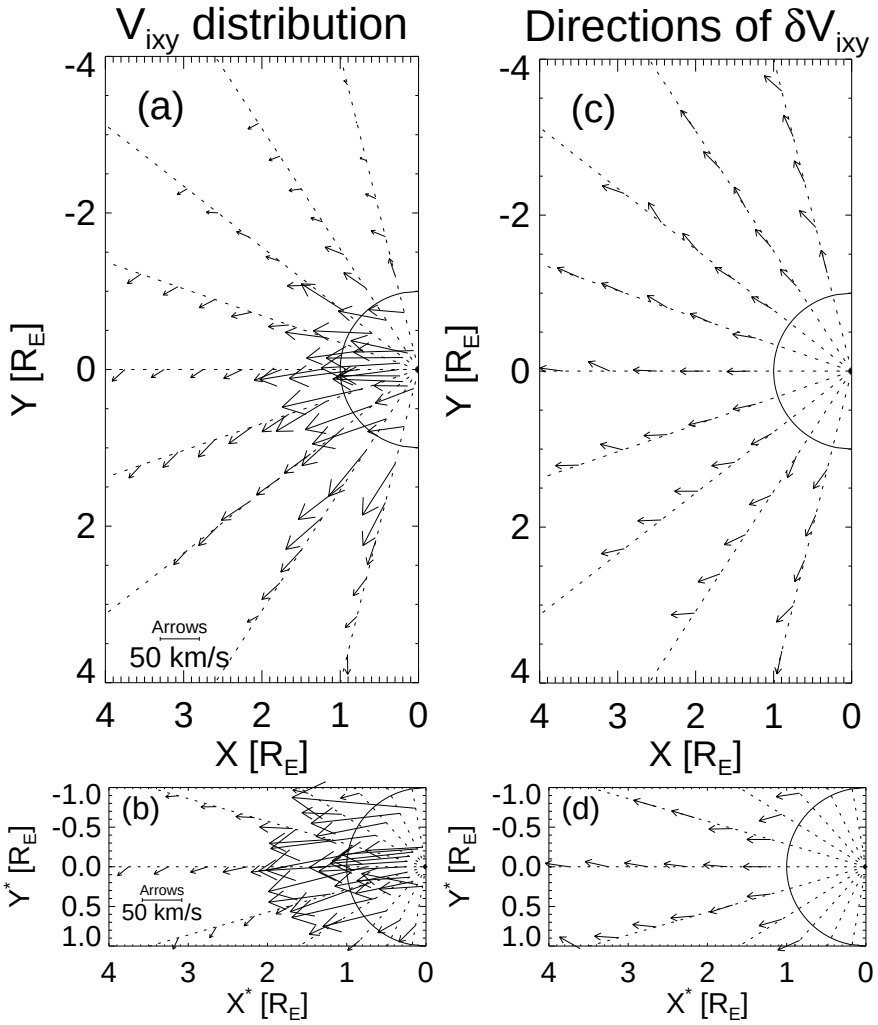

Figure 4.5: Ion bulk flow's XY component near the DFB illustrated on a 2-D map binned in the same manner as the maps in Figures 4.1, 4.3, and 4.4 (in panels a and b flows are not detrended; in panels c and d they are). The black semicircle represents the DFB's outer boundary. The dotted lines are lines of constant azimuth. Figures 4.5a and 4.5c are reconstructed from the satellite paths in Figure C.1a; Figures 4.5b and 4.5d are reconstructed from the satellite paths in Figure C.1b. The arrow in each bin represents the median value of that bin, and its tail is placed at the center of the bin. Figures 4.5c and 4.5d show the distribution of detrended flow outside the DFB. I first get the median detrended flow in each bin and then normalize the median to represent the flow direction.

align well with the DF's convective motion direction in Figure 4.5b; velocity from plasma measurement agrees with that from electric field measurement. The flows immediately outside the DFB are also strong, but point radially away from the dipolarization front. Such radial flows persist in the ambient plasma farther away from the DFB with smaller amplitudes. These radial flows are consistent with the ambient plasma being pushed away in the DF normal direction by the approaching DF via radial pressure gradient force pointing from the DF towards the ambient plasma (see $P_{\mathrm{ttl},r}$ distribution outside the DFB in Figures 4.1c and 4.1d). In the ambient plasma, the flow vectors also have a duskward component from diamagnetic drift associated with the plasma pressure gradient towards the neutral sheet and towards the Earth (*Angelopoulos et al.*, 1993, 1994).

In Figures 4.5c and 4.5d, the distribution of detrended flow (quiet time value removed) reveals a secondary flow pattern that has been masked by ambient diamagnetic flow. The detrended flow in the ambient plasma to the dusk side of the DFB has a dawnward azimuthal component. The dawnward flow in the ambient plasma has been explained in the kinetic framework as ions' gyromotion after DF reflection (*Zhou et al.*, 2011, 2012). Therefore, the dawnward flow component to the duskside of the DF indicates stronger reflection effect at a DF's duskside than at its dawnside.

Flow vortices, which have been suggested to be responsible for DFB-associated FACs (e.g., *Birn et al.*, 2004a, 2013), do not appear in statistical flow patterns in Figure 4.5. Since the flow vortices are caused by the DFB's interchange motion, they are expected to show up only when data are organized by DFB motion direction as in Figures 4.5b and 4.5d. However, Figures 4.5b and 4.5d have a limited lateral range excluding the regions to the dawn and dusk sides of the DFB; these excluded regions are where flow vortices are expected to appear. This limitation is due to my usage of only DFB-transecting measurements to reconstructing the statistical maps. Measurements from satellite paths that are near the DFB but do not transect it are needed to enlarge the range of Figures 4.5b and 4.5d. I plan to incorporate such observations in the future.

4.3 Summary and Discussion

In this section I first summarize my findings. Next, I discuss the nature of my observed pressure and flow distributions. Then I discuss how my observations shed light on the force balance condition that controls DFB motion. Last, I discuss how my observed thermal pressure distribution requires field-aligned currents to arise near the DFB and how my findings are related to the substorm process.

To unravel the force balance condition, which controls the DFB motion, I reconstructed statistical maps of total pressures around the DFB. From these maps,

- I examined the total pressure ($P_{\rm ttl}$) and radial total pressure ($P_{{\rm ttl},r}$, modified total pressure excluding the magnetic pressure component that is ineffective in the direction of DF normal's XY projection). I found that both quantities peak inside the dipolarization front layer at its central meridian (zero azimuth relative to the DFB center) and decrease towards all directions away from that peak. Specifically, the pressure decreases radially towards the ambient plasma, towards the DFB interior, and toward larger azimuths. The $P_{{\rm ttl},r}$ buildup results in a tailward gradient force density of $\sim$0.15 nPa/$\rm R_E$ (on average, and likely an underestimate) that brakes the DFB's earthward motion. This gradient force density is larger than the large-scale tailward total pressure gradient force density of $\sim$0.07 nPa/$\rm R_E$ (*Shiokawa et al.*, 1997).

To investigate the relationship between the DFB's thermal pressure buildup and field-aligned currents, I reconstructed statistical maps of the thermal pressure around the DFB and found that:

- The thermal pressure builds up immediately ahead of the DFB. It is strongest at the DFB's central meridian and reduces toward larger azimuths both earthward of and inside the DF layer. The thermal pressure retains such distribution when projected to the equatorial plane.

- The thermal pressure is slightly higher on the DFB's duskside than on its dawnside.

To determine whether DFB-associated flows can generate FACs, I reconstructed statistical maps of plasma flow distribution. Although these did not exhibit vortices, I found that:

- The ambient plasma flows away from the DFB along the XY projection of the DF normal direction with a duskward component caused by diamagnetic drift. When the diamagnetic effect is subtracted, the flow has a prominent dawnward component to the DFB's duskside.

From my statistical maps I also found the following interesting phenomena:

- The vertical total pressure drops across the DF, indicating cross-tail current reduction immediately inside the DFB. The reduced cross-tail current may have been fed to the dipolarization front current sheet.

- The coordinate system determined by the direction of DFB motion usually aligns data better, suggesting that DFB motion controls the distributions of physical quantities.

4.3.1 The nature of pressure and flow distributions

The pressure buildup and flow diversion I observed are responses to DFB motion, which involves both fluid and kinetic effects. Buildups of the total pressure, radial total pressure, and thermal pressure all peak at the DFB's central azimuth and reduce toward larger azimuths. Such a pressure distribution is expected as a simple fluid effect from a moving object: the severest compression happens where the object's surface-normal direction is the same as its motion direction. Plasma flow radially away from the DFB is a signature of fluid pushed away by an impenetrable body. The pressure and flow distribution can also be understood kinetically, as a result of ambient particles being accelerated and reflected at the DF (*Zhou et al.*, 2011; *Xing et al.*, 2012). Stronger acceleration-reflection at the DF's duskside can explain the stronger thermal pressure and more prominent dawnward component of the quiet-time-average-removed flow to a DFB's duskside.

4.3.2 The factors controlling DFB motion

I have established that the radial total pressure $P_{\mathrm{ttl},r}$ controls DFB motion, which is mainly in the XY plane. From the DF layer $P_{\mathrm{ttl},r}$ exerts two pressure gradient forces—one away from the DFB to push the ambient plasma away radially and another tailward towards deep inside the DFB to decelerate it. If the tailward $P_{\mathrm{ttl},r}$ gradient force is larger/smaller than the magnetic curvature force, the DFB is accelerated tailward/earthward. We can roughly estimate the typical curvature force density f_c based on the *Harris* (1962) current sheet assumption:

$$f_{\mathrm{c},x} = -\frac{B_z dB_x}{\mu_0 dz} = -\frac{B_z B_{\mathrm{lobe}}}{\mu_0 l}\Big(1 - \tanh^2\frac{z - z_0}{l}\Big) = -\frac{B_z B_{\mathrm{lobe}}}{\mu_0 l}\Big(1 - \tanh^2\frac{B_x^2}{B_{\mathrm{lobe}}^2}\Big), \qquad (4.3)$$

where l is the cross-tail current sheet half thickness and z_0 is the neutral sheet location. Into Equation 4.3 I put the median values behind the DF: B_z =∼13 nT (Figure 4.2a), B_{lobe} =∼30 nT (Figure 4.2d), l =∼2 $\mathrm{R_E}$, and B_x =∼12 nT (see Section 5.2.4 for l and Section 2.2.1 for B_x). I get a typical curvature force density of ∼0.13 nPa/$\mathrm{R_E}$, comparable to the typical tailward $P_{\mathrm{ttl},r}$ gradient, ∼0.15 nPa/$\mathrm{R_E}$. Therefore, the pressure gradient force and curvature force at the DFB are statistically in approximate force balance in the 9-12 $\mathrm{R_E}$ downtail region where the dominant population of my event list dwells.

Section 3.3.2.1 displayed the statistical variations of the DFBs' plasma bulk velocity after they are generated at 20-30 $\mathrm{R_E}$ downtail (Figure 3.4b). From $X = -21$ to -15 $\mathrm{R_E}$, the DFBs' median earthward velocity v_x increases from 200 km/s to 300 km/s. If we assume that such a trend can represent the life history of an individual DFB, it indicates that tailward of $X = -15$ $\mathrm{R_E}$ the curvature force overcomes the pressure gradient force and accelerates the DFB earthward. From $X = -15$ to -6 $\mathrm{R_E}$, the median earthward velocity of the DFBs decreases from 300 km/s to 150 km/s. This trend suggests that the DFB motion gets braked by the larger pressure gradient force (this braking creates a dawnward inertial current inside the DFB which can contribute to the local cross-tail current reduction I have observed behind the DF). Based on Figure 3.4b we can roughly estimate the net force density

accelerating/decelerating the DFB (the left hand side of Equation 4.1)

$$f_{\mathrm{net},x} = \rho \frac{dv_x}{dt} = N m_{\mathrm{p}} v_x \frac{dv_x}{dx}, \tag{4.4}$$

where N is the plasma number density and m_{p} is the proton mass. Figure 2.2d the typical N inside the DFB is $\sim$0.3/cc. The aforementioned velocity dependence on downtail distance gives a typical v_x of 250 km/s and a dv_x/dx of $\sim$20 km/(s$\cdot$R$_{\mathrm{E}}$) (absolute value for both accelerating and decelerating phases). Through Equation 4.4 these values result in a net force density of $\sim$0.003 nPa/R$_{\mathrm{E}}$. This result is smaller than the $\sim$0.01 nPa/R$_{\mathrm{E}}$ estimate of *Shiokawa et al.* (1997) due to different event selection criteria. Compared with the typical pressure gradient and curvature force density of $\sim$0.15 nPa/R$_{\mathrm{E}}$, both net force density values (ours and that of *Shiokawa et al.* (1997)) suggest that the DFBs are indeed in approximate force balance; the tiny difference between the pressure gradient and curvature forces determines a DFB's acceleration.

Individual cases may deviate from the DFBs' statistical approximate force balance (e.g., *Li et al.*, 2011). Nevertheless, this approximate force balance condition provides confidence for my application of Equation 4.2 in evaluating the DFB-associated field-aligned currents.

4.3.3 The relationship between thermal pressure buildup and FACs

When coexisting with flux tube volume distribution near the DFB, my reconstructed equatorial thermal pressure (P_{eq}) distribution requires field-aligned currents to arise. My statistical map of P_{eq} is consistent with RCM simulations which associated such a distribution with FACs around the DFB based on Equation 4.2 (*Yang et al.*, 2011, 2012) (Although *Yang et al.* (2011, 2012) focus on stopping DFBs at geosynchronous orbit, whereas I focus on travelling DFBs mainly at 9-12 R$_{\mathrm{E}}$ downtail, the pressure distribution relative to the DFB is the same). Applicability of Equation 4.2 to the vicinity of the DF is limited by the DF's kinetic nature (e.g., *Runov et al.*, 2011); future kinetic models are necessary to fully understand FAC generation near the DF. Nevertheless, I use Equation 4.2 to roughly illustrate how the P_{eq} distribution demands both region-1 and -2-sense FACs (Figure 4.6). The P_{eq} gradient arrows

in Figure 4.6 have been directly transferred from the $P_{\rm eq}$ distribution in Figure 4.4: they have a radial component toward the DFB's outer boundary and an azimuthal component toward the meridian of the DFB's leading point. Next I derive the gradient of the unit-flux flux tube volume $V = \int \frac{ds}{B}$, which is another factor of Equation 4.2. Typically, magnetic field strength B minimizes at the DFB's outer boundary (see Figure 4.2b). We expect field line length s to increase from the ambient plasma (earthward of the DFB) towards the DFB's outer boundary and vary insignificantly over the thin DF. Therefore, the flux tube volume of unit magnetic flux, an integral of field line length over magnetic field strength, peaks at the DFB's outer boundary. This peak gives ∇V a radial component pointing from both sides of the DFB outer boundary towards it. In addition, ∇V also has a tailward gradient due to the general magnetotail field configuration in the absence of a DFB. The combination of radial and tailward components gives the ∇V directions I illustrated in Figure 4.6. The illustrated ∇V in the ambient plasma fills the $\sim$0.8 R_E region ahead of the DFB because the gradual drop in field strength from ahead of the DF toward the DFB's outer boundary typically persists for $\sim$40s (Figure 4.2b). The illustrated ∇V also fills the DF layer because the magnetic field continues to strengthen over the DF thickness. On the other hand, $\nabla P_{\rm eq}$ radially toward the DFB's outer boundary and azimuthally toward the DFB's central azimuth takes up the area from $\sim$1 R_E ahead of the DFB to $\sim$0.3 R_E (larger than the DF thickness) behind the DFB's outer boundary. According to Equation 4.2, the non-alignment $\nabla P_{\rm eq}$ and ∇V necessitates FACs into and out of the ionosphere, as illustrated in Figure 4.6. The resultant FACs are in region-2-sense in the $\sim$0.8-R_E-thick region immediately earthward of the DFB and in region-1-sense inside the DF layer.(Even if ∇V is unperturbed by the DFB and is tailward everywhere as that during quiet time, the resultant FACs' directions are still so.) The directions and locations of these FACs are the same as those inferred from magnetic field variations, as we shall see in Chapter 5 observed.

Both region-1 and -2-sense FACs can connect to Earth's ionosphere (e.g., *Yang et al.*, 2012). Region-1-sense FACs result in auroral poleward boundary intensification and streamers in the ionosphere (e.g., *Nakamura et al.*, 2001); Recent observations suggested the relationship between auroral forms and region-2-sense FACs (e.g., *Yao et al.*, 2013). The

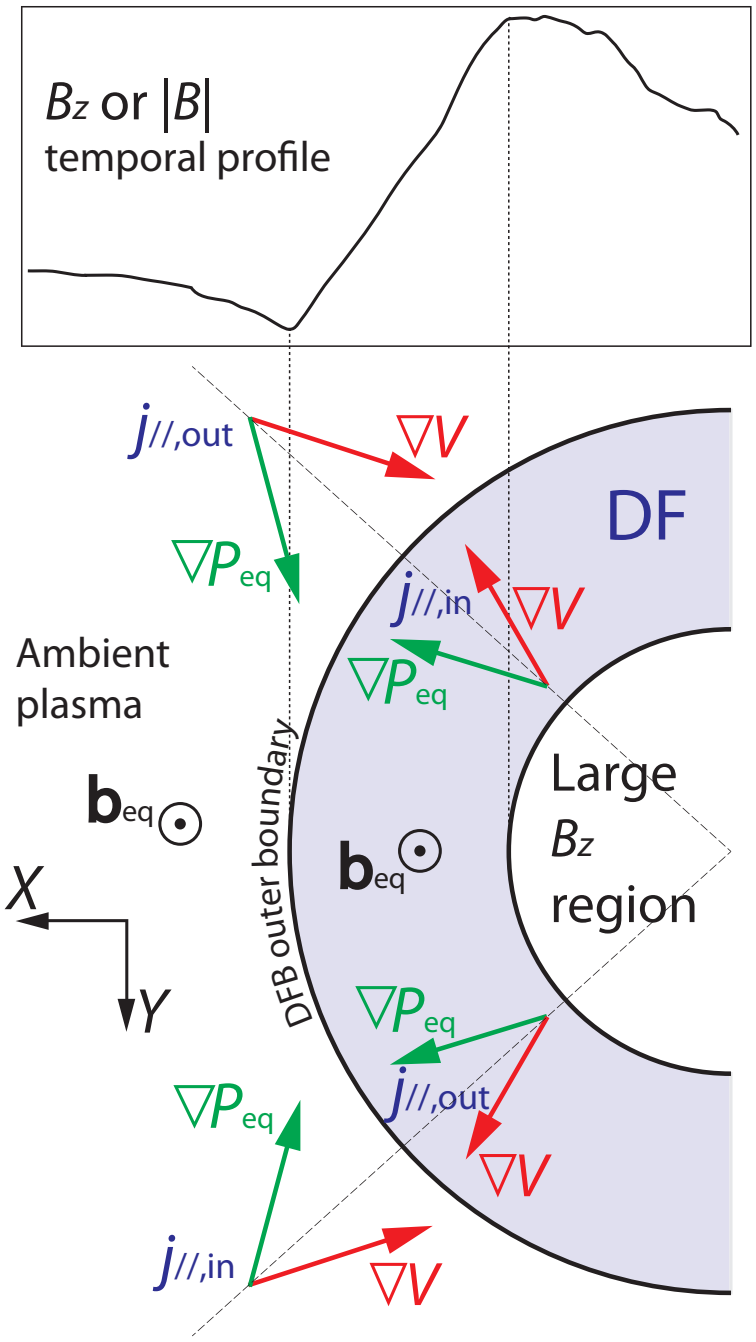

Figure 4.6: Field-aligned currents associated with equatorial thermal pressure buildup near the DFB. The top black curve shows the typical in-situ observation of a DFB. The lower part is an equatorial-cut cartoon of a DFB in which dipolarization front thickness (blue area) is exaggerated. Green arrows represent the gradient of equatorial thermal pressure; red arrows represent the gradient of unit-magnetic-flux flux tube volume. Note that the arrows do not represent the magnitudes of the gradients. The magnetic field has a component out of the plane. The configurations of gradients and magnetic field are consistent with FACs towards ($j_{\parallel,\mathrm{in}}$) and out of ($j_{\parallel,\mathrm{in}}$) the ionosphere.

region-1-sense FACs also connect to the cross-tail current to complete a current loop; this closure contributes to the cross-tail current reduction behind the DF. Region-2-sense FACs may connect to the duskward dipolarization front current (which contains the region-1-sense FACs as a component, see Chapter 5) to complete its loop (*Yang et al.*, 2012; *Birn et al.*, 1999).

The DFB's FAC pair is in similar configuration to the two-loop substorm current wedge model (e.g., *Sergeev et al.*, 2011) which also consists of a region-1-sense loop and another region-2-sense loop earthward of the region-1-sense loop. According to my results, both the DFB's region-1 and -2-sense FACs can come from thermal pressure buildup caused by fluid compression and/or kinetic reflection from DFB motion. Therefore, unlike a SCW which always emerges near geosynchronous orbit, a DFB's FACs can emerge independent of downtail location: as long as a DFB moves, it creates pressure and flux tube volume gradients that require FAC generation. The FACs are "supported" by the DFB motion. The FACs thus travel earthward with DFBs and result in equatorward-streaming auroral signatures in the ionosphere. When the DFBs finally reach the inner magnetosphere, the coalescence of several DFB-caused pressure buildups may lead to a substorm current wedge.

In Chapter 5, I continue to investigate the DFB-associated FACs.

CHAPTER 5

The current system of the dipolarizing flux bundle

In this chapter I infer the current system of the dipolarizing flux bundle from magnetic field measurements, using the leading DFB list I built in Section 2.2.1 and its subsets. The magnetic field perturbations caused by a DFB are consistent with local field-aligned current generation of region-2 sense ahead of the front and region-1 sense at the dipolarization front. The median thickness of the dipolarization front current sheet (DFCS) increases from 800 to 2000 km with increasing distance from the neutral sheet, indicating bundle compression near the neutral sheet. On a sagittal cross section, DFCS's linear current density (1.2-1.8 nA/m) peaks $\sim \pm 0.55l$ from the neutral sheet (where l is the ambient cross-tail current sheet half-thickness, $l \sim 1.5$ R_E in my database). This peak, reminiscent of active-time cross-tail current sheet bifurcation noted in past studies, suggests that the intense but thin DFCS (10 to 20 nA/m^2) may be produced by redistribution (diversion) of the extended but weaker cross-tail current ($\sim$ 1 nA/m^2). Near the neutral sheet, the average DFCS current over the dipolarization front (DF) thickness is perpendicular to both the magnetic field interior to the DFB and the average field direction over the DF thickness. Away from the neutral sheet, the average current becomes progressively parallel to the internal field and the average field direction. The average current directions are indicative of region-1-sense field-aligned current on the DF. As few as approximately three DFBs can carry sufficient total current that, if redirected into the auroral ionosphere, can account for the substorm current wedge's peak current for a sizable substorm ($\sim$ 1 MA). A collapsing DFB could thus be an elemental substorm current wedge, or "wedgelet", that can divert a sizable portion of the cross-tail current into the auroral ionosphere.

5.1 Introduction

Small-amplitude, negative B_z variations (dips) often precede dipolarizing flux bundles (*Ohtani et al.*, 2004; *Runov et al.*, 2011). These have been explained as the magnetic field rotation or bending expected in the flux rope model (*Zong et al.*, 2004) or the NFTE model (*Sergeev et al.*, 1992) of DFBs. The B_z dip can also be explained as the result of fringing fields from a finite-size, vertical sheet current. With or without a dip, the sharp magnetic field jump at the dipolarization front is indicative of a concentrated, thin, approximately one-dimensional current layer flowing on the DF. We call this current layer the dipolarization front current sheet (DFCS).

As I found in Section 2.3, the DF and thus the DFCS has a saddle like spatial profile. We have discussed how such spatial profile influence the DFB's magnetic field variations and its modifications to ambient plasma in section 2.3.3.

Another factor controlling the DFB magnetic field is the electric current direction in the DFCS. The strong B_z of an earthward propagating DFB is most likely produced by a duskward current along the DF. *Schmid et al.* (2011) showed that this is true for most DFs and confirmed statistically the results of earlier case and multicase studies regarding the current's predominant orientation perpendicular to the internal field (*Runov et al.*, 2011; *Runov et al.*, 2011). On the other hand, DFBs may also be accompanied by field-aligned currents (FACs). *Chen and Wolf* (1993) suggested that the cross-tail currents at the morning and evening sides of the plasma bubble feed field-aligned currents (FACs) that connect the bubble to the ionosphere. MHD simulations affirmed this scenario by showing that both region-1-sense and region-2-sense FACs can be generated by flow shears and vortexes associated with an earthward moving DFB (*Birn et al.*, 1999, 2004a). Here region-1 and -2 sense stand for FAC direction combinations: region-1 (-2) sense means toward (away from) Earth on the DFB's morning side and away from (toward) Earth on the DFB's evening side. Chapter 4 and multi-fluid simulations by *Yang et al.* (2011, 2012) showed that DFB motion can result in pressure gradients that can also account for region-1 and -2-sense FACs. In their simulations, the region-1-sense FACs connect to the ionosphere and create polar

boundary intensifications (PBIs) (e.g., *Zesta et al.*, 2002) and north-south arcs (streamers) (e.g., *Nakamura et al.*, 2001), whereas the region-2-sense FACs connect the ionosphere with the partial ring current, which is enhanced by the DF's duskward current. However, to fully understand the relationship between the DF current and the FACs, more observational investigations are needed.

The DFB-related FACs implies a close relationship between DFBs and the substorm current wedge (SCW) (*McPherron et al.*, 1973). Dipolarizing flux bundles are localized within 1 to 3 R_E in the cross-tail direction (e.g., *Sergeev et al.*, 1996, and section 2.3.2.3), whereas the SCW typically occupies several hours of magnetic local time (MLT). Moreover, DFBs typically propagate earthward, whereas SCWs "expand" outward (see, e.g., *Jacquey et al.*, 1993). Further investigations, such as comparing the DFCS strength with the SCW strength, are needed to clarify the DFB-SCW relationship.

Dipolarization front current sheet thickness (the dipolarization front is entirely filled by the DFCS, and the DFCS thickness is thus also the DF thickness), density, and strength are important for understanding the evolution of the dipolarizing flux bundle structure as it propagates across large distances in the magnetotail, as well as for understanding local magnetic field dynamics and global magnetotail current system modification. *Runov et al.* (2009, 2011) estimated the DFCS to be as thin as $\sim$ 1000 km (on the order of one to a few ion inertial lengths) and its current density to be about 50 to 100 nA/m^2 (several times the cross-tail current density). The thinness of the front results in a finite ion gyroradius effect separating ions and electrons; this effect decouples the ions from the field lines.

To date, the three-dimensional nature of the DFB current system has not been explored comprehensively. My following statistical survey of DFB current directions and strength by using a large number of events could help elucidate the origin and importance of DFB currents to global magnetospheric current systems.

5.2 Results and Interpretations

In this section I first investigate the direction and strength of the dipolarizing flux bundle's current system. Then I examine what change the DFB current system bring to the cross-tail current. In each subsection I first report the result and then discuss what the result means.

5.2.1 Region-2 and -1-sense field-aligned currents

As suggested by section 4.3.3, thermal pressure distribution requires the existence of region-2-sense field-aligned currents in the $\sim$ 1 R_E region ahead of the DFB and region-1-sense FACs inside the DF layer. To confirm their existence, I examine the B_y variations around the DFB.

5.2.1.1 Results

For the examination of B_y variations in Figure 5.1, I split the database into four quadrants depending on crossing location: evening or morning side, as previously done based on the sign of n_y (excluding near-zero events), and north or south of the neutral sheet, based on the value of $B_{qx}/B_{lobe,q} > 0.3$ or < -0.3. For simplicity, in Figure 5.1, I only show the result from the $\mathbf{B}_{in} \times \mathbf{B}_{out}$ DF-normal determination method (other methods give similar results, although, again, the $\mathbf{B}_{in} \times \mathbf{B}_{out}$ method organizes my data best). The B_y perturbation relative to the quiet time pre-DFB average is positive immediately ahead of the approaching DF ($\delta B_y > 0$) on the evening-south (Figure 5.1b) and morning-north (Figure 5.1c) regions and negative ($\delta B_y < 0$) in the other two quadrants (Figures 5.1a and 5.1d).

Behind the DF, δB_y sharply reverses its pre-DF trend in all four quadrants, suggesting that the DFCS current system plays a role in generating these B_y perturbations. To examine this effect further, I detrend the B_y profiles by removing the quiet-time ($t_0 - 3$ min to $t_0 - 2$ min) averages. The rationale for the detrending is that the quiet-time average may be due to biases introduced by interplanetary magnetic field penetration into the magnetosphere or the magnetotail's local activity history. Figures 5.1e-5.1h show the results after detrending:

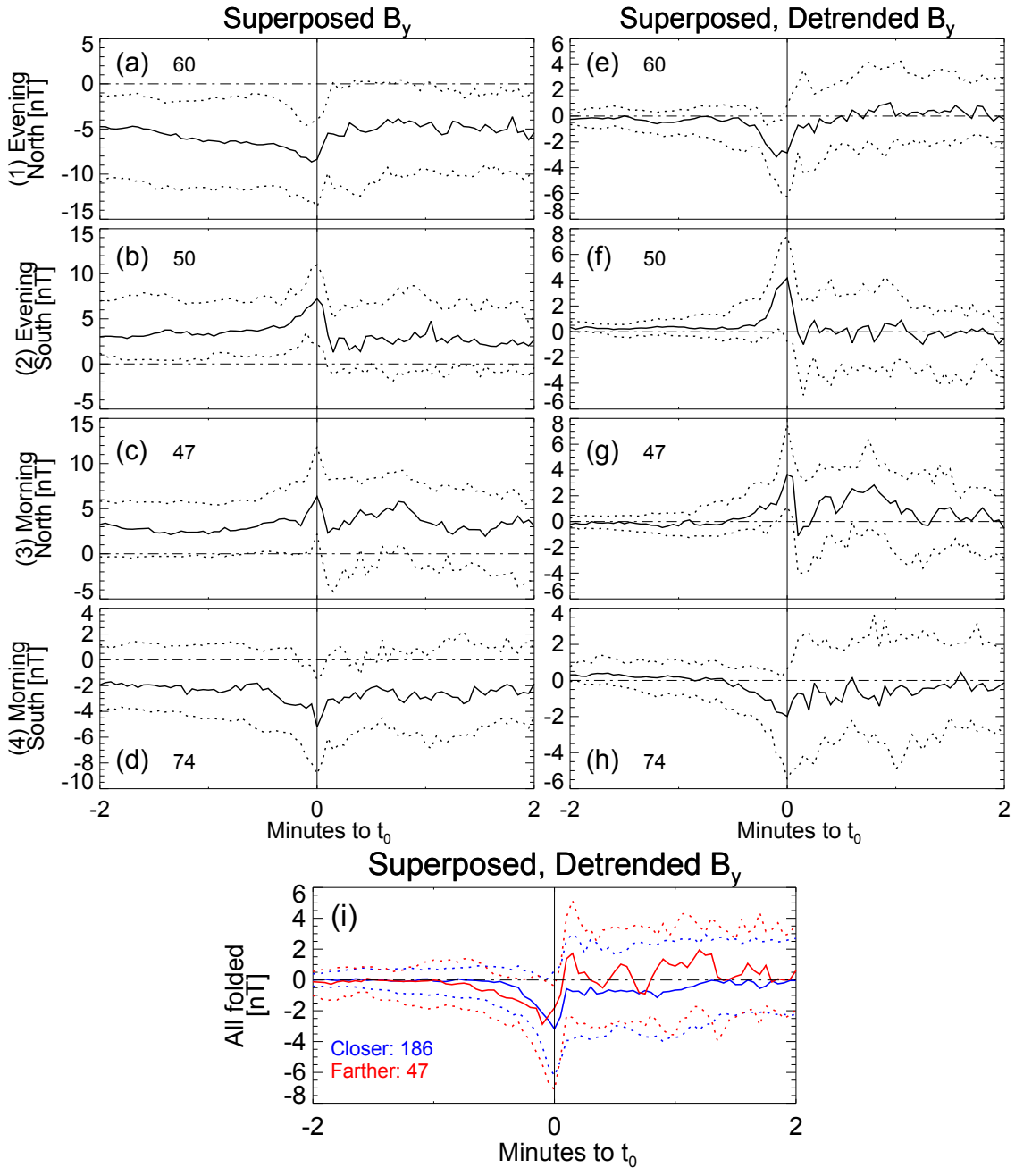
Superposed B_y
Superposed, Detrended B_y
(1) Evening North [nT]
(2) Evening South [nT]
(3) Morning North [nT]
(4) Morning South [nT]
(a) 60
(b) 50
(c) 47
(d) 74
(e) 60
(f) 50
(g) 47
(h) 74
Minutes to t_0
Minutes to t_0
Superposed, Detrended B_y
(i)
All folded [nT]
Closer: 186
Farther: 47
Minutes to t_0

δB_y perturbations are very gradual about 1 min prior to DF arrival, become significant about 30 s prior to DF arrival, and are completely eradicated in $\sim$ 7 s along with DF passage. The current signatures inferred from these unipolar δB_y variations are consistent with a pair of field-aligned current sheets in each quadrant. These two current sheets, which are stationary in the frame of the DFB, correspond to a region-1-sense field-aligned current system immediately at the DF (since the δB_y return align with the B_z sharp increase in Figures 2.2a and 2.2i) and a region-2-sense FAC system ahead of (earthward of) the DF.

We can roughly estimate the thickness and intensity of these two sheet current systems. My events' average propagation speed in the DF normal direction is $\sim$ 170km/s. The $\sim$ 30 s, $\sim$ 4 nT δB_y deviation ahead of the DF (Figures 5.1e-5.1h) corresponds to a $\sim$ 0.8 R_E thick region-2-sense current system with a density of $\sim$ 0.6 nA/m^2. The $\sim$ 7 s δB_y sharp returns in Figures 5.1e-5.1h are also $\sim$ 4 nT; they correspond to $\sim$ 1200 km thick and $\sim$ 4 nA/m^2 dense region-1-sense current. In Figures 5.1e-5.1h, the δB_y deviation and return have the same magnitude; thus, in general the region-2 and -1-sense current sheets contain approximately the same amount of current. Since the database is dominated by observations taken not far from the neutral sheet, this is a behavior characteristic of the relatively near-neutral-sheet portion of the dipolarization front current system. We also examined this for the subset of fronts that are detected further away from the neutral sheet ($|B_{qx}/B_{lobe,q}| > 0.6$, red traces in Figure 5.1i). For those events, the δB_y return at the front (even overshooting pre-DF value) is much larger than its deflection ahead of the front. Thus, the region-1-sense sheet

Figure 5.1 *(preceding page)*: Superposed epoch analysis of (a-d) B_y and (e-l) detrended δB_y for $\mathbf{B}_{in} \times \mathbf{B}_{out}$, earthward-normal dipolarization front events. The curves in each panel are the upper quartile (dotted), median (solid), and lower quartile (dotted) of the superposed data. "Morning" stands for $n_y < -0.2$ in Figures 5.1c, 5.1d, 5.1g, and 5.1h; "Evening" stands for $n_y > 0.2$ in Figures 5.1a, 5.1b, 5.1e, and 5.1f. "North" (of the neutral sheet) stands for $B_{qx}/B_{lobe,q} > 0.3$ in Figures 5.1a, 5.1c, 5.1e, and 5.1g; "South" (of the neutral sheet) stands for $B_{qx}/B_{lobe,q} < -0.3$ in Figures 5.1b, 5.1d, 5.1f, and 5.1h. The number in each of Figures 5.1a-5.1h is the total number of events used in that figure. In Figure 5.1i, I compare the result for the 47 events far from the neutral sheet ($|B_{qx}/B_{lobe,q}| > 0.6$, red quartiles) with that for the 186 events closer to the neutral sheet ($0.3 < |B_{qx}/B_{lobe,q}| < 0.6$, blue quartiles). We have folded the four regions in Figures 5.1e-5.1h into one (by inverting data in evening-south and morning-north groups) for conciseness.

contains significantly more current than the region-2-sense sheet. A comparison between δB_y perturbations at large and at relatively small (Figure 5.1i, blue traces) distances from the neutral sheet reveals that the region-1-sense current increases by a factor of two at large distances, whereas the region-2-sense current remains the same in magnitude (but appears earlier).

5.2.1.2 Interpretation and Discussion

Current systems similar to the inferred region-1 and -2-sense FACs have been modeled by fluid simulations (*Birn et al.*, 1999, 2004a; *Yang et al.*, 2011, 2012). They are also required by thermal pressure buildup caused by the DFB (see Section 4.3.3). From Figure 5.1, we see that the current system type can be identified directly from field line deflection. In most previous studies, FACs emerge when DFBs are slowing down or have reached geosynchronous orbit. The events in Figure 5.1, however, are mostly distributed around ~ 10 R_E downtail. Thus, my observations reveal that FACs may exist in the DFB's traveling stage, and, notably, that the region-2-sense system may be generated ~ 0.8-R_E ahead of (earthward of) the DFB rather than at the partial ring current near geosynchronous orbit. These two current systems, which may be related to the substorm current wedge (e.g., *Yao et al.*, 2012), deserve more investigations. In the next section, I further examine the spatial distribution of the DFCS current system and, in particular, its direction.

5.2.2 The DFCS current direction

5.2.2.1 Results

We infer the current direction relative to the magnetic field direction immediately behind the DF by comparing the maximum magnetic field variance direction $\mathbf{L}$ during a DF crossing with the direction of $\mathbf{B}_{\text{in}}$. The DFCS current $\mathbf{j}$ is always perpendicular to $\mathbf{L}$ and parallel to DF plane, the plane that contains both $\mathbf{L}$ and $\mathbf{B}_{\text{in}}$ (this is the basis of the $\mathbf{B}_{\text{in}} \times \mathbf{L}$ DF-normal determination; see Appendix A for details). Here $\mathbf{j}$ represents the average current over the DF thickness, since $\mathbf{L}$ is obtained from MVAB (MVA on magnetic field data) applied across

the DF (when I refer to the "average current" over the DF thickness, "average" means in an average sense, not the arithmetic mean which "average" stands for in all other occasions). From the two opposite choices for the direction of **L** given by MVAB, I select the one that makes an increase of the field along the **L**-direction upon entry into the DFB. Consistent with the DF selection criteria (keyed on the increase in B_z), **L** has a northward component for 1317 of the 1326 events that have a maximum-to-intermediate variance eigenvalue ratio greater than 3 (meet the "good **L**" requirement; see Appendix B for more details). For the other nine events, the minimum variance analysis was overwhelmed by B_x or B_y fluctuations and failed to reflect the B_z jump. An increase in the field along the **L**-direction upon DFB entry means that the inferred average current density **j** is oriented 90° clockwise from **L** when viewed from outside the DFB. For an earthward-normal DFB with **L** pointing northward, this gives a current with a duskward component, consistent with expectations. When $\mathbf{B}_{\rm in}$ and **L** are in the same direction, $\mathbf{B}_{\rm in}$ is in the same direction as the magnetic field perturbation generated by **j**, and **j** is perpendicular to $\mathbf{B}_{\rm in}$. This perpendicular current is expected from case studies and has shown statistically to be the case near the equatorial plane, (e.g., *Schmid et al.*, 2011). When the angle between $\mathbf{B}_{\rm in}$ and **L**, $\theta_{\mathbf{B}_{\rm in}\text{-}\mathbf{L}}$, deviates from zero, the magnetic field perturbation from **j** has a component across the internal field $\mathbf{B}_{\rm in}$, and there is a DFCS current component aligned with $\mathbf{B}_{\rm in}$. When $\mathbf{B}_{\rm in}$ and **L** are purely orthogonal, **j** is either parallel or antiparallel to $\mathbf{B}_{\rm in}$.

In Figure 5.2a, I show the distribution of the absolute value of the angle between $\mathbf{B}_{\rm in}$ and **L**, $|\theta_{\mathbf{B}_{\rm in}\text{-}\mathbf{L}}|$, at various distances from the neutral sheet. Here I include both earthward-normal and tailward-normal DFs (the results hold for the two categories separately as well), as this simple, robust result is independent of DF-normal direction (and the associated event loss from various goodness conditions on normal determination). For all distances (black line), most events' $|\theta_{\mathbf{B}_{\rm in}\text{-}\mathbf{L}}|$ is rather small, so the DFCS current direction is most often perpendicular to the internal field $\mathbf{B}_{\rm in}$ ($\mathbf{B}_{\rm in}$ is mostly northward, so the current flows duskward). This is consistent with previous results from multipoint observations (*Schmid et al.*, 2011).

As the distance from the neutral sheet increases (larger $B_{{\rm q}x}/B_{\rm lobe,q}$, colored lines in Figure

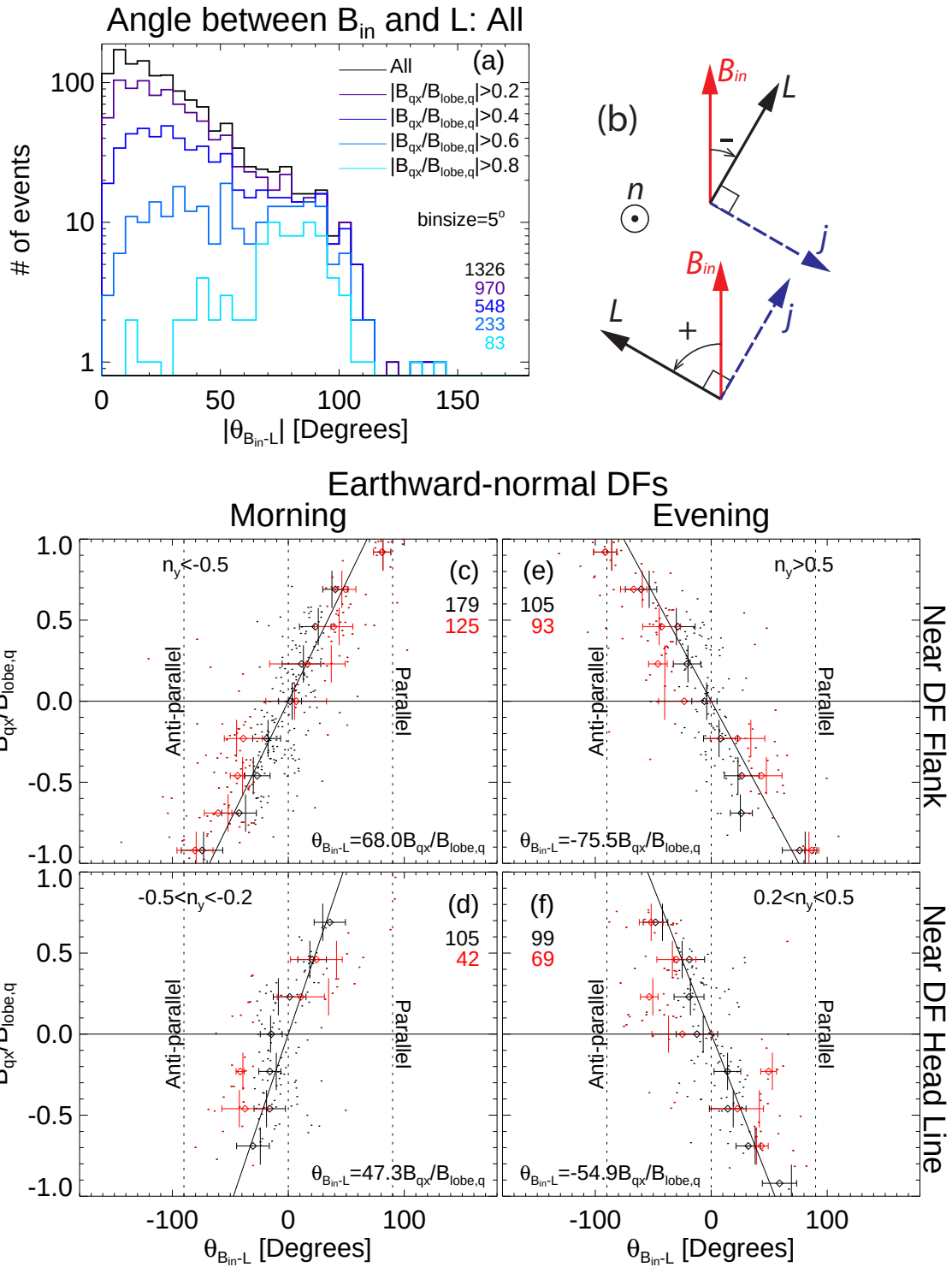
Angle between B_in and L: All
(a)
All
|B_qx/B_lobe,q|>0.2
|B_qx/B_lobe,q|>0.4
|B_qx/B_lobe,q|>0.6
|B_qx/B_lobe,q|>0.8
binsize=5°
1326
970
548
233
83
# of events
|θ_Bin-L| [Degrees]
(b)
B_in
L
n
j
+
−
Earthward-normal DFs
Morning
Evening
Near DF Flank
Near DF Head Line
(c)
(d)
(e)
(f)
n_y<-0.5
-0.5<n_y<-0.2
n_y>0.5
0.2<n_y<0.5
179
125
105
42
105
93
99
69
Anti-parallel
Parallel
B_qx/B_lobe,q
θ_Bin-L=68.0B_qx/B_lobe,q
θ_Bin-L=47.3B_qx/B_lobe,q
θ_Bin-L=-75.5B_qx/B_lobe,q
θ_Bin-L=-54.9B_qx/B_lobe,q
θ_Bin-L [Degrees]

5.2a), a progressively larger portion of events have a $\theta_{\mathbf{B}_{\rm in}\text{-}\mathbf{L}}$ angle close to 90°, indicating a progressively more $\mathbf{B}_{\rm in}$-aligned DFCS current. By $B_{{\rm q}x}/B_{\rm lobe,q} > 0.8$ (cyan line), i.e., when DFBs are observed to start when the probe resides in the ambient outer plasma sheet, DFCSs exhibit currents nearly aligned with $\mathbf{B}_{\rm in}$. We also separated events according to their distance from Earth (not shown) but found no clear difference in the $\theta_{\mathbf{B}_{\rm in}\text{-}\mathbf{L}}$ distribution for various event groups; my study cannot validate the hypothesis that DFCS-related FACs are most prominent as the DFBs slow down in their near-Earth final stages (e.g., *Chen and Wolf*, 1993; *Birn et al.*, 2004a). Observations from a larger database over a greater distance, extending from the plasma sheet inner edge ($X =\sim -6$ $\rm R_E$) to the putative DFB source region ($X = -20 \sim -30$ $\rm R_E$), are required to study the effects of DFB braking.

To further investigate the sense of the DFCS's $\mathbf{B}_{in}$-aligned components (parallel or anti-parallel to $\mathbf{B}_{\rm in}$) and their dependence on the side of the neutral sheet (north or south) as well as the azimuthal distance from the DF's head line, I use the following convention for the sign of the angle from $\mathbf{B}_{\rm in}$ to $\mathbf{L}$ ($\theta_{\mathbf{B}_{\rm in}\text{-}\mathbf{L}}$). Viewed from the front-normal side (n out of the plane),

---

Figure 5.2 *(preceding page)*: (a) The histogram distributions of the absolute value of the angle between $\mathbf{B}_{\rm in}$ and $\mathbf{L}$, $\theta_{\mathbf{B}_{\rm in}\text{-}\mathbf{L}}$ for events at various distances from the neutral sheet (denoted by lines of different colors). The distribution includes all events that meet the good $\mathbf{B}_{\rm in}$ and $\mathbf{L}$ requirements described in Appendix B. Event numbers in each histogram (denoted by the histogram color) are also inserted in the figure. (b) The definition of $\theta_{\mathbf{B}_{\rm in}\text{-}\mathbf{L}}$ as viewed from outside the DFB ($\mathbf{n}$ out of the plane). (c-f) The dependence of $\theta_{\mathbf{B}_{\rm in}\text{-}\mathbf{L}}$ on the distance from the neutral sheet ($B_{{\rm q}x}/B_{\rm lobe,q}$ as proxy) at different azimuthal locations on the curved front (from morning flank through front head to evening flank, as determined by n_y). Normal directions were determined using the $\mathbf{B}_{\rm in} \times \mathbf{L}$ method. Red dots represent events that meet the good angle requirement for normal determination ($30° < \theta_{\mathbf{B}_{\rm in}\text{-}\mathbf{L}} < 150°$, see Appendix B); black dots represent those that do not ($\theta_{\mathbf{B}_{\rm in}\text{-}\mathbf{L}} < 30°$ or $\theta_{\mathbf{B}_{\rm in}\text{-}\mathbf{L}} > 150°$). All events meet the "good $\mathbf{L}$" and "good $\mathbf{B}_{\rm in}$" requirements. The events represented by black dots were determined to be earthward-normal DFs. Vertical bars/diamonds represent each bin's median/average. Horizontal error bars on top of the diamonds are each bin's standard deviation. Black medians/averages are the medians/averages of all the events (both black and red dots) in that bin; red medians/averages are the medians/averages of the red dots only. We calculate medians and averages only for bins with no less than three events. The numbers in black/red are the numbers of black/red dots (events). The straight line shown in each panel is the linear least squares fit to the $\theta_{\mathbf{B}_{\rm in}\text{-}\mathbf{L}}$ dependence on $B_{{\rm q}x}/B_{\rm lobe,q}$ (forced to pass through the origin) for all events in that panel. At the bottom of each panel, I show the fit result.

$\theta_{\mathbf{B}_{\rm in}\text{-}\mathbf{L}}$ is positive (or negative) when $\mathbf{L}$ rotates counter-clockwise (or clockwise) relative to $\mathbf{B}_{\rm in}$ (see schematic in Figure 5.2b). $\theta_{\mathbf{B}_{\rm in}\text{-}\mathbf{L}}$ of $+90°/-90°$ represents currents parallel/anti-parallel to $\mathbf{B}_{\rm in}$. Figures 5.2c-5.2f show the (signed) $\theta_{\mathbf{B}_{\rm in}\text{-}\mathbf{L}}$ dependence on the distance from the neutral sheet and the azimuthal distance of the DF crossing relative to the DF's head line. We used the $\mathbf{B}_{\rm in} \times \mathbf{L}$ method to determine the DFCS normal direction because $\mathbf{j}$ is flowing on the DF plane determined by $\mathbf{B}_{\rm in}$ and $\mathbf{L}$. In each panel, averages and medians for all events have the same trends as the averages and medians for events with well-defined normal direction (red dots). At the morning side of the DFB ($n_y < 0$, Figures 5.2c and 5.2d), medians and averages of $\theta_{\mathbf{B}_{\rm in}\text{-}\mathbf{L}}$ progressively move away from their near-neutral-sheet values of 0° and approach +90° northward of the neutral sheet and −90° southward of it. Thus, DFCS currents become progressively parallel/anti-parallel to $\mathbf{B}_{\rm in}$ northward/southward of the neutral sheet on the morning side of the DFB. On the evening side ($n_y > 0$, Figures 5.2e and 5.2f), the trend is reversed in sign, such that parallel/anti-parallel (to $\mathbf{B}_{\rm in}$) currents are the limiting cases for the southern-most/northern-most distances. Since B_x,in has the same sign as $B_{{\rm q}x}$ 94% of the time (as discussed in section 3), the DFCS $\mathbf{B}_{\rm in}$-aligned component $\mathbf{j}_{\parallel\text{-}\mathbf{B}_{\rm in}}$ is earthward/tailward on the DF's morning/ evening part. Based on the aforementioned relative directions between $\mathbf{j}$ and $\mathbf{B}_{\rm in}$ and the inferred $\mathbf{j}_{\parallel\text{-}\mathbf{B}_{\rm in}}$ direction relative to Earth, I refer to the relationship between $\mathbf{j}$ and $\mathbf{B}_{\rm in}$ as a region-1-sense relationship.

Linear fits to $\theta_{\mathbf{B}_{\rm in}\text{-}\mathbf{L}}$'s dependence on height for crossings nearer the DF's head line ($0.2 < |n_y| < 0.5$, Figures 5.2d and 5.2f) reveal smaller slopes than the linear fit for events near the DF's flanks ($|n_y| > 0.5$, Figures 5.2c and 5.2e). Thus, $\mathbf{j}_{\parallel\text{-}\mathbf{B}_{\rm in}}$ is more prominent near the DF's flanks. Here I have avoided using $|n_y| < 0.2$ events. When $|n_y|$ is small, even small errors from the normal determination may result in some morning or evening side events being falsely included in the opposite category, reducing and even canceling the signal in the linear fit.

To view the evolution of field and currents with height and azimuth relative to the DF's head line, I show the relative directions of the unit vectors along $\mathbf{B}_{\rm in}$, $\mathbf{L}$, and $\mathbf{j}$ on an "unfolded DF" in Figure 5.3. "Up" in each plane (vector triplet) in Figure 5.3a is the internal field $\mathbf{B}_{\rm in}$ direction, so the planar projections use "local-magnetic" coordinates. The

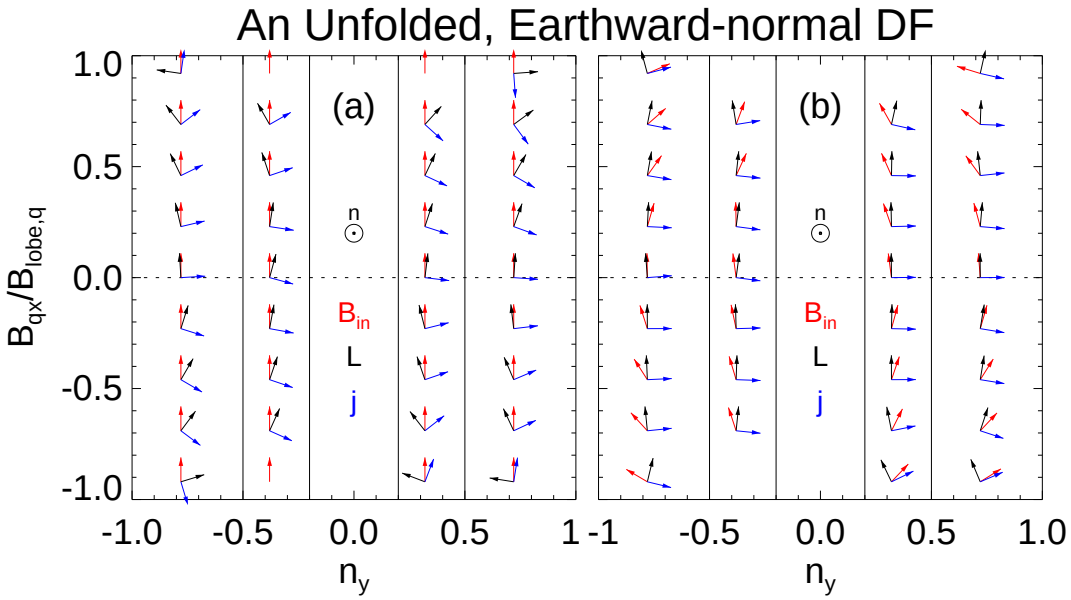

Figure 5.3: $\mathbf{B}_{\rm in}$, $\mathbf{L}$ and $\mathbf{j}$ relative directions inferred from the black vertical bars (median $\theta_{\mathbf{B}_{\rm in}\text{-}\mathbf{L}}$ values) in Figures 5.2c-5.2f. The directions are normally projected onto the plane tangent to the dipolarization front. Each vector triad, representing one such local planar projection, corresponds to one neutral-sheet distance bin in one of the four azimuths (four vertical regions) relative to the front head line (each vertical region corresponding to each of the four panels, i.e., Figures 5.2c-5.2f, according to n_y). The three vector planar projections are done in two different ways: (a) The projection is such that "up" is defined as the direction of $\mathbf{B}_{\rm in}$. (b) The projection is global magnetic, such that "up" on the tangent plane is the direction of Z projected on the tangent plane. The red vectors in Figure 5.3b are the directions of the median Bin (of the corresponding events and regions in Figures 5.2c-5.2f).

evolution of the current systems relative to the locally measured internal field is evident in Figure 5.3a: the currents become increasingly parallel or anti-parallel to $\mathbf{B}_{\text{in}}$ (in a region-1 sense) moving away from the equator and closer to the plasma sheet boundary. Figure 5.3b provides a slightly different view. "Up" is the projection of Z on each local DF-tangent plane, so all planar projections use "globalmagnetic" coordinates. In that panel, the "up" direction is fixed, thus revealing not only the current evolution with height but also the projected internal field-line orientation's evolution with height. As they move away from the equator near the DF's flanks, $\mathbf{B}_{\text{in}}$ field lines become more horizontal, and the currents retain their parallel or anti-parallel orientation to $\mathbf{B}_{\text{in}}$ in region-1 sense. In Figure 5.3b, average current $\mathbf{j}$ is predominantly horizontal in all bins, as the maximum variance vector $\mathbf{L}$ is predominantly along the Z projection direction on DF. This result is not due to a bias from my DF selection criteria based on sharp B_z changes. The DF tangent plane is often at a large angle to the Z axis, such that Z is far from $\mathbf{L}$ direction—even though the Z vector's projection ("up" direction) is close to the $\mathbf{L}$ vector on the tangent plane (see Appendix D.1 for further discussion).

The investigations above refer to the DFCS current's (in an average sense over the DF thickness) direction relative to $\mathbf{B}_{\text{in}}$, rather than the usually mentioned field-aligned or perpendicular current, a concept describing the local current direction's relationship to the magnetic field at the same point. However, the region-1-sense relationship between $\mathbf{j}$ and $\mathbf{B}_{\text{in}}$ is indicative of a region-1-sense field-aligned current component on the DF, consistent with the current type inferred from $|B_y|$ drops in section 5.2.1. To strengthen my argument, in appendix D.2, I compare $\mathbf{L}$ with the average magnetic field $\langle\mathbf{B}\rangle$ and the average field direction $\langle\mathbf{b}\rangle$ over the DF thickness. The results are qualitatively the same as those of Figures 5.2 and 5.3: $\mathbf{j}$ is in region-1-sense relationships with both $\langle\mathbf{B}\rangle$ and $\langle\mathbf{b}\rangle$. The results in appendix D.2 also show that $\mathbf{j}$ is more aligned with $\langle\mathbf{B}\rangle$ and $\langle\mathbf{b}\rangle$ than with $\mathbf{B}_{\text{in}}$.

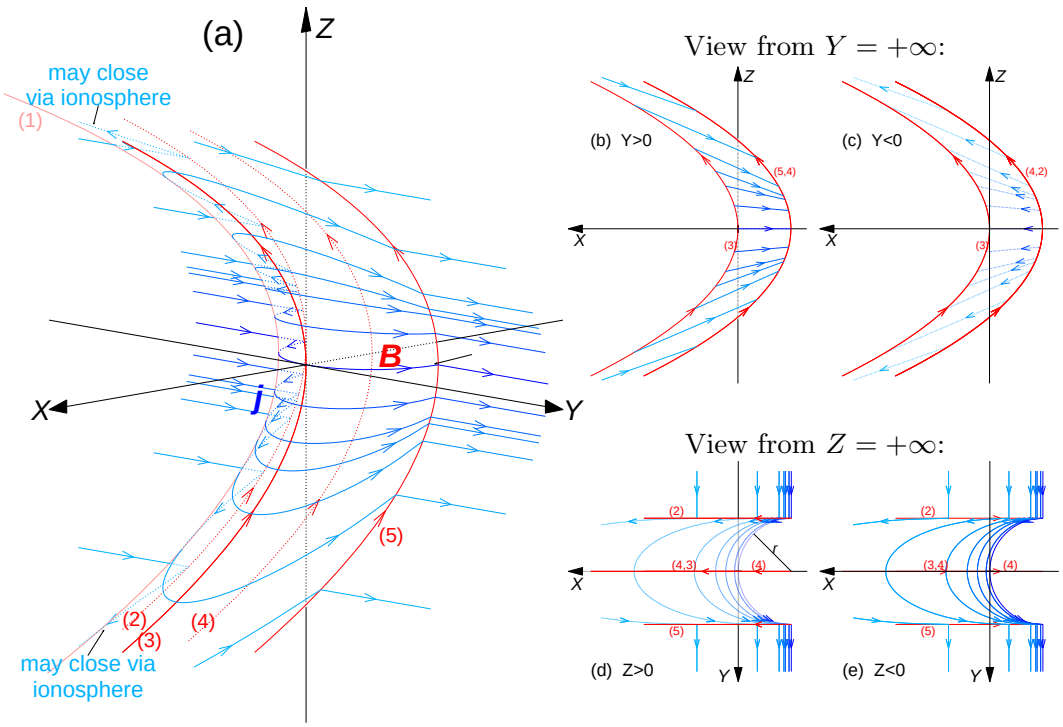

Figure 5.4: Illustration of a dipolarization front current sheet. In this figure, I have translated the GSM coordinate system to originate at the dipolarization front's head point at the neutral sheet. Magnetic field lines are in red; blue lines are the currents of the dipolarization front current sheet. (a) The 3-D view of the DFB and DFCS. Curve 1 separates the visible from the invisible parts of the 3-D structure. The field lines' (lines 2-5) footprints at the $Z = 0$ plane are (in $[X, Y]$): 2: $[-r, -r]$; 3: $[0, 0]$; 4: $[-r, 0]$; 5: $[-r, r]$, r being the radius of the semicircular current in the $Z = 0$ plane. In this ideal case, field line 3 is also this DF's head line, and the $Y = 0$ plane is this DF's midsagittal plane. Figures 5.4b and 5.4c are views of the 3-D structure's $Y > 0$ and $Y < 0$ parts (evening and morning parts) seen from $Y = +1$. Figures 5.4d and 5.4e are views of the 3-D structure's $Z > 0$ and $Z < 0$ parts (north and south parts) seen from $Z = +1$.

5.2.2.2 Interpretations and Discussions

In Figure 5.4, I illustrate the DFCS current directions on a saddle-shaped DF (here I draw an ideal case: the DFB is symmetric about the neutral sheet and has a head line parallel to the XZ plane), supposing $\mathbf{j}$ (the average current over the DF thickness) can largely represent the general behavior of the currents on the DFCS. We note that the current system near the DF can be very complicated in reality; Figure 5.4 is an oversimplification.

As illustrated in Figure 5.4, the duskward DFCS currents become increasingly aligned with the magnetic field ($\mathbf{B}_{\text{in}}$, $\langle\mathbf{B}\rangle$, or $\langle\mathbf{b}\rangle$; they represent the general field directions on the

DF) in a region-1 sense farther away from the neutral sheet and towards the DF's flanks. We drew the DF's transverse section as a semicircle in Figure 5.4 , but in reality, the DF's flanks (large $|n_y|$ region) where the field-aligned currents are prominent, may be elongated (e.g., *Nakamura et al.*, 2001; *Yang et al.*, 2012). Far from the neutral sheet, the highly field-aligned portion of the currents may close earthward through the ionosphere. As the DFB moves earthward, this closure creates poleward boundary intensifications. *Nakamura et al.* (2001) observed several cases in which the PBI's west/east end maps to a flow burst's evening/morning side, supporting the DF-PBI association.

Closer to the neutral sheet, the duskward DFCS currents and lower (smaller distance from the neutral sheet) ends of the region-1-sense FACs may connect to their likely source, the cross-tail current (illustrated as horizontal straight blue lines in Figure 5.4), on the dusk and dawn sides at a location tailward of the DF head line (see also *Zhang et al.*, 2011; *Yang et al.*, 2012). This current closure results in cross-tail current reduction behind the DF (absence of straight blue lines behind the saddle in Figure 5.4; they have been diverted away to be along the DF). As inferred from *Yang et al.* (2012) results, duskward DF currents near the neutral sheet may close through the ionosphere via the region-2-sense FACs earthward of the DF (closure not drawn in Figure 5.4 for simplicity). In reality, the duskward DF current may connect to both the cross-tail current and the region-2-sense FACs earthward of the DF. We have inferred possible existence of these region-2-sense FACs from magnetic field perturbations in section 5.2.1. We do not examine these region-2-sense FACs in this section (5.2.2) because this section's methodology only pertains to currents on the DF surface. For the same reason, the currents I studied in this section, which flows on the DF, is different from the flow-vortex-generated region-1-sense FACs outside the DFB in the *Birn et al.* (2004a) MHD simulation. Furthermore, due to the current and field rotations across the DF layer, my results provide indirect indications of the local current directions. Future studies are needed to fully resolve the DF current closure issue.

5.2.3 DFCS Thickness, Density, and Total Strength

5.2.3.1 Results

The current density of the dipolarization front current sheet can be calculated as follows:

$$i = (B_{\mathrm{in},L} - B_{\mathrm{out},L})/\mu_0,$$

$$j = i/d,$$

where i is the linear current density (the total current per unit length in $\mathbf{L}$ direction), j is the current density, and d is the DF (DFCS) thickness. The DF thickness calculation was explained in appendix B. In Figure 5.5, I investigate the spatial distribution of the quantities related to DFCS current density. For all panels that involve DF normal direction $\mathbf{n}$ (Figures 5.5b-5.5f), I show only earthward-normal DFs; $\mathbf{n}$ was calculated using the $\mathbf{B}_{\mathrm{in}} \times \mathbf{B}_{\mathrm{out}}$ method. $\mathbf{B}_{\mathrm{in}} \times \mathbf{L}$ and MinVar methods produce similar statistical trends (not shown since $\mathbf{B}_{\mathrm{in}} \times \mathbf{B}_{\mathrm{out}}$ method gives the clearest trends). To avoid event attrition from normal determination subject to goodness criteria, Figure 5.5a includes all events.

Figures 5.5a and 5.5b show the spatial variation of the DFCS linear current i. Typical (average and median) values of i at all locations on the DF are between $\sim 1.0 \times 10^7$ nA/m (0.06 MA/$\mathrm{R_E}$) and $\sim 1.8 \times 10^7$ nA/m (0.12 MA/$\mathrm{R_E}$). Starting from the lobe ($B_{\mathrm{q}x}/B_{\mathrm{lobe,q}} = \pm 1$, Figure 5.5a), i increases as the neutral sheet is approached, peaks at $B_{\mathrm{q}x}/B_{\mathrm{lobe,q}} = \pm 0.5$, and then decreases again toward the neutral sheet. The peak distance corresponds to $Z = \sim \pm 0.55l$ from the neutral sheet, where l is the ambient cross-tail current sheet half-thickness in the Harris model. Thus, the linear current density peaks midway through the plasma sheet on either side of the neutral sheet, showing a bifurcating distribution as a function of the distance from the neutral sheet. A double-peak signature also appears in the dependence of i on the azimuthal distance to the DF's head line (Figure 5.5b). The current peaks at $n_y \sim \pm 0.4$ ($\pm 24^\circ$ azimuth, assuming an ideal circular transverse section). This trend is present at all distances from the neutral sheet (this distance independence is not shown for conciseness).

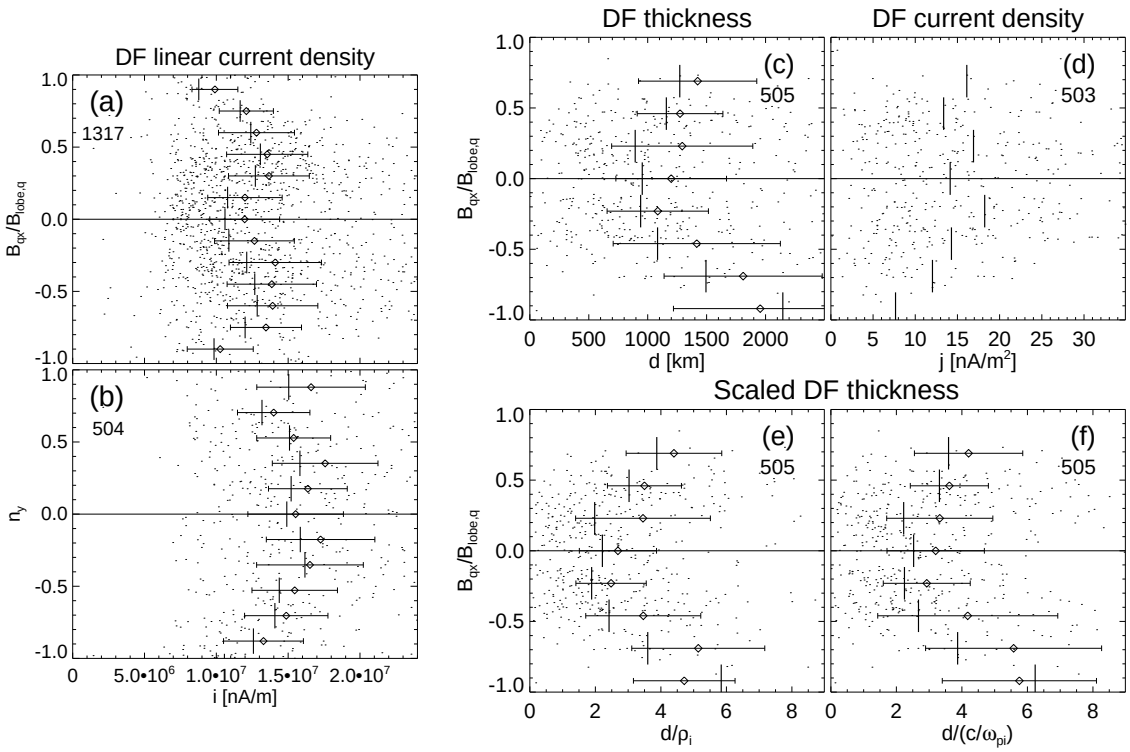

Figure 5.5: The dependence on the distance from (a and c-f) the neutral sheet and (b) n_y of dipolarization front current sheet properties: linear density in Figures 5.5a and 5.5b, thickness in Figures 5.5c, 5.5e, and 5.5f, and current density in Figure 5.5d. Each dot represents an event; Figure 5.5a includes both earthward and tailward dipolarization fronts; the other panels include only earthward-normal DFs. The DFCS current densities in Figures 5.5a, 5.5b, and 5.5d are inferred from B_L changes. In Figure 5.5e/5.5f, I scale the DF thicknesses in Figure 5.5d to each event's ion thermal gyroradius/inertial length measured at tin. All involved DF normal directions are from the $\mathbf{B}_{\rm in} \times \mathbf{B}_{\rm out}$ method. Vertical bars/diamonds represent each bin's median/average. Horizontal error bars on the diamonds represent each bin's standard deviation. We calculate medians and averages only for bins with no less than five events. Because near-zero thickness results in huge current density contaminating bin-average j, Figure 5.5d does not show averages. The number in each panel is the number of events whose information that panel contains.We have truncated the horizontal axis to show the median/average trends better, so not all the events counted into that number are visible. The slight event number differences from Figures 5.5b to 5.5f are caused by the good **L** requirement (see appendix B) and data gaps.

An examination of the DF thickness (Figure 5.5c) shows that as one moves from the outer plasma sheet towards the neutral sheet, the DF thins by more than a factor of 2 (from $>$ 2000 km to $<$ 1000 km). This thinning near the neutral sheet may be caused by compression of the DF flux tubes against the pre-existing (ambient) plasma. The $1000-2000$ km DF thickness is consistent with my rough estimate at the end of section 5.2.1.

The DFCS current density j varies from $<$ 10 nA/m^2 to $\sim$ 20 nA/m^2 (Figure 5.5d). Its dependence on the distance from the neutral sheet is simply a combination of i and DF thickness trends: the double peak has been muted (the trend is clear for the southern hemisphere but not for the northern hemisphere), with the peak density near the neutral sheet. The $\sim$ 4 nA/m^2 region-1-sense current density estimated at the end of section 5.2.1 is a fraction of the $10 - 20$ nA/m^2 total DFCS current density.

Zhang et al. (2011) suggested that in one event, the electron diamagnetic current could contribute 60% of the total DFCS current density. This diamagnetic current is atypical of DFs in general, whose currents are in agreement with ion diamagnetism and a Hall current (*Runov et al.*, 2011). Nevertheless, I can examine the total (ion and electron) pressure current's contribution to the DFCS by taking into account both ion and electron pressure gradients. According to Figures 2.2f and 2.2n, the thermal pressure drop across the DF $\Delta P_{\rm th}$ is $\sim$ 0.1 nPa. Taking the magnetic field strength B as 10 nT and DF thickness d as 1000 km, we have a diamagnetic current ($j_{\rm diag} = \Delta P_{\rm th}/Bd$) of 10 nA/m^2, equal to the statistical DFCS current density.

Figures 5.5e and 5.5f show the DF thickness distribution in physical units: I compute each event's ion thermal gyroradius $\rho_{\rm i}$ and inertial length $c/\omega_{\rm pi}$ at $t_{\rm in}$ and plot the ratio of the DF thickness to these two plasma parameters. Median values varying from 2 to 6 $\rho_{\rm i}$ in Figure 5.5e and from 2 to 6 $c/\omega_{\rm pi}$ in Figure 5.5f are consistent with the observations of *Runov et al.* (2011); *Runov et al.* (2011). The trends of these normalized quantities are the same as for the absolute values of the thickness, i.e., the DFCS thins by a factor of 2 to 3 from the outer plasma sheet to the neutral sheet.

5.2.3.2 Interpretation and Discussion

The dipolarization front's linear current density bifurcation as a function of the distance from the neutral sheet in Figure 5.5a is reminiscent of the cross-tail current sheet bifurcation at active times. *Runov et al.* (2003) and *Asano et al.* (2005) suggested that at such times the cross-tail current density often peaks away from the neutral sheet (exhibiting two peaks, one north and one south of the neutral sheet). *Runov et al.* (2003) and *Sergeev et al.* (2003) observed the bifurcated cross-tail current density to peak at $|B_x/B_{\rm lobe}| \sim 0.5$, similar to my observations of the DFCS linear current density peak location. That these two current systems peak at the same location supports my hypothesis that the cross-tail current is the likely source of the DFCS current. If the DFCS duskward current connects with region-2-sense FACs earthward of the DF, the linear current density bifurcation indicates that the region-2-sense FACs have two density peaks, one to the north and the other to the south of the neutral sheet.

The linear current density's double-peak dependence on the azimuthal distance from the DF head line (Figure 5.5b) may be caused by interplay between the emergence and the diversion of the DFCS current. As one moves from the DF's flanks to the DF's head line, the DF surface is more earthward and thus interrupts a longer portion of the cross-tail current; meanwhile, a larger portion of the azimuthally distributed region-2-sense FACs ahead of the DF can contact the DF. As more cross-tail currents and/or region-2-sense FACs join the DFCS, the DFCS current increases. On the other hand, the DFCS currents are diverted into a more field-aligned configuration at lager distances from the neutral sheet; closer-to-neutral-sheet currents feeding that portion therefore need to be reduced towards the DF's head line. This effect, which is illustrated in Figure 5.4 as reduced blue-line density towards the head line, could account for the observed current reduction towards the DF head line. Figure 5.4, however, does not depict the current increase away from the DF's flanks because I have forced the currents to flow in or out of the DF only at the dawn and dusk ends (at field lines 2 and 5) to simplify the figure. In actuality I expect the cross-tail current and/or region-2-sense FACs (not shown in Figure 5.4) ahead of the DF to flow onto the DF along

its entire surface, as discussed earlier.

5.2.4 Cross-tail Current Sheet Modification by Dipolarizing Flux Bundles

5.2.4.1 Results

In this section, I investigate the changes that DFBs bring to the cross-tail current. First, I compute the lobe magnetic field $B_{\rm lobe}$ before and after DF arrival from local total plasma pressure measurements (explained in section 2.2.1). The lobe field ahead of the DF is taken as its average in the $t_0 - 3$min to $t_0 - 2$min time range. Because my selection criteria cannot guarantee quiet plasma conditions after DF passage, I limit the time range for calculating average $B_{\rm lobe}$ to $t_0 + 30$ s to $t_0 + 90$ s after DF passage to avoid contributions from subsequent DFBs. Due to the large B_z value and fluctuations behind the DF, the estimate of the lobe field behind the DF is very rough. Nevertheless, I found that $B_{\rm lobe}$ decreased (increased) after the passage of 821 (499) DFs: Most DFBs are associated with lobe magnetic field reduction, which indicates the reduction of the cross-tail current. This finding is consistent with the result of Figures 4.1e and 4.1f.

Next, I cast my observations in absolute distance terms by computing the typical value of the ambient cross-tail current sheet thickness in my database. Observations from two Z-separated satellites can be used to solve for the parameters of the Harris current sheet model (*Harris*, 1962), which is assumed to be a good approximation of the pre-DFB (typically thin) cross-tail current sheet (I will also apply it to the after-DFB region for rough estimations). The parameters are $2l$, the thickness of the cross-tail current sheet, and $z_{\rm ns}$, the Z-location of the neutral sheet:

$$B_x = B_{\rm lobe} \tanh[(z - z_{\rm ns})/l].$$

The pre-DFB cross-tail current density is then $B_{\rm lobe}/\mu_0 l$. B_x, $B_{\rm lobe}$, and the satellite location z are observational quantities.

During THEMIS's 2009 tail season, P5 was close to either P3 or P4. Due to its slightly different orbit inclination from P3 and P4 but nearly identical (in X and Y) apogee and

perigee to those of P3 and P4, P5 was often immediately below P3 or P4 (small X and Y separation relative to their Z separation). We used P5 as one observation point and P3 or P4 (depending on which was closer to P5 in their XY projection) as the other point to solve the Harris current sheet equations for l. Again, I took the average measured quantities of $t_0 - 3$min to $t_0 - 2$min and $t_0 + 30$ s to $t_0 + 90$ s as their values before and after DF arrival, respectively, to infer the DFB-associated change in the cross-tail current sheet thickness and strength. Seventy-three events in the 2009 tail season observed simultaneously by P5 and one of P3 and P4 can be solved for l. We used these events to determine the absolute properties of the cross-tail current.

Fifty (23) of the DFBs in the above database were accompanied by a $B_{\rm lobe}$ decrease (increase), 59 (14) of the events showed an increase (decrease) in the cross-tail current sheet thickness, and the cross-tail current density dropped (increased) after the passage of 58 (15) DFs. The average cross-tail current sheet thickness before (after) DF arrival was 3.4 R_E (4.6 R_E) in Harris approximation; the corresponding medians were 3.0 R_E (3.9 R_E). The average cross-tail current density before (after) DF arrival was 3.90 nA/m^2 (2.76 nA/m^2); the corresponding medians were 3.12 nA/m^2 (2.31 nA/m^2). Therefore, in addition to lobe field reduction, DFBs are associated with cross-tail current sheet thickening and cross-tail current density weakening. All these properties confirm the *Palin et al.* (2012) results obtained from measurements farther away from the DF and are consistent with effects of tail reconnection in the course of substorms (*Coroniti*, 1985).

We expect the cross-tail current sheet expansion to make the magnetic field lines behind the DF ($\mathbf{B}_{\rm in}$) more dipolar than those ahead of it ($\mathbf{B}_{\rm out}$ and the unperturbed magnetic field a few minutes before DF arrival). The curvature of the field line embedded inside the DF $\mathbf{B}_{\rm mid}$ should be between those of $\mathbf{B}_{\rm in}$ and $\mathbf{B}_{\rm out}$. In Figure 5.6, I determine the angle between the magnetic field's XZ projection B_{XZ} and the Z axis $\theta_{B_{XZ}\text{-}Z}$ to investigate this effect. As illustrated in Figure 5.6a, upper left corner, I define $\theta_{B_{XZ}\text{-}Z}$ as positive/negative when B_{XZ} rotates counter-clockwise/clockwise from the Z axis. For a dipole-like field line, this angle is positive/negative when the probe is located north/south of the neutral sheet and grows from 0° to -90° from the neutral sheet to the lobe. Figures 5.6a-5.6c show the $\theta_{B_{XZ}\text{-}Z}$ dependence

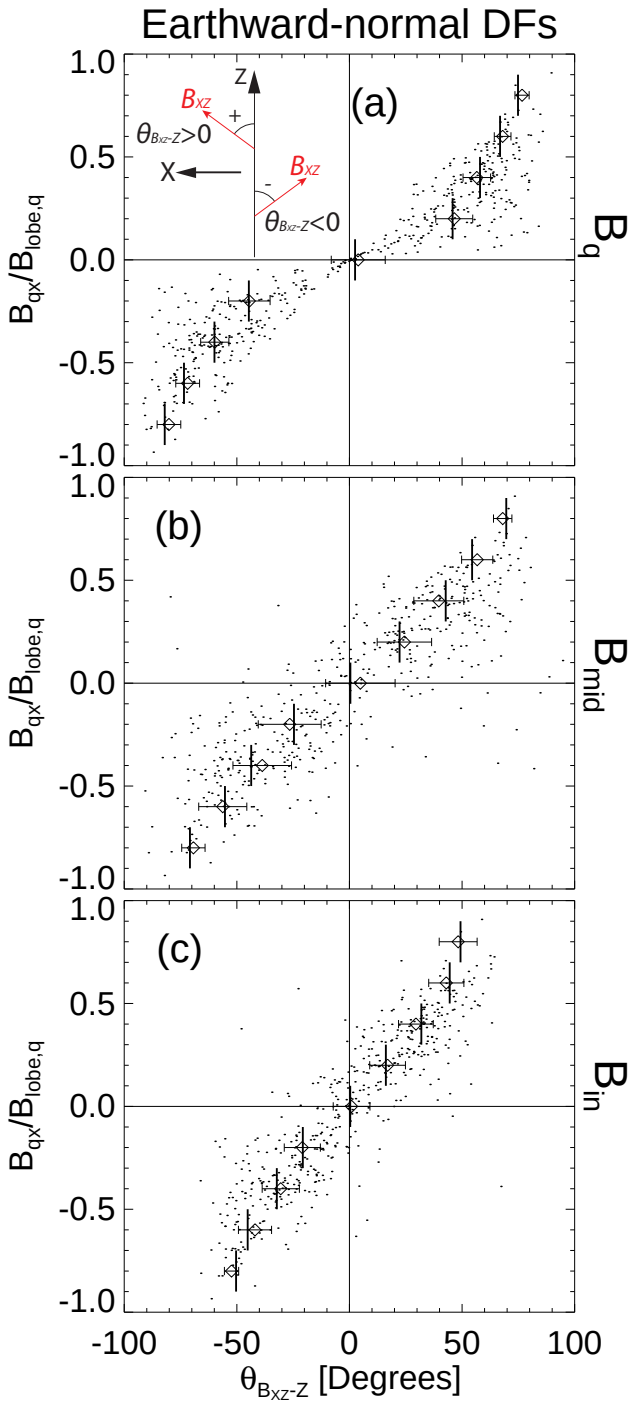

Figure 5.6: $\theta_{B_{XZ}\text{-}Z}$ (the angle by which B_{XZ} rotates from the Z axis, illustrated in the second quadrant of Figure 5.6a) dependence on distance from the neutral sheet for (a) $\mathbf{B}_{\rm q}$, (b) $\mathbf{B}_{\rm mid}$, and (c) $\mathbf{B}_{\rm in}$. All panels include only earthward-normal DFs (determined by $\mathbf{B}_{\rm in} \times \mathbf{B}_{\rm out}$ method, 505 events), and each dot represents an event. Vertical bars/diamonds are the $\theta_{B_{XZ}\text{-}Z}$'s median/average of each $B_{qx}/B_{\rm lobe,q}$ bin. Medians and averages are shown only for bins with no less than five events.

on the distance from the neutral sheet for field lines $\mathbf{B}_{\mathrm{q}}$, $\mathbf{B}_{\mathrm{mid}}$, and $\mathbf{B}_{\mathrm{in}}$. Here $\mathbf{B}_{\mathrm{q}}$ is the average magnetic field from $t_0 - 3$min to $t_0 - 2$min representing the pre-DF unperturbed magnetic field and $\mathbf{B}_{\mathrm{mid}}$ is the magnetic field at $t_{\mathrm{mid}} = 0.5(t_{\mathrm{out}} + t_{\mathrm{in}})$. Unfortunately, due to its occasional B_z reversal, $\mathbf{B}_{\mathrm{out}}$ is too noisy to yield a clear trend. In each of the three groups in Figure 5.6, most events have a small B_y, so the XZ projections can, to a large extent, represent pictorially not just a 2-D projection but a good approximation of the actual 3-D field line configuration.

5.2.4.2 Interpretation and Discussion

Using the linear interpolations to the $\theta_{B_{XZ}\text{-}Z}$ medians of the neutral-sheet-distance bins in Figure 5.6, I attempt to reconstruct the XZ projections of $\mathbf{B}_{\mathrm{q}}$, $\mathbf{B}_{\mathrm{mid}}$, and $\mathbf{B}_{\mathrm{in}}$ in Figure 5.7. Note that I have translated $B_{\mathrm{q}x}/B_{\mathrm{lobe,q}}$ into a physical distance estimate from the neutral sheet in $\mathrm{R_E}$ (along Z) by inserting the median pre-DF cross-tail current sheet thickness I found in my 2009 database, $l \sim 1.5$ $\mathrm{R_E}$, into the Harris current sheet model. The reconstructed field line projections suggest that $\mathbf{B}_{\mathrm{in}}$ bends less than $\mathbf{B}_{\mathrm{mid}}$ and $\mathbf{B}_{\mathrm{q}}$, i.e., the field line curvatures are consistent with the cross-tail current sheet expansion I observed and magnetic field dipolarization during DFB passage.

In Figure 5.7, I also draw the DF median thicknesses of Figure 5.5c (black bars) and derive from them the DF's outer boundary (dashed curve).

It is evident from Figure 5.7 that $\mathbf{B}_{\mathrm{mid}}$, and by inference $\mathbf{B}_{\mathrm{out}}$ ($\mathbf{B}_{\mathrm{out}}$ should be more stretched than $\mathbf{B}_{\mathrm{mid}}$), is more stretched than the DF's outer boundary (this conclusion is reached for $\mathbf{B}_{\mathrm{in}} \times \mathbf{B}_{\mathrm{out}}$ events with a greater than 30° angle between $\mathbf{B}_{\mathrm{in}}$ and $\mathbf{B}_{\mathrm{out}}$). The stretchiness of $\mathbf{B}_{\mathrm{out}}$ is directly related to the small B_z reduction ahead of the DF (Figures 2.2c and 2.2k). My explanation is that either (1) the fringe fields of the finite-height DFCS further reduce $\theta_{B_{XZ}\text{-}Z}$ ahead of the front or (2) the ambient plasma is pushed DF-flankward and tailward by the earthward-normal DF, dragging $\mathbf{B}_{\mathrm{out}}$, which is frozen into it. This dragging can penetrate to the location of $\mathbf{B}_{\mathrm{mid}}$. The ambient flow, the flow vortex, and the earthward flow inside the DFB form multiple shear flow layers surrounding the DF, which

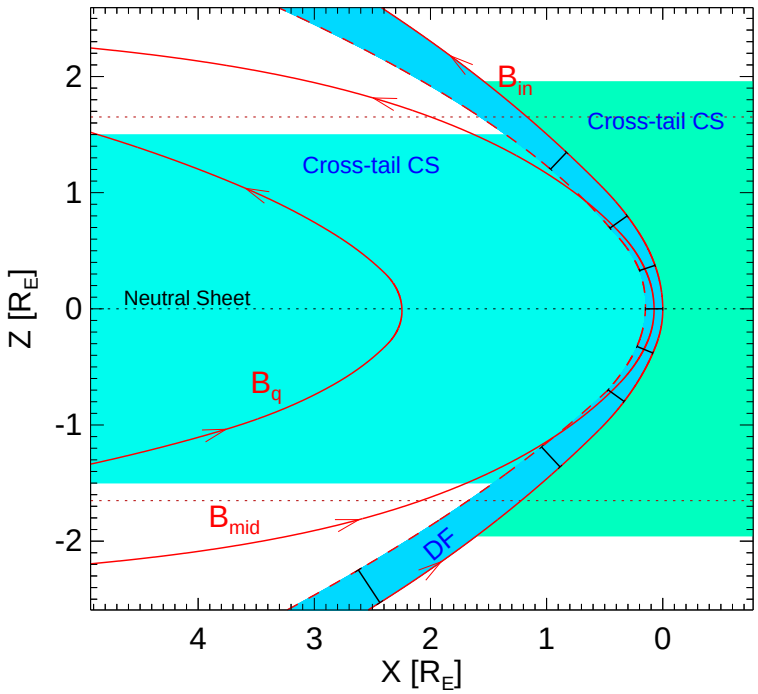

Figure 5.7: Reconstruction of an earthward-normal dipolarization front. In this figure, I have translated the GSM coordinate system to originate from the DF's head point at the neutral sheet. The red solid lines (from left to right), $\mathbf{B}_{\rm q}$, $\mathbf{B}_{\rm mid}$, and $\mathbf{B}_{\rm in}$, are field line XZ projections interpolated from the $\theta_{B_{XZ}\text{-}Z}$ medians in Figure 5.6. The two red dotted lines at $Z = \pm 1.65$ $\mathrm{R_E}$ correspond to the highest bin centers ($B_{{\rm q}x}/B_{\rm lobe,q} = \pm 0.8$) in Figure 5.6. The black bars anchored at $\mathbf{B}_{\rm in}$ are the DF median thicknesses at different distances from the neutral sheet, taken from Figure 5.5c. The dashed curve, the quadratic interpolation of the thickness bars' earthward ends, represents the XZ projection of the DF's outer (in this case, earthward) boundary. $\mathbf{B}_{\rm mid}$ is positioned to intersect thickness bar's midpoint at the neutral sheet. $\mathbf{B}_{\rm q}$ is placed at an arbitrary location earthward of $\mathbf{B}_{\rm mid}$. The cross-tail current sheet thicknesses (two light blue areas) ahead of and behind the DF (thin blue region) are the medians from the 2009 multi-point observations (explained in section 5.2.4.1.

contribute field-aligned components to both the local DFCS and the extended current system surrounding the DF (*Birn et al.*, 1999). Scenarios 1 and 2, which may occur simultaneously, even result in over-stretching: the far-from-neutral-sheet ends of the reconstructed $\mathbf{B}_{\mathrm{mid}}$ (and by inference $\mathbf{B}_{\mathrm{out}}$) are more stretched than those of $\mathbf{B}_{\mathrm{q}}$.

Finally, it is noteworthy that each reconstructed field line in Figure 5.7 is a combination of different temporal stages of the DF field lines. An observation far from the neutral sheet corresponds to an earlier DF-evolution stage than a neutral sheet observation at the same downtail location; the far-from-neutral-sheet DF's equatorial part is still farther down tail. Thus, the far-from-neutral-sheet parts of the reconstructed field lines in Figure 5.7 are from earlier stages than their near-neutral-sheet parts.

5.3 Summary and Additional Discussion

Using a comprehensive dipolarizing flux bundle (DFB) event database, I infer the properties and structure of the DFB's current system, especially of the dipolarization front current sheet (DFCS) that encompasses a DFB. My findings are as follows:

- Near the neutral sheet and the DF's head line, the average current over the DF thickness is perpendicular to the DFB's internal magnetic field and the average magnetic field direction over the DF thickness. Farther from the neutral sheet and azimuthally away from the DFs head line, however, the DFCS has a significant component aligned with the internal and average fields. By inference, the DFCS's local field-aligned component is in the region-1 sense and is more prominent away from the neutral sheet and towards the DF's flanks. The existence of such region-1-sense FACs and their prominence far from the neutral sheet are also inferred by magnetic field dawn-dusk component variations. At larger distances ahead of (earthward of) the DFCS, a distributed, region-2-sense field-aligned current system may also accompany the front. My observations are consistent with previous modeling (e.g., *Yang et al.*, 2011) and the prediction from thermal pressure distribution (Chapter 4).

- The typical DFCS (DF) thickness is 800 to 2000 km (thinnest at the neutral sheet, comparable to one to several ion inertial lengths), and its typical current density is 10 to 20 nA/m^2. These ranges are consistent with the *Runov et al.* (2011) results from multi-case studies.

- On a sagittal cross section, the DF linear current density peaks at $B_x/B_{\rm lobe} \sim \pm 0.5$ relative to the pre-DFB thin neutral sheet parameters. This peak corresponds to a distance $\Delta Z \sim \pm 0.82$ R$_{\rm E}$ from the neutral sheet. On a transverse cross section, the linear current density peaks at $\sim \pm 24^\circ$ azimuthal angle from the DF's head line. The linear density decreases away from the sites of those maxima toward the neutral sheet, far-from-neutral-sheet locations, the DF's head line, and the DF's flanks.

- DFBs are associated with lobe field reduction (cross-tail current reduction), cross-tail current sheet thickening (from $\sim$ 3 R$_{\rm E}$ to $\sim$ 4 R$_{\rm E}$), and cross-tail current density reduction (from $\sim$ 3.5 to $\sim$ 2.5 nA/m^2). These signatures are also expected during substorms, suggesting that DFBs are an integral part of the substorm process.

- Among the three DF normal direction determination methods ($\mathbf{B}_{\rm in} \times \mathbf{B}_{\rm out}$ method and two others; see appendix B), the one based entirely on the tangential discontinuity assumption ($\mathbf{B}_{\rm in} \times \mathbf{B}_{\rm out}$ method) organizes data best. This fact implies that most DFs are likely tangential discontinuities.

Putting my conclusions in the context of previous work, I may draw a general picture of the evolution of the DFB's current system. Dipolarizing flux bundles are generated at around 20-50 R$_{\rm E}$ downtail, most likely by reconnection (e.g., *Semenov et al.*, 2005; *Sitnov et al.*, 2009), and then move earthward. The DFB's strong magnetic field leads to a strong duskward dipolarization front current sheet. At the same time, the DFB motion builds up thermal pressure around it (see Chapter 4), which results in region-2-sense FACs ahead of the DFB and region-1-sense FACs inside the DF layer. When the DFB is traveling, its B_z is frequently observed to maximize within 10 s and return to the pre-DF value within less than a minute (*Runov et al.*, 2009). Nevertheless, its local passage results in a significant, long-duration modification to the cross-tail current. The DFCS may connect to the ionosphere via both

region-1-sense and region-2-sense FACs, and as a DFB moves earthward, it is expected to generate equatorward propagating north-south arcs, often originating at poleward boundary intensifications (e.g., *Kauristie et al.*, 2000; *Zesta et al.*, 2000, 2002; *Nakamura et al.*, 2001; *Nishimura et al.*, 2010a,b). Lastly, as the DFB merges smoothly with Earth's dipole field, B_z is observed not returning to its pre-DF value after dipolarization. The disappearance of a field gradient between the DFB and the external, strong dipole field obviates the need for a DFCS. At the same time, by perturbing the pressure profile of the plasma sheet inner boundary, the DFB contributes to the current and flow perturbations associated with substorm current wedge formation, consistent with the disappearance of the DFCS.

Latest models of the substorm current wedge based on ground and space observations (e.g., *Sergeev et al.*, 2011) suggest that a SCW in space consists of a pair of current loops, one in region-1 sense and the other in region-2 sense (located earthward of the region-1-sense loop). The region-2-sense loop has less current than the region-1-sense loop so that the net effect is region-1-sense. On the other hand, a DFB can sustain a region-1-sense current sheet on the DF and a wider region-2-sense current sheet earthward of it. The two sheets carry comparable field-aligned currents near the neutral sheet, but far from the neutral sheet, the region-2-sense current sheet has significantly less total current in each leg than the region-1-sense current sheet. It is possible that a DFB can feed these FACs into the ionosphere. The configurational resemblance between the DFB-associated current sheets and the latest SCW models indicates that DFBs function as individual pieces of a substorm current wedge, i.e., as "wedgelets". As I have shown in Chapter 4, the wedgelet's FACs are supported by the DFB motion—as long as a DFB moves, it creates pressure distribution that leads to the FACs. Follow-up observations showing that traveling DFBs already carry FACs in the 15-19 R_E downtail region, not long after they are generated, support this scenario (*Sun et al.*, 2013). Therefore, a wedgelet represents the propagation state of a SCW element.

It would be instructive to determine how efficiently a wedgelet can divert the cross-tail current and what fraction of a SCW can be drawn from the collapse of a wedgelet. We have shown that the typical DFCS linear current density is $1.0 \times 10^7 - 1.8 \times 10^7$ nA/m ($0.06 - 0.12$ MA/R_E) at all DF-azimuths and distances from the neutral sheet. If the DF

has 1 to 3 R_E extent in the direction along the DF surface and perpendicular to the DF current, one to a few wedgelets can completely divert the local cross-tail current of 4×10^7 nA/m (the unit length of this linear density is approximately along X). Each of the SCW's two loops carries a current on the order of 1 MA for a moderate substorm (e.g., *Sergeev et al.*, 2011). Therefore, upon collapse, several wedgelets can supply the region-1-sense or the region-2-sense component or both components of the SCW (as shown qualitatively by *Yang et al.* (2012)), depending on how the DFCS is finally diverted in reality.

CHAPTER 6

Conclusions

Dipolarizing flux bundles (DFBs) are an important participant in many aspects of magnetotail dynamics. In this thesis, a comprehensive statistical study has been employed to explore three aspects of DFBs: their role in tail magnetic flux transport, what controls their motion, and their current system. This thesis has accomplished the following main tasks:

1. Established that DFBs are the major, highly efficient carrier of near-earth magnetotail flux.

2. Showed that DFB motion builds up pressure at its leading edge; in a statistical sense, the buildup exerts a braking force comparable to the driving force of DFB motion.

3. Suggested that a DFB has a current system comparable in configuration and strength to a substorm current wedge—each DFB is a "wedgelet", a building block of the SCW.

Chapter 3 discusses the importance and properties of DFBs in magnetotail flux transport. I show that although BBF-embedded DFBs occupy only only $\sim 30\%$ of BBF duration, they contribute $\sim 70\%$ of BBF magnetic flux transport. Therefore, because BBFs are major magnetic flux transporters in the magnetotail, DFBs are also major flux transporters in near-earth tail convection. In this chapter I also show various DFB flux transport properties depending on tail location and geomagnetic activity. I further estimated that DFBs contribute $40-70\%$ of the near-earth tail flux transport, although they are observed only 3-4% of the time in the central plasma sheet—DFBs are the major, high-efficiency flux transporter in the near-earth magnetotail. In this chapter I also showed that DFBs have a higher flux transport rate when observed closer to Earth, in the tail's pre-midnight sector, farther away

from the neutral sheet, and during substorm time. The high rate in the latter two conditions leads to more flux transport of individual DFBs. In addition, DFBs appear more often during substorm time. Because of the DFB's importance in tail flux transport, these DFB flux transport characteristics may shape the entire near-earth magnetotail convection.

In Chapter 4 I investigated the factors that control DFB motion and the effects arising from the pressure and flow perturbations created by that motion. The results showed that DFB motion causes the total pressure to build up inside the DF layer; this buildup exerts a tailward pressure gradient force to slow the DFB's earthward motion. Then I established that a modified total pressure effective only in the radial (relative to the DFB center) direction is more relevant to DFB motion. This radial total pressure also builds up inside the DF layer. On a statistical basis, the tailward radial total pressure gradient force density is ~ 0.15 nPa/R_E, comparable to the earthward magnetic curvature force density. Statistically, the DFB is in approximate force balance. Considering the results in Chapter 3, I concluded that in a statistical sense the pressure gradient force is a little higher than the curvature force earthward of 15 R_E downtail, whereas the curvature force is a little higher than the pressure gradient force beyond 15 R_E downtail. Dipolarizing flux bundle motion also builds up thermal pressure earthward of it; the buildup is strongest at the DFB's meridian of symmetry. When combined with the flux tube volume distribution around the DFB, such thermal pressure distribution requires region-2-sense field-aligned currents (FACs) earthward of the DFB and region-1-sense FACs inside the DF layer.

Chapter 5 deals with the DFB current system. Magnetic field variations around the DFB indicate the existence of region-2-sense FACs earthward of the DFB and region-1-sense FACs inside the DF layer, consistent with pressure distribution requirements shown in Chapter 4. Such a configuration is similar to that of a substorm current wedge. I further investigated the region-1-sense FACs inside the DF layer and found that they are more prominent away from the neutral sheet and at the DFB's flanks; at other locations the DF current is mostly perpendicular to the magnetic field. The DF current density showed bifurcated distribution with peaks to the north and south of the neutral sheet, respectively. Such a distribution is similar to the cross-tail current distribution, which also has two density peaks at the same

locations, so the DF current and the cross-tail current are most likely connected. From the DF current density I estimated that the amount of current carried by several DFBs is enough to form a SCW of $\sim$ 1 MA typical strength. Therefore, DFBs are "wedgelets"— traveling building blocks of the substorm current wedge.

APPENDIX A

Correcting THEMIS EFI measurements

The THEMIS electric field instrument can only measure the satellite spin-plane components and suffers from offset. Thus the EFI data need to be corrected before using. In the following, I first introduce an easy correction method which I use in all my studies, and then explain that the imprecision of this method (neglecting ambient convection) do not affect my results.

A.1 The correction method

First of all, I remove the offset of the electric field data's spin-plane components ($E_{x,\mathrm{DSL}}$ and $E_{y,\mathrm{DSL}}$). As this offset varies all the time, I remove it event by event. I determine the offset as the mean measured value of a pre-event quiet time range and subtract it from the data. For my dipolarizing flux bundle and bursty bulk flow events, I use $t_0 - 3\mathrm{min}$ to $t_0 - 2\mathrm{min}$ as the pre-event quiet time range, where t_0 is the start of each event.

After correcting the spin-plane components I can infer the axial component from them. I use the relationship $\mathbf{E} \cdot \mathbf{B} = 0$ (the parallel electric field is zero for low-frequency variations) to infer $E_{z,\mathrm{DSL}}$:

$$E_{z,\mathrm{DSL}} = -\frac{E_{x,\mathrm{DSL}} B_{x,\mathrm{DSL}} + E_{y,\mathrm{DSL}} B_{y,\mathrm{DSL}}}{B_{z,\mathrm{DSL}}}$$

When the magnetic field has a very shallow angle ($< 5^\circ$) with respect to the spacecraft's spin plane, noisy $E_{z,\mathrm{DSL}}$ values appear resulting from even small noise levels in B_z. At such times, the inferred $E_{z,\mathrm{DSL}}$ data were flagged. Then I interpolated across the flagged gaps smaller than 30 s. Next I rotate the data to GSM using standard methods.

The above technique introduces data gaps to three-component $\mathbf{E}_{\mathrm{GSM}}$. When I need only the E_y component (as in chapter 3), I use $E_{y,\mathrm{DSL}}$ to approximate $E_{y,\mathrm{GSM}}$. This is because in

most cases the duskward directed electric field is nearly identical in the two systems (DSL and GSM), except for a sign change to account for the spin axis of P1 and P2, which were close to ecliptic normal south. In other words, the spin planes of all probes were approximately in the $X - Y_{\rm GSM}$ plane, and the intersection of the spin plane and the $X - Y_{\rm GSM}$ plane lies very near the $Y_{\rm GSM}$ and $Y_{\rm DSL}$ axes.

A.2 Considering quiet-time convection

The offset removal operation in the previous section is imprecise due to possible background steady convection and ion-gyro scale effects. To examine whether the background convection is important, I compute the average $\mathbf{V}_{\rm i} \times \mathbf{B}$ ($\mathbf{V}_{\rm i}$ is the ion bulk velocity, $\mathbf{B}$ is the magnetic field) and its standard deviation from $t_0 - 3$min to $t_0 - 2$min for each event of the dipolarizing flux bundle event list (see section 2.2.1 for the descriptions of this list and t_0). I then calculate the average spin-plane components of these quantities for all my events as shown in Table A.1. Both spin-plane components of $\mathbf{V}_{\rm i} \times \mathbf{B}$ are small in absolute average value (less than 0.3 ± 0.4 mV/m) and variation (less than 0.25 ± 0.3 mV/m) from $t_0 - 3$min to $t_0 - 2$min, indicating that the background convection is not strong enough to contaminate my EFI offset removal.

$\mathbf{V}_{\rm i} \times \mathbf{B}$ cannot represent the background electric field generated by ion-gyro scale effects. To account for all effects, I repeat the EFI data offset removal procedure by comparing with the quantity $\mathbf{V}_{\rm e} \times \mathbf{B}$ ($\mathbf{V}_{\rm e}$ is the electron bulk velocity), which can better agree with the actual electric field than $\mathbf{V}_{\rm i} \times \mathbf{B}$ does. To be more specific, I use the difference between EFI spin-plane measurements and $\mathbf{V}_{\rm e} \times \mathbf{B}$ spin-plane components and use the average of this difference on the time range from $t_0 - 3$min to $t_0 - 2$min as the offset. Everything else on the EFI data processing is the same. Next I repeat my statistical study with the new EFI offset removal method. The numbers of earthward (tailward) -normal DFs in each event subset are now: 785 (191) for MinVar events, 410 (94) for $\mathbf{B_{in}} \times \mathbf{L}$ events and 489 (89) for $\mathbf{B_{in}} \times \mathbf{B_{out}}$ events; i. e., 15-19% of all events have tailward normal directions. The percentage of tailward-normal events is a little higher but close to that obtained by offset

component k	X, DSL	Y, DSL
$\overline{\lvert\langle(\mathbf{V}_\mathrm{i}\times\mathbf{B})_k\rangle\rvert}$	0.233	0.298
$\Sigma_{\lvert\langle(\mathbf{V}_\mathrm{i}\times\mathbf{B})_k\rangle\rvert}$	0.243	0.400
$\overline{\sigma_{(\mathbf{V}_\mathrm{i}\times\mathbf{B})_k}}$	0.167	0.247
$\Sigma_{\sigma_{(\mathbf{V}_\mathrm{i}\times\mathbf{B})_k}}$	0.158	0.264

Table A.1: The statistical characteristics of the $\mathbf{V}_\mathrm{i}\times\mathbf{B}$ spin plane components (X, DSL and Y, DSL components). The $\langle\rangle$ sign represents the average value over the time range from t_0-3min to t_0-2min for each individual event; the top bar represents the average value for all of my 1326 events with fast-survey plasma measurements. Lower case σ is the standard deviation over the time range from t_0-3min to t_0-2min for each individual event; capital Σ is the standard deviation of all my events.

determination with solely EFI data (as in the main article). All the statistical results with the new offset removal are qualitatively the same as those in the main article. I show DF thickness and current density distributions obtained with the new offset removal method in Figure A.1. These are the only statistics in which the subjects themselves depend on electric field measurements (to calculate the DF thickness); all other statistics use electric field data only to decide which events have earthward normal. The trends described in the main article are obviously present in Figure A.1. The DF thicknesses in Figure A.1a are not as well organized as in Figure 5.5c (of the main article); this degeneration may result from contaminations in $\mathbf{V}_\mathrm{e}$ measurements. The agreement between the statistical results using the two EFI offset removal methods proves that electric field deviation from zero in the time range t_0-3min to t_0-2min is too small to affect my results.

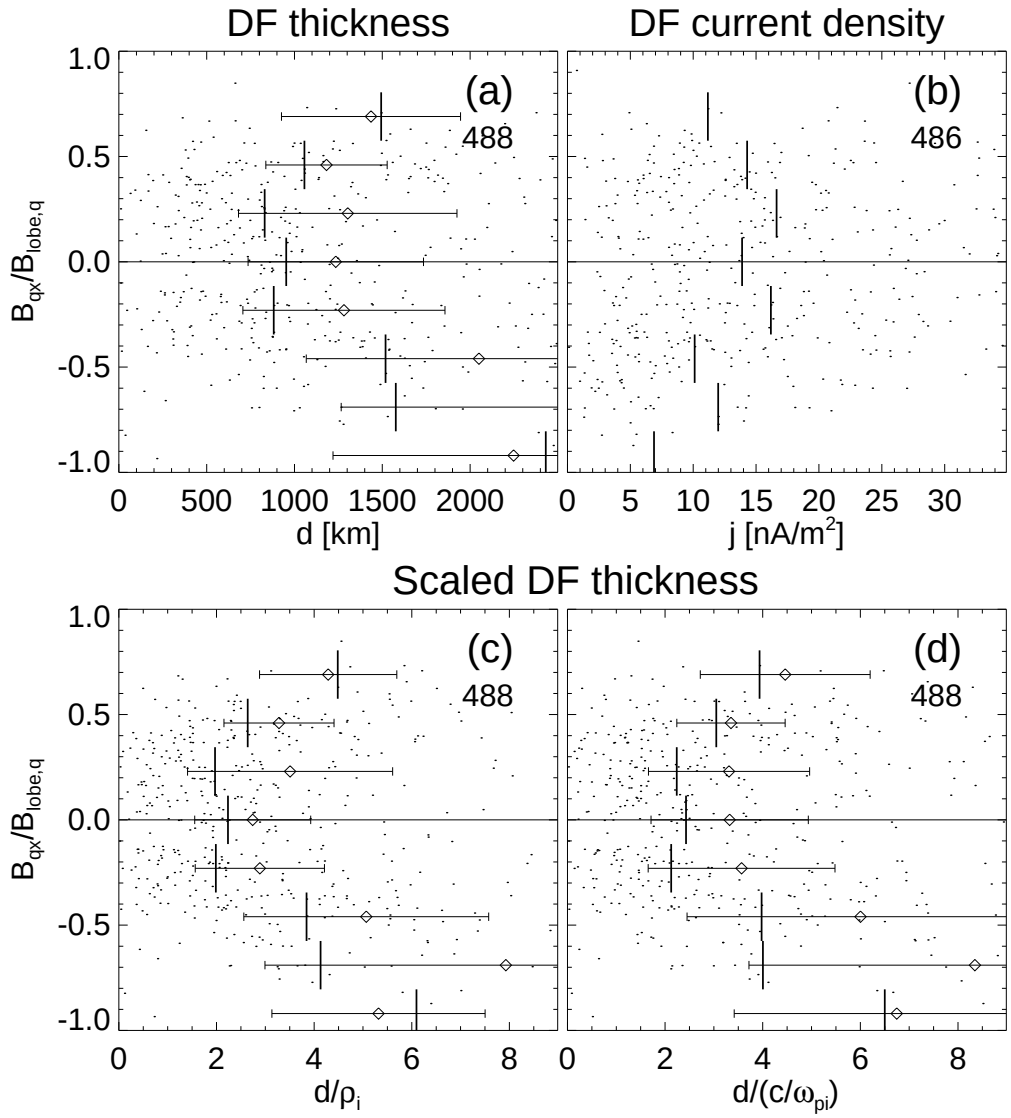

Figure A.1: The dipolarization front thickness and current density distributions calculated with EFI offset removal regarding $\mathbf{V}_e \times \mathbf{B}$ data. Panels a-d are plotted in the same way as Figure 5.5c-f in the main article. Electron measurement availability has reduced useful event number.

APPENDIX B

Determining the Dipolarization Front's Normal Direction

The best way to determine a propagating front's normal direction in 3-D space is by observing it from at least four points (e.g., *Nakamura et al.*, 2002; *Shi et al.*, 2005). When only single-point observations of DFs are available, normal-determination methods are applied on time series data as the front travels past the spacecraft. This requires the front to be sufficiently thin that the spacecraft enters and exits it at locations with approximately the same surface normal. For a typical dipolarization front thickness of 1000-2000 km (e.g., *Runov et al.*, 2011), smaller than the dipolarizing flux bundle's typical scale size of one to several R_E (e.g., *Sergeev et al.*, 1996), single-point methods are applicable, assuming a simple curved DF. If corrugated fronts develop (*Pritchett and Coroniti*, 2010), such techniques may no longer be suitable.

The most widely used single-point normal-determination method is minimum variance analysis (MVA) (*Sonnerup and Scheible*, 1998). Following *Sergeev et al.* (1996) and *Runov et al.* (2011), I apply MVA on 0.25s fluxgate low-resolution magnetic field data (MVAB) and take the minimum variance direction as the DF normal direction $\mathbf{n}$ (MinVar method). For each event, I apply MVAB around the interval from the time when the probe is immediately ahead of the DF ($t_{\rm out}$) to the time when it has moved immediately behind the DF ($t_{\rm in}$). Since the DFCS is responsible for the magnetic field's abrupt change, the point immediately ahead of it is the B_z dip point typically seen before DFB arrival, and the point immediately behind the DF is the first B_z peak point inside the DFB. I determine $t_{\rm in}$ to be time of maximum B_z in the t_0 to $t_0 + 15$s time range and $t_{\rm out}$ to be the time of the minimum B_z in the $t_0 - 15$s to $t_{\rm in}$ time range, where t_0 is defined as the time of the first abrupt jump in B_z (see selection

criterion 1 in Section 2.2.1). The magnetic fields at these two times are $\mathbf{B_{in}}$ and $\mathbf{B_{out}}$, respectively. I interpret the magnetic field's minimum variance direction as the direction normal to the front because a current sheet does not generate a magnetic field component in the direction normal to the sheet. However, the magnetic field component in the current direction may also be small, resulting in indeterminacy of the minimum and intermediate directions. Thus, I require that the ratio between the intermediate and minimum variance direction eigenvalues σ_M/σ_N be larger than 10 for a well-determined minimum variance direction (the "good MinVar requirement"); I then take this well-determined minimum variance direction (actually one of the two oppositely directed minimum variance directions; discussed later) as the front's normal direction.

To confirm the MinVar method, I introduce two other methods of determining DF normal direction with single spacecraft measurements. Following most models that interpret a DFB as a strong B_z flux tube, I assume that a DF is a tangential discontinuity. This assumption has been supported by DF-vicinity observations of plasma flows (*Schmid et al.*, 2011), electric fields (*Fu et al.*, 2012), and plasma populations (*Sergeev et al.*, 2009). Thus, the magnetic fields immediately inside the flux tube $\mathbf{B_{in}}$ and immediately outside the flux tube $\mathbf{B_{out}}$ are parallel to the DF. Moreover, the magnetic field variance produced by a sheet current is parallel to the current sheet (in this case, the dipolarization front current sheet which overlaps the DF). In other words, the MVAB's maximum variance direction ($\mathbf{L}$) is parallel to the DF. Therefore, $\mathbf{B_{in}}$ and $\mathbf{B_{out}}$'s cross product and $\mathbf{B_{in}}$ and L's cross product both give the $\mathbf{n}$ direction. These form my $\mathbf{B_{in}} \times \mathbf{B_{out}}$ method and $\mathbf{B_{in}} \times \mathbf{L}$ method for $\mathbf{n}$ computation. I disregard the cross product's handedness, and the DF normal can be picked from two opposite directions. To ensure that the normal directions from the $\mathbf{B_{in}} \times \mathbf{B_{out}}$ and $\mathbf{B_{in}} \times \mathbf{L}$ methods are well defined, I require that (1) the strength of the magnetic field used to make the cross product ($\mathbf{B_{in}}$ and $\mathbf{B_{out}}$ for $\mathbf{B_{in}} \times \mathbf{B_{out}}$ method; $\mathbf{B_{in}}$ for $\mathbf{B_{in}} \times \mathbf{L}$ method) be greater than 2 nT (good B requirement) and that (2) the angle between any two crossed vectors, $\mathbf{B_{in}}$ and $\mathbf{B_{out}}$ ($\mathbf{L}$), be greater than 30° and smaller than 150° (good angle requirement). Finally, I require $\mathbf{L}$ to be well defined for the $\mathbf{B_{in}} \times \mathbf{L}$ method. The magnetic field maximum variance produced by the DFCS is predominantly parallel to the DF and perpendicular to the DFCS

current direction. Hence, $\mathbf{L}$ is easily well defined, and I only require that the eigenvalue's ratio σ_L/σ_M be greater than 3 for trustworthy $\mathbf{L}$ directions (good $\mathbf{L}$ requirement). Finally, I normalize the cross products to be unit vectors.

With the three methods to infer the DF normal direction, I have three subsets: MinVar, $\mathbf{B_{in}} \times \mathbf{L}$, and $\mathbf{B_{in}} \times \mathbf{B_{out}}$ events. Each subset contains the events for which the DF normal direction has been well determined (meets all good-result requirements) by the respective method.

Each normal determination method gives two oppositely directed normal directions. I choose $\mathbf{n}$ to be the one that gives a positive time integral of v_n (normal component of the DF convection speed) during the DF crossing from $t_{\rm out}$ to $t_{\rm in}$. If the normal direction chosen method has an earthward (tailward) component, the probe enters the dipolarizing flux bundle from the DF's earthward (tailward) side, and I call these events earthward (tailward)-normal DFs or DFBs. The numbers of earthward (tailward)-normal DFs in each event subset are as follows: 823 (157) for MinVar events, 425 (82) for $\mathbf{B_{in}} \times \mathbf{L}$ events, and 506 (73) for $\mathbf{B_{in}} \times \mathbf{B_{out}}$ events; i.e., 13-16% of all events have tailward $\mathbf{n}$.

In Figure B.1, I show the angle difference in the normal directions from the different methods for each event for which good determination was possible. All angle-difference histograms peak at the bin closest to 0°; the medians of the angles between the normal directions computed by different methods are all smaller than 21°, showing agreement between different methods. It would be worthwhile to compare these methods with more precise multi-point techniques in future studies.

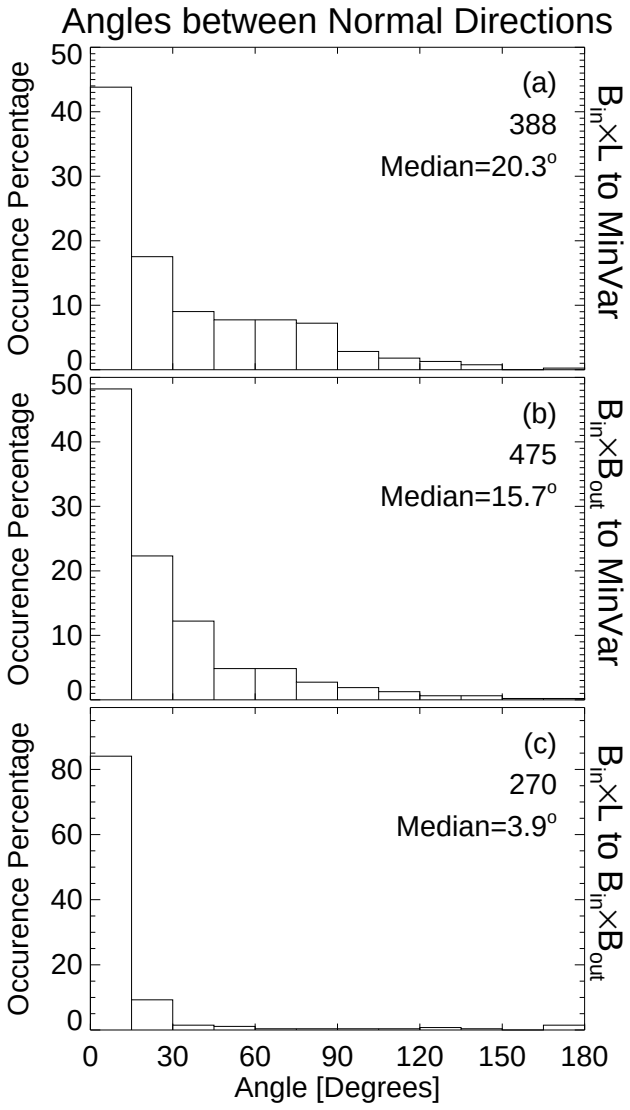

Figure B.1: Comparison of the dipolarization front normal directions from (a) MinVar and $\mathbf{B_{in}} \times \mathbf{L}$ methods, (b) MinVar and $\mathbf{B_{in}} \times \mathbf{B_{out}}$ methods, and (c) $\mathbf{B_{in}} \times \mathbf{L}$ and $\mathbf{B_{in}} \times \mathbf{B_{out}}$ methods. The integer in each panel is the number of events that can be compared using the specific methods. The "Median" in each panel is the median angle between normal directions for the events in that panel.

APPENDIX C

Reconstruction of quantity distributions around the DFB

I introduce a method in reconstructing statistical quantity maps around the DFBs in the XY plane, which give intuitive views of different quantities' distributions. The method contains several steps. First, I assume the size and shape of the transverse (parallel to XY plane) cross section of the DFB's leading portion. Second, I reconstruct satellite paths relative to the assumed DFB's leading portion from in-situ observations. In the first two steps I convert temporal data to spatial data collected on the reconstructed satellite paths. Third, I bin the data collected on the satellite paths to get a quantity map. As demanded by Chapter 4, I conduct the reconstruction in both GSM and X^*Y^* coordinates whose X^* direction is parallel to the DF convective direction (see Section 2.3.2.3 for more details about the X^*Y^* coordinate system).

In Section 2.3.2.3 I showed that the transverse cross section of the dipolarizing flux bundle resembles a semicircle and that the typical radius of this semicircle is ~ 1 R_E. Therefore, I assume that the transverse cross sections of all DFBs are 1-R_E-radius semicircles. In Figure C.1a I draw a 1-R_E-radius semicircle in GSM coordinates but with the origin at the center of the semicircle. Figure C.1b shows the semicircle in X^*Y^* coordinates. The area enclosed by the semicircle and the Y (or Y^*) axis represents the leading portion of the DFB. Next, assuming that each DFB neither deform nor change its speed much during the satellite passage through it, I reconstruct the satellite paths relative to the semicircle.

Satellite path reconstruction is done in three steps. First, I identify where and when the satellite transects the semicircle. That location is given by the dipolarization front normal

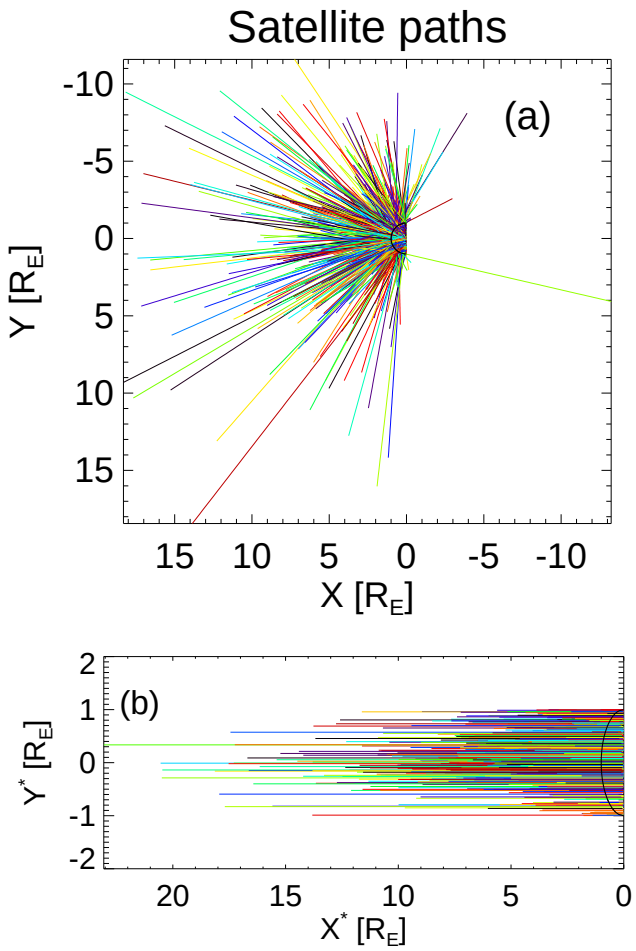

Figure C.1: Satellite paths in reconstructed from the 506 $\mathbf{B}_{\text{in}} \times \mathbf{B}_{\text{out}}$ earthward-normal events which I use in Chapter 4. Each colored straight line is the satellite path's XY projection of an individual event. The satellite path of each event is derived from the observed dipolarization front normal and convective velocity. The black semicircle in each panel denotes the outer boundary of the DFB. In Figure C.1a the paths are plotted in GSM coordinates. In Figure C.1b the paths are plotted in X^*Y^* coordinates where X^* is the DF propagation direction.

azimuth, as explained in Section 2.3.2.3 and illustrated in Figure 2.9a. The transecting time I assign to the transecting point is each event's t_{out} (see Appendix B for the definition of t_{out}), so the semicircle in Figures 2.9a, C.1a, and C.1b stands for the outer boundary of the DFB, which is also the earthward or leading boundary of the finite-thickness DF. Second, I calculate each satellite path by multiplying time by the satellite's relative velocity to the DFB and match the path to the DFB semicircle using the transecting point and time obtained in the first step. The satellite's relative velocity to the DFB is $-\mathbf{v}_{\text{DF}}$, the opposite of the DF convective velocity (see Section 2.1.0.1 for how I obtain $\mathbf{v}_{\text{DF}}$). As my quantity map reconstruction is in the XY plane, I use only the XY component of the satellite paths (see Figures 2.9a and C.1). In fact, the XY component of a satellite path largely represents the satellite path because in only 16% of my events are the $\mathbf{v}_{\text{DF}}$, and thus satellite paths, elevated more than 30° from the XY plane. Third, to ensure the quality of my statistics, I trim each satellite path XY component so that its remainder starts from the location corresponding to $t_{\text{out}} - 3\text{min}$ and stops at either ±90° azimuth (the boundary of my 2-D maps) or where it hits the DFB semicircle from the inside (where the solid part of "sc path 2" stops in Figure 2.9a). After applying these three steps to each event in my event list, I reconstruct a map of satellite paths (XY components) relative to the DFB from the 506 $\mathbf{B}_{\text{in}} \times \mathbf{B}_{\text{out}}$ earthward-normal events (see Appendix B for the explanation of such events). Figures C.1a and C.1b shows such reconstructed maps in translated GSM and X^*Y^* coordinates, respectively (the paths in Figure C.1b are all parallel to X^* because X^* was defined as the direction of $\mathbf{v}_{\text{DF},XY}$).

The essence of the satellite path reconstruction is that it converts temporal data (in-situ observations) to spatial data collected on satellite paths. For each event in my event list, the value of a physical quantity measured at each time point of the temporal data can be treated as collected at the location to which this time point corresponds on this event's reconstructed satellite path. (In practice, I treat the value as collected on the satellite path's XY component to reconstruct XY quantity maps.) Then I can bin the map of satellite paths (Figure C.1) radially and azimuthally and calculate the median of values collected on the satellite path (XY component) segments that fall into each bin to reconstruct a statistical quantity map in Chapter 4. Reconstructions based on two path types as shown in Figures

C.1a (X points earthward) and C.1b (X^* points along the DFB motion direction) enable me to evaluate how the choice of coordinates affects the quantity distributions.

At last, I note the limitations of my method. In the reconstruction I assumed the DFB's transverse cross section to be semicircular, but it may have another convex shape, such as parabolic. Furthermore, although I assumed all my events to have 1-R_E-radius cross sections, the radius actually varies from event to event. A DFB's shape and size variations affect the actual satellite path relative to it. As long as the DFB is convex, however, the variations will not affect the relative location where the satellite hits the DFB, which is given by the DF normal direction. Therefore, the closer to the DFB's outer boundary, the more reliable my reconstructions are. Because most of the results in Chapter 4 pertain to regions close to the DF, they are likely quite reliable.

APPENDIX D

Clarifying the inference of the direction of dipolarization front current

In section 5.2.2.1 I identified possible issues that may contaminate my findings. In this appendix I show that they do not affect my results.

D.1 The angle between L and Z

One potential criticism that may arise from my DFB selection criterion of a sharp jump in B_z is that the magnetic field maximum variance direction **L** could be biased to point along the Z direction. In that case, the $\theta_{\mathbf{B}_{\rm in}\text{-}\mathbf{L}}$ trends as a function of the distance from the neutral sheet in Figure 5.2 could be simply due to the increasing angle between the magnetic field $\mathbf{B}_{\rm in}$ and the Z direction away from the neutral sheet. To dispel this doubt, I examined the angle between **L** and Z $\theta_{\mathbf{L}\text{-}Z}$ in Figure D.1. In Figure D.1a, the $\theta_{\mathbf{L}\text{-}Z}$ occurrence does not peak at 0°, and large angles ($\theta_{\mathbf{L}\text{-}Z} > 30°$) occur more frequently than small angles. So no bias favoring small $\theta_{\mathbf{L}\text{-}Z}$ is introduced by the selection process. Moreover, in Figure D.1b, the average and median $\theta_{\mathbf{L}\text{-}Z}$ as function of my proxy distance from the neutral sheet show an increase away from the neutral sheet (except at the highest proxy distances, perhaps due to the small number of events there). In fact, this median angle exceeds 45° at $B_{\rm qx}/B_{\rm lobe,q} = -0.7$ and is comparable to $\mathbf{B}_{\rm in}$'s rotation angle from the Z axis at the same location (Figure 5.6c). Thus, although my selection procedure picks events based on B_z increase, the magnetic field variations of these events are not always in the Z direction, particularly at large distances from the neutral sheet.

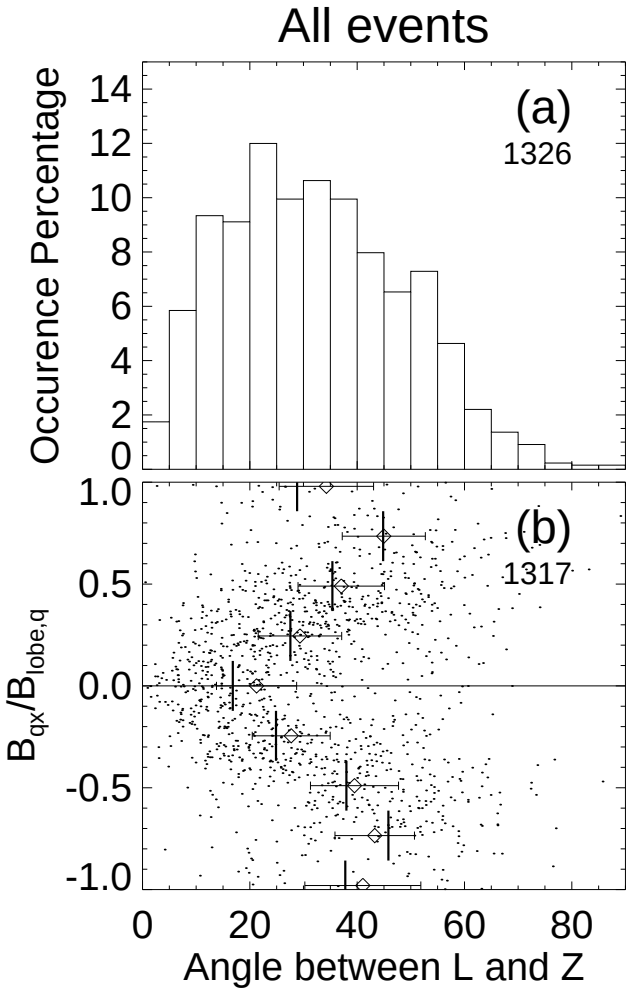

Figure D.1: The distribution of $\theta_{\mathbf{L}\text{-}Z}$, the angle between magnetic field maximum variance direction ($\mathbf{L}$) and Z: (a) the angle's occurrence rate for all events that meet the good $\mathbf{L}$ requirement and (b) $\theta_{\mathbf{L}\text{-}Z}$'s dependence on the distance from the neutral sheet. Each dot in Figure D.1b represents an event. Vertical bars/diamonds represent each bin's median/average. Horizontal error bars on top of the diamonds are each bin's standard deviation. The number in each panel is the number of events that panel contains.

D.2 The dipolarization front current direction relative to the dipolarization front average magnetic field direction

In section 5.2.2.1 I demonstrated that the average current over the dipolarization front thickness $\mathbf{j}$ is in a region-1-sense relationship to the magnetic field immediately behind the DF, $\mathbf{B}_{\rm in}$. In this auxiliary material, I compare $\mathbf{j}$ to the average magnetic field over the DF thickness.

In pure, collisionless MHD discontinuities are treated as infinitesimal. The magnetic field at the discontinuity has no normal (to the discontinuity surface) component (B_n). In reality, the dipolarization front (DF), which I assume to be a tangential discontinuity, has a finite thickness due to kinetic effects (ion or electron finite gyroradius effects at the boundary). We may modify the tangential discontinuity's magnetic field signature to be $B_n = 0$ everywhere inside the DF layer. The average magnetic field over the DF thickness, $\langle\mathbf{B}\rangle$ (in this section $\langle\rangle$ sign represents the average over the DF thickness), thus has no normal component and is parallel to the DF. Then the cross product of $\langle\mathbf{B}\rangle$ and the maximum magnetic field variance direction $\mathbf{L}$ ($\mathbf{L}$ is also parallel to the DF, see explanation in the main article) gives the DF normal direction $\mathbf{n}$. In this $\langle\mathbf{B}\rangle \times \mathbf{L}$ DF normal determination method, I compute $\langle\mathbf{B}\rangle$ as the average magnetic field from t_{out} to $t_{\rm in}$ (these two time points are defined in the main article). The criteria for good normal direction for the $\langle\mathbf{B}\rangle \times \mathbf{L}$ method are: (i) $|\langle\mathbf{B}\rangle|$ being larger than 2 nT (good $\langle\mathbf{B}\rangle$), (ii) a good $\mathbf{L}$ requirement, and (iii) a good angle requirement on the angle between $\langle\mathbf{B}\rangle$ and $\mathbf{L}$. The explanations for the latter two requirements are in the appendix of the main article.

Using $\langle\mathbf{B}\rangle \times \mathbf{L}$ to determine $\mathbf{n}$, I can repeat section 5.2.2.1 to investigate DFCS (dipolarization front current sheet) current direction ($\mathbf{L}$ as the proxy, see explanations in the main article) relative to $\langle\mathbf{B}\rangle$. The distributions of the angle from $\langle\mathbf{B}\rangle$ to $\mathbf{L}$ ($\theta_{\langle\mathbf{B}\rangle\text{-}\mathbf{L}}$, the sign of this angle is assigned in the same way as the angle from $\mathbf{B}_{\rm in}$ to $\mathbf{L}$, $\theta_{\mathbf{B}_{\rm in}\text{-}\mathbf{L}}$) are shown in Figures D.2 and D.3. The trends in all panels are the same as those in the corresponding panels in Figures 5.2 and 5.3; the DFCS current direction's relationship to $\langle\mathbf{B}\rangle$ ($\mathbf{j}$-$\langle\mathbf{B}\rangle$ relation) is in general the same as its relationship to $\mathbf{B}_{\rm in}$. Moreover, $\langle B_x\rangle$ has the same sign as B_{qx} for

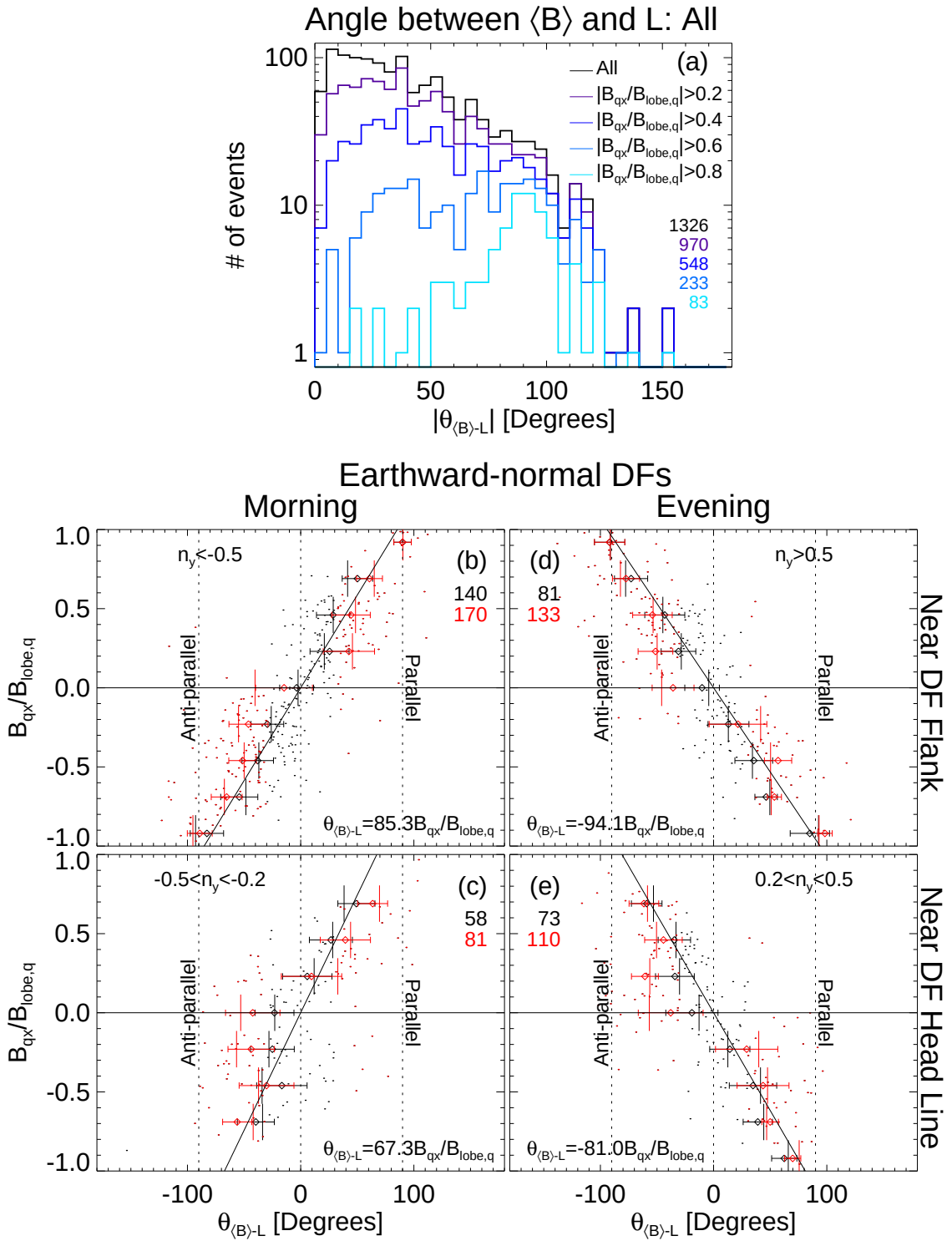
Angle between ⟨B⟩ and L: All
100
10
1
# of events
All
(a)
|Bqx/Blobe,q|>0.2
|Bqx/Blobe,q|>0.4
|Bqx/Blobe,q|>0.6
|Bqx/Blobe,q|>0.8
1326
970
548
233
83
0
50
100
150
|θ⟨B⟩-L| [Degrees]
Earthward-normal DFs
Morning
Evening
Near DF Flank
Near DF Head Line
ny<-0.5
(b)
140
170
ny>0.5
(d)
81
133
-0.5<ny<-0.2
(c)
58
81
0.2<ny<0.5
(e)
73
110
Anti-parallel
Parallel
θ⟨B⟩-L=85.3Bqx/Blobe,q
θ⟨B⟩-L=-94.1Bqx/Blobe,q
θ⟨B⟩-L=67.3Bqx/Blobe,q
θ⟨B⟩-L=-81.0Bqx/Blobe,q
Bqx/Blobe,q
1.0
0.5
0.0
-0.5
-1.0
-100
0
100
θ⟨B⟩-L [Degrees]

95% of my events (1844 out of 1950; B_{qx} is the quiet time average B_x, see main article for explanation), so the DFCS $\langle\mathbf{B}\rangle$-aligned component $j_{\|\text{-}\langle\mathbf{B}\rangle}$ is earthward/tailward on the DF's morning/evening part. The $\mathbf{j}$-$\langle\mathbf{B}\rangle$ relation is thus a region-1-sense relationship.

One doubt about the region-1-sense $\mathbf{j}$-$\langle\mathbf{B}\rangle$ relation is that the average magnetic field is dominated by the strong field close to the point immediately behind the DF where $\mathbf{B}_{\text{in}}$ is measured. Then $\langle\mathbf{B}\rangle$ is always close to $\mathbf{B}_{\text{in}}$, and the $\mathbf{j}$-$\langle\mathbf{B}\rangle$ relation is similar to the $\mathbf{j}$-$\mathbf{B}_{\text{in}}$ relation. To deal with this doubt, I also compare $\mathbf{j}$ with the average magnetic field direction $\langle\mathbf{b}\rangle$ over the DF thickness. I normalize the magnetic field at each time point within the DF layer (from t_{out} to t_{in}) and then average these field directions to get $\langle\mathbf{b}\rangle$. Since I have assumed that the magnetic field at any point inside the DF layer has no normal (to the DF) component, $\langle\mathbf{b}\rangle$ is parallel to the DF. The cross-product of $\langle\mathbf{b}\rangle$ and $\mathbf{L}$ gives the DF normal direction. For good $\langle\mathbf{b}\rangle \times \mathbf{L}$ method-determined normal directions, I still apply the good $\mathbf{L}$ and good angle (on the angle between $\langle\mathbf{b}\rangle$ and $\mathbf{L}$) requirements. Since $\langle\mathbf{b}\rangle$ has no magnitude, I use the good $\langle\mathbf{B}\rangle$ requirement for reliable magnetic field direction. Figures D.4 and D.5 demonstrate the distribution of the angle from $\langle\mathbf{b}\rangle$ to $\mathbf{L}$ ($\theta_{\langle\mathbf{b}\rangle\text{-}\mathbf{L}}$, the sign of this angle is assigned in the same way as $\theta_{\mathbf{B}_{\text{in}}\text{-}\mathbf{L}}$ and $\theta_{\langle\mathbf{B}\rangle\text{-}\mathbf{L}}$), using the $\langle\mathbf{b}\rangle \times \mathbf{L}$ method for the DF normal direction. The trends are the same as those in the plots using $\mathbf{B}_{\text{in}}$ or $\langle\mathbf{B}\rangle$. In addition, $\langle b_x\rangle$ has the same sign as B_{qx} for 94% of all my events (1828 out of 1950), so the DFCS $\langle\mathbf{b}\rangle$-aligned component $j_{\|\text{-}\langle\mathbf{b}\rangle}$ is earthward/tailward on the DF's morning/evening part. In conclusion, the average DFCS current direction over the DF thickness has a region-1-sense relationship to the average magnetic field direction over the DF thickness.

Finally, I note that the slopes of the linear least square fits in Figures D.2b-e and Figures D.4b-e are larger than those in the main article's Figures 5.2c-f. Therefore $\mathbf{j}$ is more aligned

---

Figure D.2 *(preceding page)*: The distribution of $\theta_{\langle\mathbf{B}\rangle\text{-}\mathbf{L}}$, the angle from $\langle\mathbf{B}\rangle$ to $\mathbf{L}$, ordered in the same way as Figure 5.2. The dipolarization front normal directions used in panels b-e are determined using the $\langle\mathbf{B}\rangle \times \mathbf{L}$ method; with these normal directions I determined the events in panels b-e to be earthward-normal DFs, using the method explained in the beginning of section 5.2.2.1.The black dots in panels b-e represent events that do not meet the good angle (angle between $\langle\mathbf{B}\rangle$ and $\mathbf{L}$) requirement in DF normal determination; the red dots represent those that do. All events in panels a-e meet good $\langle\mathbf{B}\rangle$ and good $\mathbf{L}$ requirements.

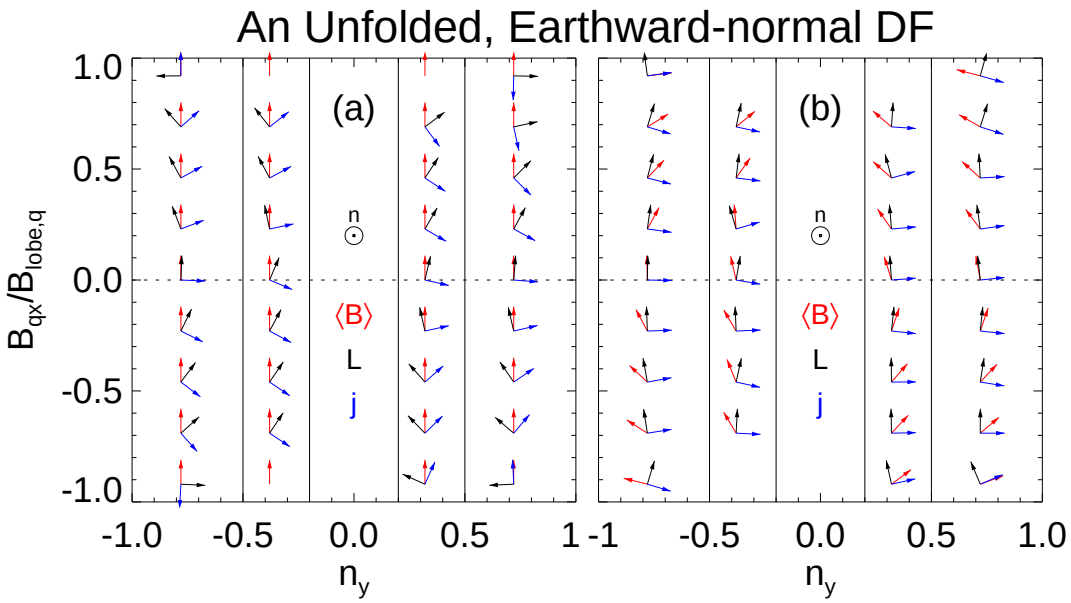

Figure D.3: $\langle \mathbf{B} \rangle$, $\mathbf{L}$, and $\mathbf{j}$ directions inferred from the black vertical bars (median $\theta_{\langle \mathbf{B} \rangle \text{-} \mathbf{L}}$ values) in Figures D.2b-e, ordered in the same way as in Figure 5.3 in the main text.

with $\langle \mathbf{B} \rangle$ and $\langle \mathbf{b} \rangle$ than with $\mathbf{B}_{\text{in}}$.

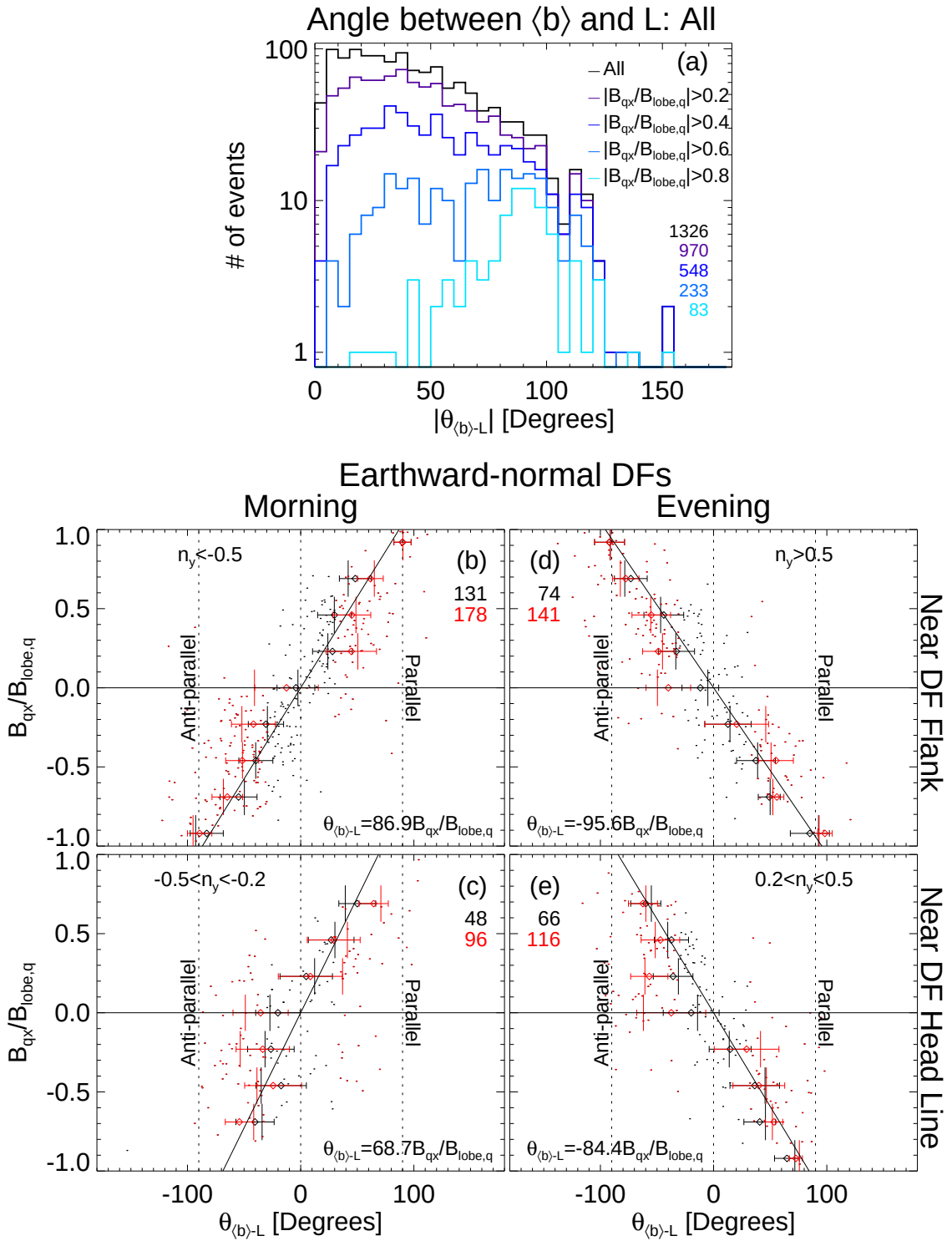
Angle between ⟨b⟩ and L: All
100
10
1
# of events
(a)
All
|Bqx/Blobe,q|>0.2
|Bqx/Blobe,q|>0.4
|Bqx/Blobe,q|>0.6
|Bqx/Blobe,q|>0.8
1326
970
548
233
83
0
50
100
150
|θ⟨b⟩-L| [Degrees]
Earthward-normal DFs
Morning
Evening
Near DF Flank
Near DF Head Line
ny<-0.5
(b)
131
178
ny>0.5
(d)
74
141
-0.5<ny<-0.2
(c)
48
96
0.2<ny<0.5
(e)
66
116
Anti-parallel
Parallel
θ⟨b⟩-L=86.9Bqx/Blobe,q
θ⟨b⟩-L=-95.6Bqx/Blobe,q
θ⟨b⟩-L=68.7Bqx/Blobe,q
θ⟨b⟩-L=-84.4Bqx/Blobe,q
Bqx/Blobe,q
1.0
0.5
0.0
-0.5
-1.0
-100
0
100
θ⟨b⟩-L [Degrees]

Figure D.4 *(preceding page)*: The distribution of $\theta_{\langle \mathbf{b} \rangle\text{-}\mathbf{L}}$, the angle from $\langle \mathbf{b} \rangle$ to $\mathbf{L}$, ordered in the same way as in Figures D.2 and 5.2. The dipolarization front normal directions used in panels b-e are determined using $\langle \mathbf{b} \rangle \times \mathbf{L}$ method. With these normal directions I determined the events in panels b-e to be earthward-normal DFs, using the method explained in the beginning of section 5.2.2.1. The black dots in panels b-e represent the events that do not meet the good angle (angle between $\langle \mathbf{b} \rangle$ and $\mathbf{L}$) requirement in DF normal determination; the red dots represent those do. All events in panels a-e meet good $\langle \mathbf{B} \rangle$ and good $\mathbf{L}$ requirements.

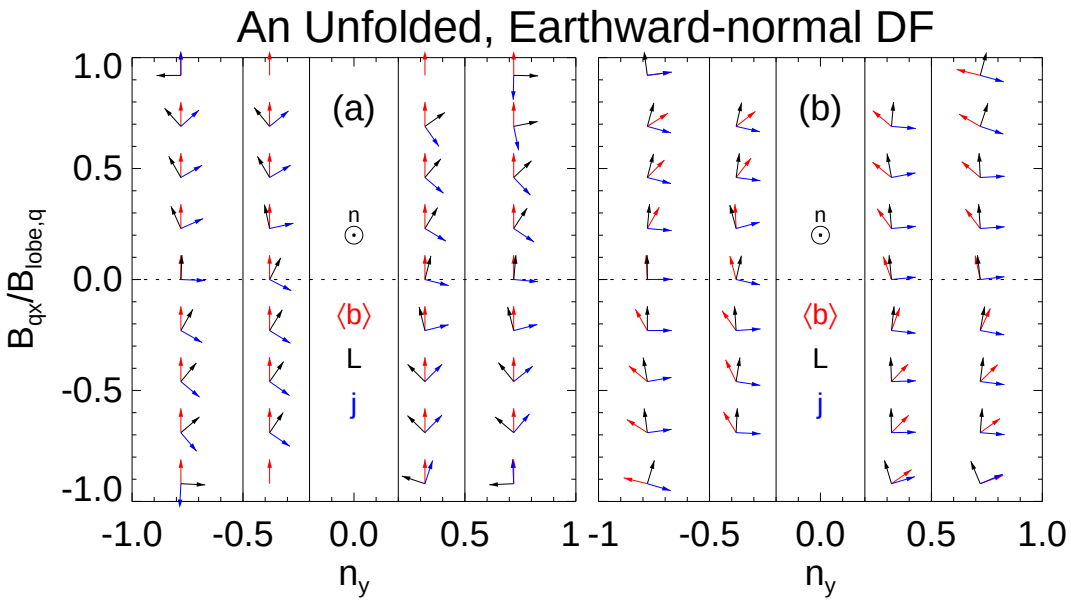

Figure D.5: $\langle \mathbf{b} \rangle$, $\mathbf{L}$ and $\mathbf{j}$ directions inferred from the black vertical bars (median $\theta_{\langle \mathbf{b} \rangle\text{-}\mathbf{L}}$ values) in Figures D.4b-e, ordered in the same way as in Figures D.3 and 5.3.

Bibliography

Akasofu, S.-I. (1964), The development of the auroral substorm, *Planet. Space Sci.*, *12*, 273–282, doi:10.1016/0032-0633(64)90151-5.

Angelopoulos, V. (2008), The THEMIS Mission, *Space Sci. Rev.*, *141*, 5–34, doi:10.1007/s11214-008-9336-1.

Angelopoulos, V., W. Baumjohann, C. F. Kennel, F. V. Coroniti, M. G. Kivelson, R. Pellat, R. J. Walker, H. Luehr, and G. Paschmann (1992), Bursty bulk flows in the inner central plasma sheet, *J. Geophys. Res.*, *97*, 4027–4039, doi:10.1029/91JA02701.

Angelopoulos, V., C. F. Kennel, F. V. Coroniti, W. C. Feldman, J. T. Gosling, M. G. Kivelson, R. J. Walker, and C. T. Russell (1993), Observations of a quasi-static plasma sheet boundary, *Geophys. Res. Lett.*, *20*, 2813–2816, doi:10.1029/93GL01979.

Angelopoulos, V., et al. (1994), Statistical characteristics of bursty bulk flow events, *J. Geophys. Res.*, *99*, 21,257–21,280.

Angelopoulos, V., et al. (1996), Multipoint analysis of a bursty bulk flow event on April 11, 1985, *J. Geophys. Res.*, *101*, 4967–4990, doi:10.1029/95JA02722.

Angelopoulos, V., F. S. Mozer, T. Mukai, K. Tsuruda, S. Kokubun, and T. J. Hughes (1999), On the relationship between bursty flows, current disruption and substorms, *Geophys. Res. Lett.*, *26*, 2841–2844, doi:10.1029/1999GL900601.

Angelopoulos, V., et al. (2008a), First Results from the THEMIS Mission, *Space Sci. Rev.*, *141*, 453–476, doi:10.1007/s11214-008-9378-4.

Angelopoulos, V., et al. (2008b), Tail Reconnection Triggering Substorm Onset, *Science*, *321*, 931, doi:10.1126/science.1160495.

Angelopoulos, V., et al. (2009), Response to Comment on "Tail Reconnection Triggering Substorm Onset", *Science*, *324*(5933), 1391, doi:10.1126/science.1168045.

Angelopoulos, V., A. Runov, X.-Z. Zhou, D. L. Turner, S. A. Kiehas, S.-S. Li, and I. Shinohara (2013), Electromagnetic Energy Conversion at Reconnection Fronts, *Science*, *341*, 1478–1482, doi:10.1126/science.1236992.

Asano, Y., et al. (2005), How typical are atypical current sheets?, *Geophys. Res. Lett.*, *32*, L03108, doi:10.1029/2004GL021834.

Auster, H. U., et al. (2008), The THEMIS Fluxgate Magnetometer, *Space Sci. Rev.*, *141*, 235–264, doi:10.1007/s11214-008-9365-9.

Baumjohann, W., G. Paschmann, and H. Luehr (1990), Characteristics of high-speed ion flows in the plasma sheet, *J. Geophys. Res.*, *95*, 3801–3809, doi:10.1029/JA095iA04p03801.

Birn, J., and M. Hesse (2013), The substorm current wedge in mhd simulations, *J. Geophys. Res.*, *118*, doi:10.1002/jgra.50187.

Birn, J., M. Hesse, G. Haerendel, W. Baumjohann, and K. Shiokawa (1999), Flow braking and the substorm current wedge, *J. Geophys. Res.*, *104*, 19,895–19,904, doi:10.1029/1999JA900173.

Birn, J., J. Raeder, Y. Wang, R. Wolf, and M. Hesse (2004a), On the propagation of bubbles in the geomagnetic tail, *Ann. Geophys.*, *22*, 1773–1786, doi:10.5194/angeo-22-1773-2004.

Birn, J., M. F. Thomsen, and M. Hesse (2004b), Electron acceleration in the dynamic magnetotail: Test particle orbits in three-dimensional magnetohydrodynamic simulation fields, *Phys. Plasmas*, *11*, 1825–1833, doi:10.1063/1.1704641.

Birn, J., M. Hesse, R. Nakamura, and S. Zaharia (2013), Particle acceleration in dipolarization events, *J. Geophys. Res.*, *118*, 1960–1971, doi:10.1002/jgra.50132.

Bonnell, J. W., F. S. Mozer, G. T. Delory, A. J. Hull, R. E. Ergun, C. M. Cully, V. Angelopoulos, and P. R. Harvey (2008), The Electric Field Instrument (EFI) for THEMIS, *Space Sci. Rev.*, *141*, 303–341, doi:10.1007/s11214-008-9469-2.

Chen, C. X., and R. A. Wolf (1993), Interpretation of high-speed flows in the plasma sheet, *J. Geophys. Res.*, *98*, 21,409, doi:10.1029/93JA02080.

Chen, C. X., and R. A. Wolf (1999), Theory of thin-filament motion in Earth's magnetotail and its application to bursty bulk flows, *J. Geophys. Res.*, *104*, 14,613–14,626, doi:10.1029/1999JA900005.

Coroniti, F. V. (1985), Explosive tail reconnection - The growth and expansion phases of magnetospheric substorms, *J. Geophys. Res.*, *90*, 7427–7447, doi:10.1029/JA090iA08p07427.

Dungey, J. W. (1961), Interplanetary Magnetic Field and the Auroral Zones, *Phys. Rev. Lett.*, *6*, 47–48, doi:10.1103/PhysRevLett.6.47.

Erickson, G. M., and R. A. Wolf (1980), Is steady convection possible in the earth's magnetotail, *Geophys. Res. Lett.*, *7*, 897–900, doi:10.1029/GL007i011p00897.

Fairfield, D. H., et al. (1998), Geotail observations of substorm onset in the inner magnetotail, *J. Geophys. Res.*, *103*, 103–118, doi:10.1029/97JA02043.

Fu, H. S., Y. V. Khotyaintsev, M. André, and A. Vaivads (2011), Fermi and betatron acceleration of suprathermal electrons behind dipolarization fronts, *Geophys. Res. Lett.*, *38*, L16104, doi:10.1029/2011GL048528.

Fu, H. S., Y. V. Khotyaintsev, A. Vaivads, M. André, and S. Y. Huang (2012), Electric structure of dipolarization front at sub-proton scale, *Geophys. Res. Lett.*, *39*, L06105, doi:10.1029/2012GL051274.

Fu, H. S., Y. V. Khotyaintsev, A. Vaivads, Retino, M. André, and A. Vaivads (2013), Energetic electron acceleration by unsteady magnetic reconnection, *Nature Phys.*, *9*, 426–430, doi:10.1038/nphys2664.

Gabrielse, C., V. Angelopoulos, A. Runov, and D. L. Turner (2012), The effects of transient, localized electric fields on equatorial electron acceleration and transport toward the inner magnetosphere, *J. Geophys. Res.*, *117*, A10213, doi:10.1029/2012JA017873.

Guzdar, P. N., A. B. Hassam, M. Swisdak, and M. I. Sitnov (2010), A simple MHD model for the formation of multiple dipolarization fronts, *Geophys. Res. Lett.*, *37*, 20,102, doi: 10.1029/2010GL045017.

Harris, E. G. (1962), On a plasma sheath separating regions of oppositely directed magnetic field, *Nuovo Cimento*, *23*, 115–121, doi:10.1007/BF02733547.

Hau, L.-N., R. A. Wolf, G.-H. Voigt, and C. C. Wu (1989), Steady state magnetic field configurations for the earth's magnetotail, *J. Geophys. Res.*, *94*, 1303–1316, doi:10.1029/ JA094iA02p01303.

Hsu, T.-S., R. L. McPherron, V. Angelopoulos, Y. Ge, H. Zhang, C. Russell, X. Chu, and J. Kissinger (2012), A statistical analysis of the association between fast plasma flows and Pi2 pulsations, *J. Geophys. Res.*, *117*, A11221, doi:10.1029/2012JA018173.

Jacquey, C., J. A. Sauvaud, J. Dandouras, and A. Korth (1993), Tailward propagating cross-tail current disruption and dynamics of near-earth tail - A multi-point measurement analysis, *Geophys. Res. Lett.*, *20*, 983–986, doi:10.1029/93GL00072.

Kauristie, K., V. A. Sergeev, M. Kubyshkina, T. I. Pulkkinen, V. Angelopoulos, T. Phan, R. P. Lin, and J. A. Slavin (2000), Ionospheric current signatures of transient plasma sheet flows, *J. Geophys. Res.*, *105*, 10,677–10,690, doi:10.1029/1999JA900487.

Kauristie, K., V. A. Sergeev, O. Amm, M. V. Kubyshkina, J. Jussila, E. Donovan, and K. Liou (2003), Bursty bulk flow intrusion to the inner plasma sheet as inferred from auroral observations, *J. Geophys. Res.*, *108*, 1040, doi:10.1029/2002JA009371.

Keiling, A., et al. (2009), Substorm current wedge driven by plasma flow vortices: THEMIS observations, *J. Geophys. Res.*, *114*, doi:10.1029/2009JA014114.

Kissinger, J., R. L. McPherron, T.-S. Hsu, and V. Angelopoulos (2012), Diversion of plasma due to high pressure in the inner magnetosphere during steady magnetospheric convection, *J. Geophys. Res.*, *117*, A05206, doi:10.1029/2012JA017579.

Lee, D.-Y., H.-S. Kim, S. Ohtani, and M. Y. Park (2012), Statistical characteristics of plasma flows associated with magnetic dipolarizations in the near-tail region of r $<$ 12 R_E, *J. Geophys. Res.*, *117*, A01207, doi:10.1029/2011JA017246.

Li, S.-S., V. Angelopoulos, A. Runov, X.-Z. Zhou, J. McFadden, D. Larson, J. Bonnell, and U. Auster (2011), On the force balance around dipolarization fronts within bursty bulk flows, *J. Geophys. Res.*, *116*, A00I35, doi:10.1029/2010JA015884.

Liu, J., et al. (2009), THEMIS observation of a substorm event on 04:35, 22 February 2008, *Ann. Geophys.*, *27*, 1831–1841, doi:10.5194/angeo-27-1831-2009.

Liu, J., V. Angelopoulos, M. Kubyshkina, J. McFadden, K.-H. Glassmeier, and C. T. Russell (2011a), Revised timing and onset location of two isolated substorms observed by Time History of Events and Macroscale Interactions During Substorms (THEMIS), *J. Geophys. Res.*, *116*, A00I17, doi:10.1029/2010JA015877.

Liu, J., C. Gabrielse, V. Angelopoulos, N. A. Frissell, L. R. Lyons, J. P. McFadden, J. Bonnell, and K. H. Glassmeier (2011b), Superposed epoch analysis of magnetotail flux transport during substorms observed by THEMIS, *J. Geophys. Res.*, *116*, A00I29, doi:10.1029/2010JA015886.

Liu, J., V. Angelopoulos, A. Runov, and X.-Z. Zhou (2013a), On the current sheets surrounding dipolarizing flux bundles in the magnetotail: The case for wedgelets, *J. Geophys. Res.*, *118*, 2000–2020, doi:10.1002/jgra.50092.

Liu, J., V. Angelopoulos, X.-Z. Zhou, A. Runov, and Z. H. Yao (2013b), On the role of pressure and flow perturbations around dipolarizing flux bundles, *J. Geophys. Res.*, under review.

Liu, J., V. Angelopoulos, X.-Z. Zhou, and A. Runov (2013c), Magnetic flux transport by dipolarizing flux bundles, *J. Geophys. Res.*, under review.

Liu, J., et al. (2013d), On the cause of the B_z dip ahead of dipolarizing flux bundles, manuscript in preparation.

McFadden, J. P., C. W. Carlson, D. Larson, M. Ludlam, R. Abiad, B. Elliott, P. Turin, M. Marckwordt, and V. Angelopoulos (2008), The THEMIS ESA Plasma Instrument and In-flight Calibration, *Space Sci. Rev.*, *141*, 277–302, doi:10.1007/s11214-008-9440-2.

McPherron, R. L., C. T. Russell, and M. P. Aubry (1973), Satellite studies of magnetospheric substorms on August 15, 1968. 9. Phenomenological model for substorms., *J. Geophys. Res.*, *78*, 3131–3149, doi:10.1029/JA078i016p03131.

McPherron, R. L., T.-S. Hsu, J. Kissinger, X. Chu, and V. Angelopoulos (2011), Characteristics of plasma flows at the inner edge of the plasma sheet, *J. Geophys. Res.*, *116*, A00I33, doi:10.1029/2010JA015923.

Milan, S. E., G. Provan, and B. Hubert (2007), Magnetic flux transport in the Dungey cycle: A survey of dayside and nightside reconnection rates, *J. Geophys. Res.*, *112*, A01,209, doi:10.1029/2006JA011642.

Moore, T. E., R. L. Arnoldy, J. Feynman, and D. A. Hardy (1981), Propagating substorm injection fronts, *J. Geophys. Res.*, *86*, 6713–6726, doi:10.1029/JA086iA08p06713.

Nagai, T. (1982), Observed magnetic substorm signatures at synchronous altitude, *J. Geophys. Res.*, *87*, 4405–4417, doi:10.1029/JA087iA06p04405.

Nagai, T., et al. (1998), Structure and dynamics of magnetic reconnection for substorm onsets with Geotail observations, *J. Geophys. Res.*, *103*, 4419–4440, doi:10.1029/97JA02190.

Nakamura, R., T. Oguti, T. Yamamoto, and S. Kokubun (1993), Equatorward and poleward expansion of the auroras during auroral substorms, *J. Geophys. Res.*, *98*, 5743–5759, doi:10.1029/92JA02230.

Nakamura, R., W. Baumjohann, R. Schödel, M. Brittnacher, V. A. Sergeev, M. Kubyshkina, T. Mukai, and K. Liou (2001), Earthward flow bursts, auroral streamers, and small expansions, *J. Geophys. Res.*, *106*, 10,791–10,802, doi:10.1029/2000JA000306.

Nakamura, R., et al. (2002), Motion of the dipolarization front during a flow burst event observed by Cluster, *Geophys. Res. Lett.*, *29*(20), 1942, doi:10.1029/2002GL015763.

Nakamura, R., et al. (2004), Spatial scale of high-speed flows in the plasma sheet observed by Cluster, *Geophys. Res. Lett.*, *31*, L09804, doi:10.1029/2004GL019558.

Nakamura, R., et al. (2008), Cluster observations of an ion-scale current sheet in the magnetotail under the presence of a guide field, *J. Geophys. Res.*, *113*, A07S16, doi: 10.1029/2007JA012760.

Nishimura, Y., L. Lyons, S. Zou, V. Angelopoulos, and S. Mende (2010a), Substorm triggering by new plasma intrusion: THEMIS all-sky imager observations, *J. Geophys. Res.*, *115*, doi:10.1029/2009JA015166.

Nishimura, Y., et al. (2010b), Preonset time sequence of auroral substorms: Coordinated observations by all-sky imagers, satellites, and radars, *J. Geophys. Res.*, *115*, A00I08, doi:10.1029/2010JA015832.

Nishimura, Y., L. R. Lyons, T. Kikuchi, V. Angelopoulos, E. Donovan, S. Mende, P. J. Chi, and T. Nagatsuma (2012), Formation of substorm Pi2: A coherent response to auroral streamers and currents, *J. Geophys. Res.*, *117*, A09218, doi:10.1029/2012JA017889.

Ober, D. M., N. C. Maynard, W. J. Burke, W. K. Peterson, J. B. Sigwarth, L. A. Frank, J. D. Scudder, W. J. Hughes, and C. T. Russell (2001), Electrodynamics of the poleward auroral border observed by Polar during a substorm on April 22, 1998, *J. Geophys. Res.*, *106*, 5927–5944, doi:10.1029/2000JA003024.

Ohtani, S., M. A. Shay, and T. Mukai (2004), Temporal structure of the fast convective flow in the plasma sheet: Comparison between observations and two-fluid simulations, *J. Geophys. Res.*, *109*, 3210, doi:10.1029/2003JA010002.

Palin, L., C. Jacquey, J.-A. Sauvaud, B. Lavraud, E. Budnik, V. Angelopoulos, U. Auster, J. P. McFadden, and D. Larson (2012), Statistical analysis of dipolarizations using spacecraft closely separated along Z in the near-Earth magnetotail, *J. Geophys. Res.*, *117*, A09215, doi:10.1029/2012JA017532.

Panov, E. V., et al. (2010), Multiple overshoot and rebound of a bursty bulk flow, *Geophys. Res. Lett.*, *37*, L08103, doi:10.1029/2009GL041971.

Pontius, D. H., Jr., and R. A. Wolf (1990), Transient flux tubes in the terrestrial magnetosphere, *Geophys. Res. Lett.*, *17*, 49–52, doi:10.1029/GL017i001p00049.

Pritchett, P. L., and F. V. Coroniti (2010), A kinetic ballooning/interchange instability in the magnetotail, *J. Geophys. Res.*, *115*, 6301, doi:10.1029/2009JA014752.

Pritchett, P. L., and F. V. Coroniti (2011), Plasma sheet disruption by interchange-generated flow intrusions, *Geophys. Res. Lett.*, *38*, L10102, doi:10.1029/2011GL047527.

Rostoker, G. (1991), Some observational constraints for substorm models, *Magnetospheric Substorms, Geophys. Monogr. Ser., AGU*, *64*, 61–72, doi:10.1029/GM064p0061.

Runov, A., et al. (2003), Current sheet structure near magnetic X-line observed by Cluster, *Geophys. Res. Lett.*, *30*(11), 1579, doi:10.1029/2002GL016730.

Runov, A., V. Angelopoulos, M. I. Sitnov, V. A. Sergeev, J. Bonnell, J. P. McFadden, D. Larson, K. Glassmeier, and U. Auster (2009), THEMIS observations of an earthward-propagating dipolarization front, *Geophys. Res. Lett.*, *36*, 14,106, doi:10.1029/2009GL038980.

Runov, A., V. Angelopoulos, X.-Z. Zhou, X.-J. Zhang, S. Li, F. Plaschke, and J. Bonnell (2011), A THEMIS multicase study of dipolarization fronts in the magnetotail plasma sheet, *J. Geophys. Res.*, *116*, A05216, doi:10.1029/2010JA016316.

Runov, A., et al. (2011), Dipolarization fronts in the magnetotail plasma sheet, *Planet. Space Sci.*, *59*(7), 517 – 525, doi:10.1016/j.pss.2010.06.006.

Runov, A., V. Angelopoulos, C. Gabrielse, X.-Z. Zhou, D. Turner, and F. Plaschke (2013), Electron fluxes and pitch-angle distributions at dipolarization fronts: THEMIS multipoint observations, *J. Geophys. Res.*, *118*, 744–755, doi:10.1002/jgra.50121.

Russell, C. T., and R. L. McPherron (1973), The Magnetotail and Substorms, *Space Sci. Rev.*, *15*, 205–266, doi:10.1007/BF00169321.

Russell, C. T., R. L. McPherron, and P. J. Coleman, Jr. (1971), Magnetic field variations in the near geomagnetic tail associated with weak substorm activity., *J. Geophys. Res.*, *76*, 1823–1829, doi:10.1029/JA076i007p01823.

Saito, M. H., L.-N. Hau, C.-C. Hung, Y.-T. Lai, and Y.-C. Chou (2010), Spatial profile of magnetic field in the near-Earth plasma sheet prior to dipolarization by THEMIS: Feature of minimum B, *Geophys. Res. Lett.*, *37*, L08106, doi:10.1029/2010GL042813.

Schmid, D., M. Volwerk, R. Nakamura, W. Baumjohann, and M. Heyn (2011), A statistical and event study of magnetotail dipolarization fronts, *Ann. Geophys.*, *29*, 1537–1547, doi:10.5194/angeo-29-1537-2011.

Schödel, R., W. Baumjohann, R. Nakamura, V. A. Sergeev, and T. Mukai (2001), Rapid flux transport in the central plasma sheet, *J. Geophys. Res.*, *106*, 301–314, doi:10.1029/2000JA900139.

Semenov, V. S., T. Penz, V. V. Ivanova, V. A. Sergeev, H. K. Biernat, R. Nakamura, M. F. Heyn, I. V. Kubyshkin, and I. B. Ivanov (2005), Reconstruction of the reconnection rate from Cluster measurements: First results, *J. Geophys. Res.*, *110*, 11,217, doi:10.1029/2005JA011181.

Sergeev, V., et al. (2003), Current sheet flapping motion and structure observed by Cluster, *Geophys. Res. Lett.*, *30*(6), 1327, doi:10.1029/2002GL016500.

Sergeev, V., V. Angelopoulos, S. Apatenkov, J. Bonnell, R. Ergun, R. Nakamura, J. McFadden, D. Larson, and A. Runov (2009), Kinetic structure of the sharp injection/dipolarization front in the flow-braking region, *Geophys. Res. Lett.*, *36*, 21,105, doi:10.1029/2009GL040658.

Sergeev, V. A., R. C. Elphic, F. S. Mozer, A. Saint-Marc, and J. A. Sauvaud (1992), A two

satellite study of nightside flux transfer events in the plasma sheet, *Planet. Space Sci.*, *40*, 1551–1572, doi:10.1016/0032-0633(92)90052-P.

Sergeev, V. A., T. I. Pulkkinen, T. I. Pellinen, and N. A. Tsyganenko (1994), Hybird state of the tail mangetic configuration during steady convection events, *J. Geophys. Res.*, *99*, 23,571, doi:10.1029/94JA01980.

Sergeev, V. A., V. Angelopoulos, J. T. Gosling, C. A. Cattell, and C. T. Russell (1996), Detection of localized, plasma-depleted flux tubes or bubbles in the midtail plasma sheet, *J. Geophys. Res.*, *101*, 10,817–10,826, doi:10.1029/96JA00460.

Sergeev, V. A., N. A. Tsyganenko, M. V. Smirnov, A. V. Nikolaev, H. J. Singer, and W. Baumjohann (2011), Magnetic effects of the substorm current wedge in a "spread-out wire model" and their comparison with ground, geosynchronous, and tail lobe data, *J. Geophys. Res.*, *116*, A07218, doi:10.1029/2011JA016471.

Shang, W.-S., et al. (2013), Braking of high speed flows in the magnetotail: Themis joint observations, *Chin. Sci. Bull.*, in press.

Shi, Q. Q., C. Shen, Z. Y. Pu, M. W. Dunlop, Q.-G. Zong, H. Zhang, C. J. Xiao, Z. X. Liu, and A. Balogh (2005), Dimensional analysis of observed structures using multipoint magnetic field measurements: Application to Cluster, *Geophys. Res. Lett.*, *32*, L12105, doi:10.1029/2005GL022454.

Shiokawa, K., W. Baumjohann, and G. Haerendel (1997), Braking of high-speed flows in the near-Earth tail, *Geophys. Res. Lett.*, *24*, 1179–1182, doi:10.1029/97GL01062.

Shukhtina, M. A., E. I. Gordeev, and V. A. Sergeev (2009), Time-varying magnetotail magnetic flux calculation: a test of the method, *Ann. Geophys.*, *27*, 1583–1591, doi: 10.5194/angeo-27-1583-2009.

Sibeck, D. G., and V. Angelopoulos (2008), THEMIS Science Objectives and Mission Phases, *Space Sci. Rev.*, *141*, 35–59, doi:10.1007/s11214-008-9393-5.

Sitnov, M. I., M. Swisdak, and A. V. Divin (2009), Dipolarization fronts as a signature of transient reconnection in the magnetotail, *J. Geophys. Res.*, *114*, A04202, doi:10.1029/2008JA013980.

Sonnerup, B. U. Ö., and M. Scheible (1998), Minimum and Maximum Variance Analysis, *ISSI Scientific Reports Series*, *1*, 185–220.

Sormakov, D. A., and V. A. Sergeev (2008), Topology of Magnetic Flux Ropes in the Magnetospheric Plasma Sheet as Measured by the Geotail Spacecraft, *Cosmic Res.*, *46*, 387–391.

Sun, W. J., et al. (2013), Field-aligned currents associated with dipolarization fronts, *Geophys. Res. Lett.*, doi:10.1002/grl.50902.

Tu, J.-N., K. Tsuruda, H. Hayakawa, A. Matsuoka, T. Mukai, I. Nagano, and S. Yagitani (2000), Statistical nature of impulsive electric fields associated with fast ion flow in the near-Earth plasma sheet, *J. Geophys. Res.*, *105*, 18,901, doi:10.1029/1999JA000428.

Vasyliunas, V. M. (1970), Mathematical Models of Magnetospheric Convection and Its Coupling to the Ionosphere, in *Particles and Field in the Magnetosphere*, *Astrophysics and Space Science Library*, vol. 17, edited by B. M. McCormack and A. Renzini, p. 60.

Wolf, R. A., C. X. Chen, and F. R. Toffoletto (2012), Thin filament simulations for Earth's plasma sheet: Interchange oscillations, *J. Geophys. Res.*, *117*, A02215, doi:10.1029/2011JA016971.

Xing, X., L. R. Lyons, V. Angelopoulos, D. Larson, J. McFadden, C. Carlson, A. Runov, and U. Auster (2009), Azimuthal plasma pressure gradient in quiet time plasma sheet, *Geophys. Res. Lett.*, *36*, L14105, doi:10.1029/2009GL038881.

Xing, X., et al. (2011), Near-Earth plasma sheet azimuthal pressure gradient and associated auroral development soon before substorm onset, *J. Geophys. Res.*, *116*, A07204, doi:10.1029/2011JA016539.

Xing, X., L. R. Lyons, X.-Z. Zhou, V. Angelopoulos, E. Donovan, D. Larson, C. Carlson, and U. Auster (2012), On the formation of pre-onset azimuthal pressure gradient in the near-Earth plasma sheet, *J. Geophys. Res.*, *117*, A08224, doi:10.1029/2012JA017840.

Yang, J., F. R. Toffoletto, R. A. Wolf, and S. Sazykin (2011), RCM-E simulation of ion acceleration during an idealized plasma sheet bubble injection, *J. Geophys. Res.*, *116*, A05207, doi:10.1029/2010JA016346.

Yang, J., F. R. Toffoletto, R. A. Wolf, S. Sazykin, P. A. Ontiveros, and J. M. Weygand (2012), Large-scale current systems and ground magnetic disturbance during deep substorm injections, *J. Geophys. Res.*, *117*, A04223, doi:10.1029/2011JA017415.

Yao, Z. H., et al. (2012), Mechanism of substorm current wedge formation: THEMIS observations, *Geophys. Res. Lett.*, *39*, L13102, doi:10.1029/2012GL052055.

Yao, Z. H., et al. (2013), Conjugate observations of flow diversion in the magnetotail and auroral arc extension in the ionosphere, *J. Geophys. Res.*, doi:10.1002/jgra.50419.

Zesta, E., L. R. Lyons, and E. Donovan (2000), The auroral signature of Earthward flow bursts observed in the magnetotail, *Geophys. Res. Lett.*, *27*, 3241–3244, doi:10.1029/2000GL000027.

Zesta, E., E. Donovan, L. Lyons, G. Enno, J. S. Murphree, and L. Cogger (2002), Two-dimensional structure of auroral poleward boundary intensifications, *J. Geophys. Res.*, *107*, 1350, doi:10.1029/2001JA000260.

Zhang, H., et al. (2007), TC-1 observations of flux pileup and dipolarization-associated expansion in the near-Earth magnetotail during substorms, *Geophys. Res. Lett.*, *34*, 3104, doi:10.1029/2006GL028326.

Zhang, X., V. Angelopoulos, A. Runov, X. Zhou, J. Bonnell, J. P. McFadden, D. Larson, and U. Auster (2011), Current carriers near dipolarization fronts in the magnetotail: A THEMIS event study, *J. Geophys. Res.*, *116*, doi:10.1029/2010JA015885.

Zhou, X., V. Angelopoulos, V. A. Sergeev, and A. Runov (2010), Accelerated ions ahead of earthward propagating dipolarization fronts, *J. Geophys. Res.*, *115*, doi:10.1029/2010JA015481.

Zhou, X.-Z., V. Angelopoulos, A. Runov, and J. Liu (), On the origin of pressure and magnetic perturbations ahead of dipolarization fronts, *J. Geophys. Res.*, submitted.

Zhou, X.-Z., V. Angelopoulos, V. A. Sergeev, and A. Runov (2011), On the nature of precursor flows upstream of advancing dipolarization fronts, *J. Geophys. Res.*, *116*, A03222, doi:10.1029/2010JA016165.

Zhou, X.-Z., V. Angelopoulos, A. Runov, J. Liu, and Y. S. Ge (2012), Emergence of the active magnetotail plasma sheet boundary from transient, localized ion acceleration, *J. Geophys. Res.*, *117*, A10216, doi:10.1029/2012JA018171.

Zong, Q.-G., et al. (2004), Cluster observations of earthward flowing plasmoid in the tail, *Geophys. Res. Lett.*, *31*, L18803, doi:10.1029/2004GL020692.